Project Title:

QUalifying and Implementing a user-centric designed and EfficienT electric vehicle

Project Acronym: QUIET

GA: **769826**

Topic: **Electric vehicle user-centric design for optimised energy efficiency**

Topic identifier: **GV-05-2017**

Type of action: **RIA Research and Innovation Action**

Deliverable No.	QUIET D2.2	
Deliverable Title	Multi-physical entire vehicle model; control units for energy management system	
Scheduled Deliverable Date	2019-06	
Actual (granted) Deliverable Date	2020-01	
Deliverable Type	Report	
Dissemination Level	Public	
Written by	Ivan CVOK (UOZ) Igor RATKOVIĆ (UOZ) Joško DEUR (UOZ) Hansjörg KAPELLER (AIT) Dominik DVORAK (AIT) Rebin JABER (AIT) Dragan SIMIC (AIT)	2020-01-24 2020-01-30 2020-01-24 2020-04-09 2019-09-26 2019-09-26 2019-09-26
Checked by	Elena PAFFUMI Tamás TURCSÁN	2020-01-30 2020-01-27
Approved by	WP Leader (HRE-G) Coordinator (AIT) Quality Coordinator (HRE-G)	2020-04-17 2020-04-21 2020-04-17
Status	Version 2.0 (revised version after reopening D2.2 by PO)	2020-04-17

This project has received funding from the European Union's Horizon 2020 research and innovation programme under grant agreement No. 769826. The content of this publication is the sole responsibility of the Consortium partners listed herein and does not necessarily represent the view of the European Commission or its services.

Publishable Executive Summary

The QUIET deliverable D2.2 (Multi-physical entire vehicle model; control units for energy management system) deals with the implementation of the multi-physical entire vehicle model for the energy flow assessment in real-world driving conditions and the hardware implementation of the control units for the energy management system including the intuitive – user centric designed – human-machine user interface. Moreover, the development of an optimal vehicle energy management strategy for user comfort as well as the on-board energy management system are subjects of this deliverable.

To this purpose, D2.2 deals with the completed entire 1D multi-physical vehicle simulation model set up in Dymola/Modelica and based on the data received from Task 1.1. The baseline reference vehicle Honda Fit EV is modelled (with all relevant auxiliary components) and parametrized. The investigated technologies, such as the heating-, ventilation and air conditioning system including the infrared radiation heating system and the thermal energy storage based on PCM, are physically described more in detail. The detailed analysis of radiation, air and refrigerant flow phenomena, is based on the 3D computational fluid dynamics tool Fluent, whereby a co-simulation of the 1D and 3D domain models enables to benefit from the strengths of each tool. Technologies that indirectly affect the energy consumption, such as lightweight material doors and seat structures, have an impact on the vehicle weight and are considered accordingly. With these models a detailed identification of the energy flows of the reference and the improved QUIET vehicle is carried out and the energy-saving potential is determined and refined.

To assess the potential optimal setting of the system parameters, D2.2 deals with the design and optimisation of the energy management strategy based on a reduced-order control-oriented model implemented in Matlab-Simulink. This includes (i) modelling and model-order reduction activity, (ii) development of tools for generating static model maps, linearized model, and model parameter identification, (iii) design of an optimised hierarchical energy management/control strategy and its verification against a benchmark obtained through dynamic programming-based control variable optimization, and (iv) development of a tool for optimising HVAC control input allocation maps and HVAC feedback controller parameters.

The development of the electronic control unit which is required to integrate the vehicle energy management strategy, and which is acting as an interface between the user and modules for heating and cooling is hence described. As user centric design is a key aspect, special focus is laid on the development of a human machine interface. An intuitive display-based (e.g. touch-based) user interface is provided to the user by forwarding its input stimuli (e.g. desired comfort temperature) to the electronic control unit as new conditions for the embedded (optimised) energy management strategy.

This project has received funding from the European Union's Horizon 2020 research and innovation programme under grant agreement No. 769826. The content of this publication is the sole responsibility of the Consortium partners listed herein and does not necessarily represent the view of the European Commission or its services.

Table of Contents

Abbreviations and Nomenclature 10
1. Introduction 12
1.1. Description of the deliverable – Goals 12
2. Multi-physical vehicle modelling for energy flow assessment in real-world driving conditions 14
2.1. Modelica vehicle model 14
2.2. Vehicle cabin model – thermal loads 15
2.2.1. Vehicle cabin model – zones 16
2.3. Heating, Ventilation and Air Conditioning (HVAC) model – thermal vehicle model 17
2.3.1. Thermal vehicle surfaces 17
2.3.2. Thermal vehicle model – convection model 18
2.3.3. Thermal vehicle model – initial approach 19
2.3.4. Thermal vehicle model – advanced approach 20
2.3.5. Results – HVAC modelling 21
2.3.6. Results – temperatures 25
2.3.7. Results – thermal losses 26
2.3.8. Results – lost thermal energy 26
3. Optimal vehicle energy management strategy for user comfort 28
3.1. Control-oriented modelling and analysis tools 28
3.1.1. 12^{th}-order vapour-compression cycle (VCC) model 28
3.1.2. Actuator models 29
3.1.3. Heat exchanger models 29
3.1.4. Overall VCC model 31
3.2. Model reduction method 32
3.2.1. Uniform heat exchanger wall temperature (R9) 32
3.2.2. Static condenser superheating node length Lc1 (R8) 32
3.2.3. Static heat exchanger outlet specific enthalpy (R6) 33
3.2.4. Static condenser two-phase node length (R5) 33
3.2.5. Further reduction steps 34
3.3. Model static mapping, linearization and identification 34
3.3.1. Static input-output maps 34
3.3.2. Linearization 35
3.3.3. Model identification 36
3.4. Control trajectory optimisation and optimised control strategy 38
3.4.1. HVAC and cabin modelling 38
3.4.2. Thermal comfort criterion 40
3.4.3. Control variable optimisation 41
3.4.4. Low-level control system 42

This project has received funding from the European Union's Horizon 2020 research and innovation programme under grant agreement No. 769826. The content of this publication is the sole responsibility of the Consortium partners listed herein and does not necessarily represent the view of the European Commission or its services.

3.4.5. High-level control system 44
3.4.6. Results for cool-down scenario 45
3.4.6.1. Control variable optimisation results 45
3.4.6.2. Control strategy results 46
3.5. Control strategy development for target EV HVAC system using multi-physical Dymola model .. 50
3.6. Optimal allocation of low-level control inputs 51
3.6.1. Optimal allocation problem 51
3.6.2. Optimisation method 53
3.6.3. Implementation of the optimisation method 54
3.6.4. Optimisation results for air-conditioning (A/C) operating mode for maximum system efficiency 55
3.6.5. Influence of different ambient conditions on air-conditioning mode optimisation results 58
3.6.6. Optimisation results for heat pump (HP) operating mode 59
3.7. Multi-objective optimisation 62
3.7.1. Multi-objective optimisation results for A/C operating mode 62
3.7.2. Multi-objective optimisation results for HP operating mode 64
3.8. Tuning of high- and low-level feedback controllers 66
3.8.1. Optimisation of low-level feedback controller parameters 66
3.8.2. Low-level controller gain scheduling maps for A/C mode 66
3.8.3. Low-level controller gain-scheduling maps for HP mode 69
3.8.4. Tuning of superimposed cabin air temperature controller 71
3.9. Dymola implementation of control strategy and verification of optimisation results 72
3.9.1. Overview of HVAC controller implementation in Dymola 72
3.9.2. Cool-down scenario simulation results 73
3.9.3. Heat-up scenario simulation results 75
3.10. Update of Dymola model and control strategy with infrared heating panels functionality 78
4. On-board energy management system and user interface 82
4.1. Hardware platform 82
4.2. GUI-design 84
5. Conclusions 88
6. Biblography 89
7. Acknowledgment 91
Appendix A1 - 12th order model 92
Appendix A2 - 6th order model 93

List of Figures

Figure 1: Detailed Modelica vehicle model of the Honda Fit EV 14

Figure 2: Thermal loads on a vehicle, including radiation, convection and conduction [8]............................15

Figure 3: Zonal model (left), interconnection of two zones with a flow model (middle), illustrative Dymola model with e.g. 4 zones, 2 flow models, 1 source, 1 sink and 1 pressure boundary condition model (right). .16

Figure 4: Zonal Model for the simulation of temperature- and flow distribution in the vehicle cabin (left) and its spatial layout in x-, y- and z-direction. 16

Figure 5: Thermal vehicle outer surfaces of the Honda Fit EV 17

Figure 6: Convection model implemented in Modelica/Dymola applicable for outer and inner surfaces, e.g.: vertical plate (left), horizontal plate (heat top side / cool bottom side) (middle), horizontal plate (heat bottom side / cool top side) (right)..18

Figure 7: Thermal vehicle model for heating mode (initial approach) using only components from the MSL 19

Figure 8: Advanced thermal vehicle model (air path considers also air flow effects) 20

Figure 9: Entire HVAC model 22

Figure 10: Condenser heat transfer optimisation – constant heat transfer coefficient.....................................23

Figure 11: Condenser heat transfer optimisation – comparison of target values and simulation 23

Figure 12: Total cycle validation AC mode (blue) and heat pump mode (red). The grey line is the saturation line of propane; the dashed lines represent the measurements and the solid lines represent the respective simulation results..25

Figure 13: Comparison between measured (blue curve) and simulated (red curve) cabin temperature and temperature profile of coolant water (green curve) 25

Figure 14: Thermal losses: relevant surfaces (left) and their quantification in Watt (right) 26

Figure 15: Lost thermal energy using standard glazing at different surfaces (left) and total (right)...............27

Figure 16: Lost thermal energy using polycarbonate glazing at different surfaces (left) and cabin temperature comparison between standard- and polycarbonate glazing (right) 27

Figure 17: Typical vehicle air-conditioning configuration..28

Figure 18: Heat exchanger node specific state variables and parameters...30

Figure 19: Schematic of the 12th order model of vapour compression cycle with corresponding state variables and control inputs. See Table 2 for the nomenclature definition...31

Figure 20. Response of nonlinear R12 and R6 (with memory blocks) models to a step change in compressor and EXV input..33

Figure 21: Filtered evaporator outlet air temperature map for fixed superheat temperatures (ΔT_{SHd} = 15 °C for $\dot{m}_{ea}$ = 0.02 kg/s and ΔT_{SHd} = 5 °C for $\dot{m}_{ea}$ = 0.075 kg/s and above) (a) and evaporator outlet air temperature and superheat temperature map for fixed air mass flow rates where the red line relates to the corresponding column in Fig. a (b). 35

This project has received funding from the European Union's Horizon 2020 research and innovation programme under grant agreement No. 769826. The content of this publication is the sole responsibility of the Consortium partners listed herein and does not necessarily represent the view of the European Commission or its services.

Figure 22: Response of nonlinear and linearized R12 model to a step change in compressor speed and EXV opening 36

Figure 23: Model identification input data (black lines) and time responses of ARX1 model with third-order polynomials (red line) and ARX2 model with sixth-order polynomials (blue line) for identification data set (a-d) and validation data set (e-h) 38

Figure 24: HVAC and cabin model schematic 38

Figure 25: HVAC model static maps related to evaporator outlet air temperature (a) and efficiency defined by COP (b)....40

Figure 26: Predicted mean vote (*PMV*) map with three inputs where filled circles show comfort range ($|PMV| < 0.5$) (a) and *PMV* map with two inputs and fixed relative humidity ($RH = 44\%$) where black lines denoting comfort range (b) 41

Figure 27: Block diagram of linearized HVAC system and controllers (solid lines) used in controller parameter optimisation (where d denotes disturbance, e.g. varying air mass flow rate) (a), and block diagram of final low-level control system (b); Note: PI controller transfer function is $G_c(s) = K_p(1 + 1/(T_is))$....43

Figure 28: Comparison of low-level controller performance with and without using gain scheduling maps. .44

Figure 29: Cabin air temperature control block diagram....45

Figure 30: Control variable optimisation results for three optimisation cases: PMV minimisation only (blue), COP maximisation only (red) and combined PMV minimisation and COP maximisation (green)....46

Figure 31: Control strategy simulation results for the case of PMV minimisation (blue line), COP maximisation (red line) and combined cost function case (green line); the superimposed cabin temperature controller has the fixed parameters 48

Figure 32: Control strategy simulation results for the case of three different PI controller tunings: Ki = 0.005 (red line), Ki = 0.01 (green line) and Ki = 0.02 (blue line), while the PMV vs. COP trade-off is fixed (to combined penalization) 48

Figure 33: Block diagram of HVAC control system related to Dymola model HVAC dynamics....51

Figure 34: Control parameter optimisation operating point grid for air-conditioning mode (a) and heat pump mode (b) 52

Figure 35: Multi-objective optimisation framework in modeFrontier (a), Flowchart depicting the optimisation loop and input/output processing within each environment (b) 54

Figure 36: Time response of single Dymola model simulation executed within control input optimisation loop 55

Figure 37: Control input allocation optimisation results for air-conditioning operating mode and COP maximisation case showing. Note that in subplots (a)-(f) solid lines correspond to optimal solutions and dashed lines to approximated solutions 57

Figure 38: Comparison of air-conditioning mode optimisation results between nominal case (solid line w/ circles), decreased ambient temperature case (dashed line w/ diamonds) and increased vehicle velocity case (stars)....58

Figure 39: Blower fan air mass flow polynomial coefficients with respect to heating capacity demand 60

This project has received funding from the European Union's Horizon 2020 research and innovation programme under grant agreement No. 769826. The content of this publication is the sole responsibility of the Consortium partners listed herein and does not necessarily represent the view of the European Commission or its services.

Figure 40: Control input allocation optimisation results for heat pump operating mode and COP maximisation case showing: Pump 2 speed n_{p2} (a), Pump 3 speed n_{p3} (b), cabin inlet air inlet temperature $T_{cab,in,R}$ (c), blower fan air mass flow $\dot{m}_{bf}$ (d) optimal COP (e), compressor speed ω_{com} (f), and absolute COP difference (g) and relative COP difference (h) when using approximation curves (bold or dashed lines) instead of real optimisation results (solid lines) 61

Figure 41: Multi-objective optimisation results for A/C mode, showing potential for achieving trade-off between COP maximisation and |PMV| minimisation for different cooling capacity demands and cabin air temperatures: $T_{cab} =$ 20°C (a), $T_{cab} =$ 25°C (b), $T_{cab} =$ 30°C (c) and $T_{cab} =$ 35°C (d) 63

Figure 42: Detailed multi-objective optimisation results for cabin air temperature of 25°C and different cooling capacity demands: trade-off between PMV and COP (a), pump speeds (b), blower fan air mass flow vs cabin inlet air temperature reference (c) and compressor speed (d) 63

Figure 43: Multi-objective optimisation results for HP mode, showing potential for achieving trade-off between COP maximisation and |PMV| minimisation for different cooling capacity demands and cabin air temperatures: 64

Figure 44: Detailed multi-objective optimisation results for cabin air temperature of 25°C and different heating capacity demands: trade-off between PMV and COP (a), pump speeds (b), blower fan air mass flow vs cabin inlet air temperature reference (c) and compressor speed (d) 65

Figure 45: Block diagram of low-level control system comprising independent modified PI controllers and linearized HVAC system model 66

Figure 46: Contour plot showing optimised low-level feedback controller parameters for A/C operating mode (red crosses indicate operating points chosen for final mapping for implementation) 67

Figure 47: Comparison between optimized low-level controller gain-scheduling map (solid lines) and implemented/interpolated gain-scheduling map (dashed lines) for air-conditioning operating mode 68

Figure 48: Closed-loop performance of linear MIMO system in open-loop (red line), using optimised gains (green line) and implemented gains (blue line) for air-conditioning operating mode 68

Figure 49: Contour plot showing feedback controller parameters for heat pump operating mode for all operating points (red crosses indicate operating points chosen for interpolation) 70

Figure 50: Comparison between optimized gain-scheduling map (solid lines) and interpolated gain-scheduling map (dashed lines) for heat pump operating mode 70

Figure 51: Closed-loop performance of linear MIMO system in open-loop (red line), using optimised gains (green line) and implemented gains (blue line) for heat pump operating mode 71

Figure 52: Modified PI controller with saturation logic and gain-scheduling maps, implemented in Dymola72

Figure 53: HVAC control strategy implemented in Dymola 73

Figure 54: Simulation response of overall A/C control system implemented in Dymola, given for cool-down scenario 75

Figure 55: Simulation response of overall HP control system implemented in Dymola, given for heat-up scenario 77

This project has received funding from the European Union's Horizon 2020 research and innovation programme under grant agreement No. 769826. The content of this publication is the sole responsibility of the Consortium partners listed herein and does not necessarily represent the view of the European Commission or its services.

Figure 56: Dymola model extension related to infrared heating functionality: look-up table-based cabin air mass flow and temperature distribution (a), single PMV calculation submodel (b), IR heating panel model (c) ...79

Figure 57: Simulation response comparison of overall HP control system implemented in Dymola without (solid line) and with (dashed line) infrared heating panels, given for heat-up scenario ...81

Figure 58: System overview – Human Machine Interface (HMI) concept ...82

Figure 59: Comparison 7“ and 10“ Display (left), Apalis iMX6Q Module (middle), Apalis Module and Development Board (right) ...83

Figure 60: Interface Board developed by AIT ...83

Figure 61: 1st Draft of possible GUI Design ...84

Figure 62: Advanced draft of possible GUI Design ...84

Figure 63: Implemented GUI Design – AUTO control: driver upper body too hot ...85

Figure 64: Implemented GUI Design – AUTO control: driver upper body too cold ...86

Figure 65: Implemented GUI Design – AUTO control: comfort level of all passengers reached ...86

Figure 66: Implemented GUI Design – custom control ...87

This project has received funding from the European Union’s Horizon 2020 research and innovation programme under grant agreement No. 769826. The content of this publication is the sole responsibility of the Consortium partners listed herein and does not necessarily represent the view of the European Commission or its services.

List of Tables

Table 1: List of Abbreviations 10

Table 2: Nomenclature 11

Table 3: Measured vs. simulated (baseline) driving ranges 15

Table 4: Overview of model order reduction steps and assumptions 32

Table 5: Cumulative energy efficiency and thermal comfort indices for cool-down scenario and different control strategy settings. 49

This project has received funding from the European Union's Horizon 2020 research and innovation programme under grant agreement No. 769826. The content of this publication is the sole responsibility of the Consortium partners listed herein and does not necessarily represent the view of the European Commission or its services.

Abbreviations and Nomenclature

Table 1: List of Abbreviations

Symbol or Shortname	Description
A/C	Air Conditioning
CAN	Controller Area Network
CFD	Computational Fluid Dynamics
DL	Dissemination Level
EC	European Commission
ECU	Electronic Control Unit
EPA	(United States) Environmental Protection Agency
EV	Electric Vehicle
FCX	Fuel Cell eXperimental
GA	General Assembly
HP	Heat Pump
HVAC	Heating, Ventilation and Air Conditioning
MSL	Modelica Standard Library
PO	Project Officer
PC	Project Coordinator
SC	Steering Committee
T	Task
WLTC	Worldwide harmonized Light vehicles Test Cycle
WLTP	Worldwide harmonized Light vehicles Test Procedure
WP	Work Package

This project has received funding from the European Union's Horizon 2020 research and innovation programme under grant agreement No. 769826. The content of this publication is the sole responsibility of the Consortium partners listed herein and does not necessarily represent the view of the European Commission or its services.

Table 2: Nomenclature

A	$[m^2]$	cross-section area	h	$\left[\frac{J}{kg}\right]$	specific enthalpy	$\dot{Q}$	$[W]$	heat flow
A	$[-]$	system matrix	L	$[m]$	length	T	$[K]$	temperature
a_v	$[-]$	valve control input	m	$[kg]$	mass	**u**	$[-]$	input vector
c_p	$\left[\frac{J}{kgK}\right]$	specific heat capacity const. press.	$\dot{m}$	$\left[\frac{kg}{s}\right]$	mass flow rate	V	$[m^3]$	volume
C_v	$[-]$	orifice hydraulic coefficient	n	$[-]$	polytropic coefficient or pump speed	x	$[m]$	position
C	$[-]$	clearance factor	P	$[W]$	power	**x**	$[-]$	state vector
D	$[m]$	diameter	p	$[Pa]$	pressure			
f	$[-]$	conservation matrix	$\dot{q}$	$\left[\frac{W}{kg}\right]$	specific heat flow			

Greek symbols

α	$\left[\frac{W}{m^2K}\right]$	heat transfer coefficient	η	$[-]$	efficiency
γ	$[-]$	void fraction	ρ	$\left[\frac{kg}{m^3}\right]$	fluid density
ε	$[-]$	heat exchanger effectiveness factor	ω	$[rad/s]$	compressor speed

Subscripts

a	air or ambient	l	liquid phase
c	condenser or clearance (compressor)	o	outlet or outer
com	compressor	r	refrigerant
e	evaporator	$\bar{x}$	averaged value of x
g	vapour (gas) phase	SH	superheat temperature
i	inlet or inner	sw	swept
is	isentropic	v	valve / orifice
k	denotes condenser or evaporator	w	tube wall

This project has received funding from the European Union's Horizon 2020 research and innovation programme under grant agreement No. 769826. The content of this publication is the sole responsibility of the Consortium partners listed herein and does not necessarily represent the view of the European Commission or its services.

1. Introduction

D2.2 deals with the implementation of a multi-physical computer simulation model of both (reference and novel) vehicles for the energy flow assessment in real-world driving conditions. The reference vehicle model is used to validate the State of the Art (SotA) energy flows of all reference vehicle components whereupon the novel vehicle model is created to analyse and investigate innovative technologies for their possible introduction and implementation during the QUIET project. The outcomes include the analysis of the thermal needs for passengers, gaining knowledge of the vehicle and the demands of the users including gender and ageing society aspects which aggregate as input for the optimal vehicle energy management strategy for user comfort.
Therefore, the development of an optimal vehicle energy management strategy (with special focus laid on user comfort) is an important target of D2.2, too, along with the development of an intuitive (user centric designed) HMI and the hardware implementation of the control units, needed for the optimised energy management system.

The outcomes of D2.2 are used as inputs within WP2 in T2.5 (First-level assessment of user-oriented on-board energy management).

1.1. Description of the deliverable – Goals

The goals covered in chapter 2 of this report are to provide the entire 1D multi-physical vehicle simulation model set up for the reference and the improved QUIET vehicle to determine energy flows and energy-saving potentials.
The steps are:

- Completion and parameterization of the baseline reference- and the improved vehicle Honda Fit EV models. All auxiliary components to be considered are modelled.
- The technologies to be investigated, such as the heating-, ventilation and air conditioning system including the infrared radiation heating system and the thermal energy storage based on PCM, are physically described.
- Analysing of radiation-, air- and refrigerant flow phenomena by means of a co-simulation of 1D and 3D (computational fluid dynamics, CFD) domain models.

Further goals covered in chapter 3 of D2.2 relate to development of an optimal vehicle energy management strategy for user comfort, which includes the following three distinct activities/steps:

- Building a 12-th order lumped-parameter control-oriented HVAC model implemented within the Matlab/Simulink environment, conducting analytical model-order reduction, and developing tools for generating model static maps, linearization and parameter identification.
- Developing an optimised hierarchical control strategy consisting of supervisory cabin temperature feedback controller, optimal low-level control input allocation algorithm, and low-level feedback controllers of HVAC system, and its verification against a benchmark obtained by using dynamic programming-based control trajectory optimisation tool for a favourable cabin thermal comfort and energy efficient HVAC operation.
- Developing a tool for optimisation of the control input allocation maps and HVAC controller feedback parameters, based on using a multi-objective genetic algorithm and nonlinear Dymola model, and its implementation and verification for full nonlinear Dymola model of target HVAC system.

Finally, chapter 4 of D2.2 deals with hardware implementation of control units for the energy management system including an intuitive, user-friendly HMI. This includes:

This project has received funding from the European Union's Horizon 2020 research and innovation programme under grant agreement No. 769826. The content of this publication is the sole responsibility of the Consortium partners listed herein and does not necessarily represent the view of the European Commission or its services.

- Implementation and execution of the derived optimal vehicle energy management strategy for user comfort on the electronic control unit (ECU, microcontroller), which also provides interfaces to monitor and control the electric vehicle (EV) modules and to anticipate the user's intentions.
- Establishing the ECU-EV interface/communication through the vehicle's on-board CAN-bus.
- Development of a human-machine interface (HMI).
  An intuitive display-based (e.g., touch-based) user interface is provided to the user. The application is intended for providing an input stimulus (e.g. desired temperature) defined by the user.

This project has received funding from the European Union's Horizon 2020 research and innovation programme under grant agreement No. 769826. The content of this publication is the sole responsibility of the Consortium partners listed herein and does not necessarily represent the view of the European Commission or its services.

2. Multi-physical vehicle modelling for energy flow assessment in real-world driving conditions

2.1. Modelica vehicle model

Based on the data received from T1.1 (Vehicle specifications and requirements) an entire 1D multi-physical vehicle simulation model is set up and parameterized (extracted from measurement data) in Dymola/Modelica. To consider also aspects of the thermal management and to assess the energy flow, the development and implementation of a simplified spatial simulation model of the Honda Fit EV vehicle cabin model including thermal models was initiated in T1.4 (Determination of improvement potentials of the reference EV) and completed in T2.2 (Multi-physical vehicle modelling for energy flow assessment in real-world driving conditions).
The obtained cabin model in combination with the multi-physical vehicle model (cp. Figure 1) enabled a realistic estimation of the total energy flow during real-world driving conditions (T2.2).

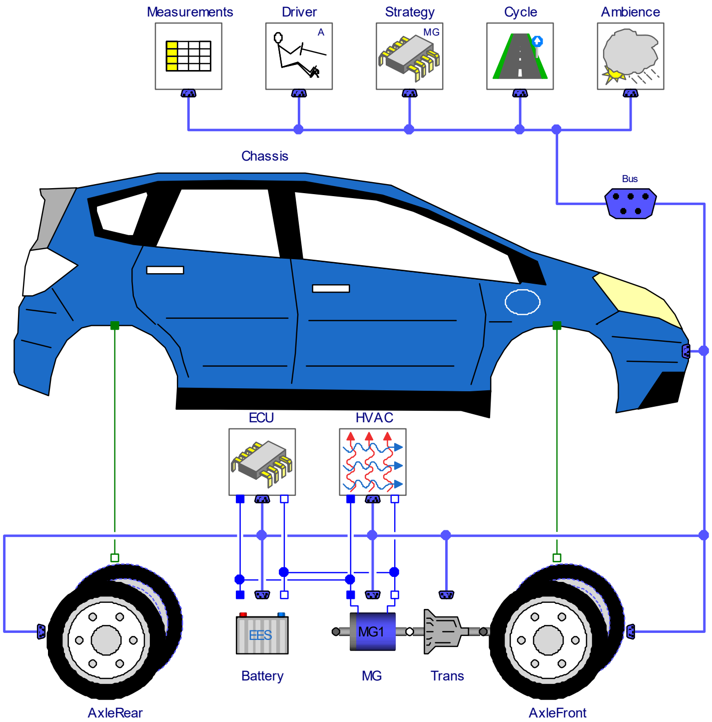

Figure 1: Detailed Modelica vehicle model of the Honda Fit EV

With the vehicle model depicted in Figure 1 a detailed identification of the energy flows of the reference and the improved QUIET vehicle is carried out and possibly energy-saving potentials have been determined and validated with measurement data gained from worldwide harmonized light vehicles test procedures (WLTP) during different ambient conditions (norm @ +23 °C, cold @ -10 °C, hot @ +40 °C).
Table 3 summarizes the performed validation for all different driving modes based on the applied WLTP cycle and for the additional modes MAX heat-up and MAX cool-down (both carried out at 40 km/h constant vehicle speed). The simulated values show only minor differences compared to the measured ones which could be achieved by recursive improvements of the vehicle simulation model during its development and due to suitable selection of different iteration algorithms provided in Dymola.

This project has received funding from the European Union's Horizon 2020 research and innovation programme under grant agreement No. 769826. The content of this publication is the sole responsibility of the Consortium partners listed herein and does not necessarily represent the view of the European Commission or its services.

Table 3: Measured vs. simulated (baseline) driving ranges

Driving mode	Driving range (measured)	Driving range (simulated)	SOC remaining (measured)	SOC remaining (simulated)
WLTP norm (+23 °C)	155.56 km	155.56 km	0.00 %	1.86 %
WLTP cold (-10 °C)	68.40 km	68.43 km	0.00 %	4.86 %
WLTP hot (+40 °C)	137.00 km	135.74 km	0.00 %	1.01 %
MAX heat-up*	43.64 km	43.64 km	22.9 %	25.07 %
MAX cool-down*	35.37 km	35.37 km	80.5 %	81.96 %

*Constant vehicle speed at 40 km/h

To identify the energy flows of the reference EV and the improved QUIET vehicle, the validated entire vehicle model was used to fine-tune various key parameters (e.g. reduction of the energy consumption of auxiliaries or weight reduction of vehicle components, etc.). By varying systematically, the key parameters (e.g. the weight of vehicle components) the energy flow needed for air conditioning or the energy flow needed for heating of the vehicle in the vehicle model can be identified and outperforming impacts became visible (the summary of all analysis findings was submitted as deliverable D1.2 - Improvement potentials of reference e-vehicle, energy flow and energy consumption report).

2.2. Vehicle cabin model – thermal loads

For modelling the Honda Fit EV vehicle cabin model various thermal loads as depicted in Figure 2 are considered and implemented as source-models (e.g. short-wave solar radiation or long-wave body radiation) which are interlinked (via convection, conduction, radiation) to the sink-models, correspondingly (cp. Figure 3, right), whereas obstructed view factors between surfaces are calculated for correct consideration of the radiation.

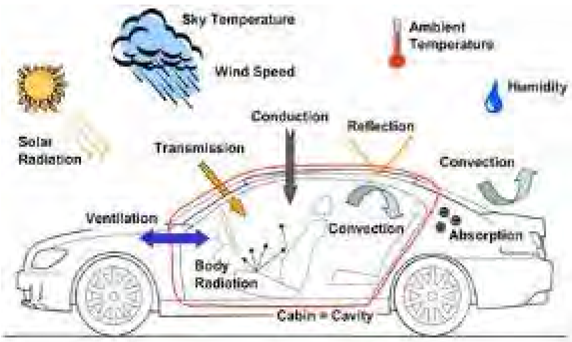

Figure 2: Thermal loads on a vehicle, including radiation, convection and conduction [8]

In T1.4 the development and implementation activities of models for thermal design of the HVAC system for the QUIET reference vehicle have been initiated and pursued in T2.2.
For modelling the Honda Fit EV vehicle cabin model various thermal loads were considered and implemented as source-models (e.g. short-wave solar radiation or long-wave body radiation) which are interlinked (via convection, conduction, radiation) to the sink-models, correspondingly (cp. Figure 3, right), whereas obstructed view factors between surfaces are calculated for correct consideration of the radiation.
The specific goals were the reduction of the complexity of a passenger cabin model of a vehicle down to only a few control volumes by keeping a reasonable accuracy. Therefore, models for the simulation of flows in closed and confined spaces were developed. These models allow the representation of a 3D air flow simulation

This project has received funding from the European Union's Horizon 2020 research and innovation programme under grant agreement No. 769826. The content of this publication is the sole responsibility of the Consortium partners listed herein and does not necessarily represent the view of the European Commission or its services.

in a very simplified way. The model consists of zones that have flow connectors in each spatial direction and are interconnected by flow models for each direction, cp. Figure 3, left and middle. In each zone, the conservation of mass and energy is handled. In the air flow model, flow resistances like pressure difference, momentum difference, gravitation and viscous forces are considered. To be able to simulate a vehicle cabin also humidity is considered which allows identifying the tendency of condensation on surfaces. Sources and sinks as well as boundary condition models allow to build up complete models for simulating the flow distribution in an overall vehicle cabin. Figure 3, right shows an illustrative model consisting of e.g. four zones, two flow models in x and two in y direction, two flow models to connect to the source and sink and a boundary condition with output pressure. The z-dimension is neglected here but the extension in z-direction is also possible.

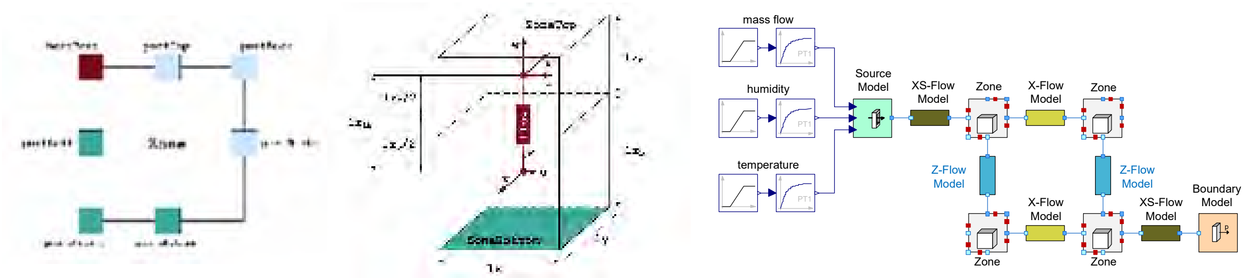

Figure 3: Zonal model (left), interconnection of two zones with a flow model (middle), illustrative Dymola model with e.g. 4 zones, 2 flow models, 1 source, 1 sink and 1 pressure boundary condition model (right).

2.2.1. Vehicle cabin model – zones

In Figure 4 left, the spatial arrangement of the developed 1D air flow zonal models (including pressure, temperature and humidity states of the media) within the Honda Fit EV reference vehicle cabin model is depicted, whereas here the extension in z-direction becomes apparent as shown in Figure 4, right.

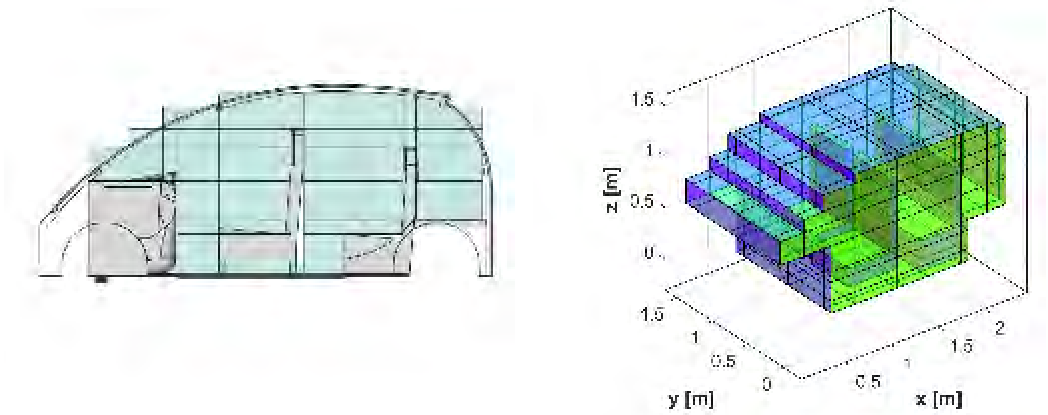

Figure 4: Zonal Model for the simulation of temperature- and flow distribution in the vehicle cabin (left) and its spatial layout in x-, y- and z-direction.

The zones are enclosed by models of the car body (walls, windows, roof, floor, etc.) considering conduction, convection and radiation effects. The vehicle cabin model can be used e.g. for a realistic temperature estimation in each zone and hence for the estimation of the Heating- and Air Condition energy demand of the QUIET reference vehicle. The integration of the air flow models into the Modelica vehicle model and the simulation of the combined models led unexpectedly to high processing efforts. This circumstance made it impossible (as originally envisaged) to perform a fast-combined analysis of the cabin comfort and the energy consumption of the vehicle for different operating conditions.

This project has received funding from the European Union's Horizon 2020 research and innovation programme under grant agreement No. 769826. The content of this publication is the sole responsibility of the Consortium partners listed herein and does not necessarily represent the view of the European Commission or its services.

2.3. Heating, Ventilation and Air Conditioning (HVAC) model – thermal vehicle model

The fact that the zonal modal will lead to high computing effort when combined with other models, has led to the approach, to develop an even more simplified cabin model ready to be used in the Heating, Ventilation and Air Conditioning (HVAC) model. The steps performed during the development of the HVAC model will be explained in the next paragraphs.

2.3.1. Thermal vehicle surfaces

The simplified cabin model encompasses the most relevant interfaces between chassis and ambient which can further be used in the HVAC model. These most important interfaces between chassis and ambient are represented by the thermal vehicle surfaces which can be separated (abstracted) into different areas as depicted in Figure 5.

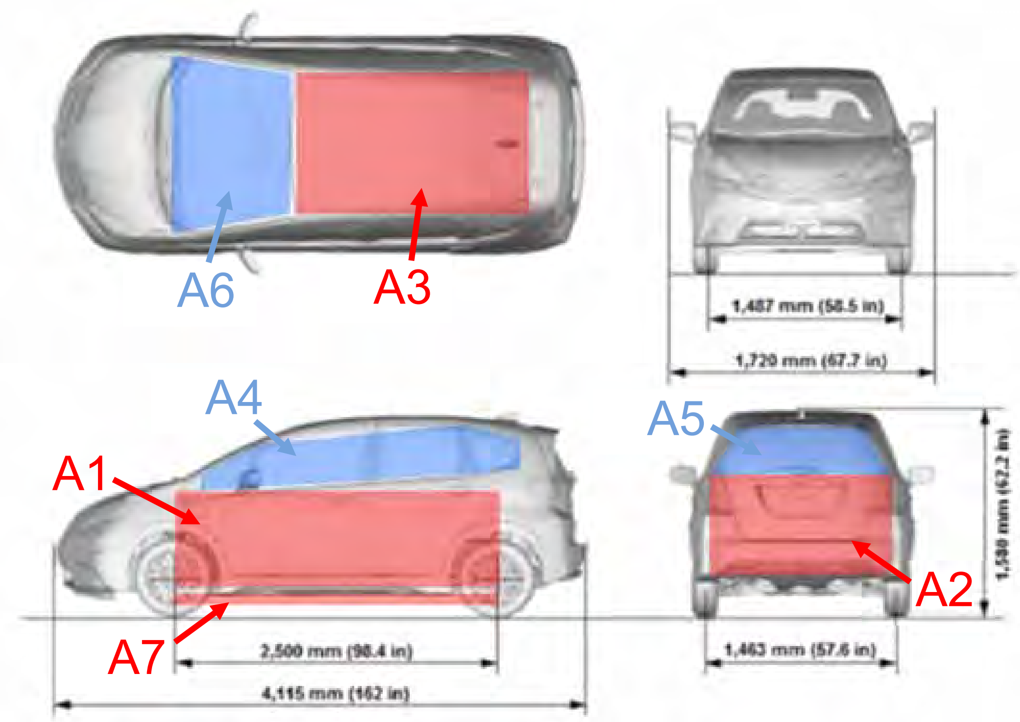

Figure 5: Thermal vehicle outer surfaces of the Honda Fit EV

The illustrated most relevant thermal vehicle outer surfaces are:

- A1: Side doors
- A2: Back door
- A3: Roof
- A4: Side windows
- A5: Back windows
- A6: Windscreen
- A7: Vehicle floor

The simplified cabin model enables on one hand the consideration of conduction, convection and radiation occurring on the surfaces, as well as the characteristics of the different surface materials on the other hand.

This project has received funding from the European Union's Horizon 2020 research and innovation programme under grant agreement No. 769826. The content of this publication is the sole responsibility of the Consortium partners listed herein and does not necessarily represent the view of the European Commission or its services.

2.3.2. Thermal vehicle model – convection model

To consider the thermal vehicle surfaces in the thermal models, convection models were developed. These models allow the calculation of convection parameter-sets, which are used to model convection effects on both, outer and inner surfaces. Figure 6 depicts convection models for (generalised) different surface alignments and flow directions.
The convection models can be used in bidirectional mode and are considering beside thermal convection also thermal conduction according to (1) and radiation according to (2),

$$\dot{q} = G \cdot \Delta T, \tag{1}$$

$$\dot{q} = G_r \cdot \sigma \cdot (T_1^4 - T_2^4), \tag{2}$$

where G denotes the conductance, G_r the radiation conductance and σ the Stefan-Boltzmann constant (the parameter G_r may be determined by measurements and is assumed to be constant over the range of operations).

The thermal convection parameters can be calculated according to equation (3),

$$\dot{q} = G_c \cdot \Delta T, \tag{3}$$

whereas G_c denotes convection conductance. The convection conductance, which is nearly never constant in practice, is a function of the surface area (*A*), the specific Reynolds number (*Re*: used to predict flow patterns in different fluid flow situations), the Prandtl number (*Pr*: ratio of momentum diffusivity to thermal diffusivity), the Grashof number (*Gr*: approximates the ratio of the weight of a displaced fluid to the viscous force acting on a fluid), the Rayleigh number (*Ra*: associates free or natural convection effects) and the Nußelt number (*Nu*: the ratio of convective to conductive heat transfer at a boundary in a fluid). By considering these set of numbers, the dynamic physical properties of air and fluids can be taken into account:

- Laminar / turbulent
- Free and forced convection (e.g. outside vehicle with v > 0 km/h), three different types:
    - Vertical plate
    - Horizontal plate (heat top side / cool bottom side)
    - Horizontal plate (heat bottom side / cool top side)

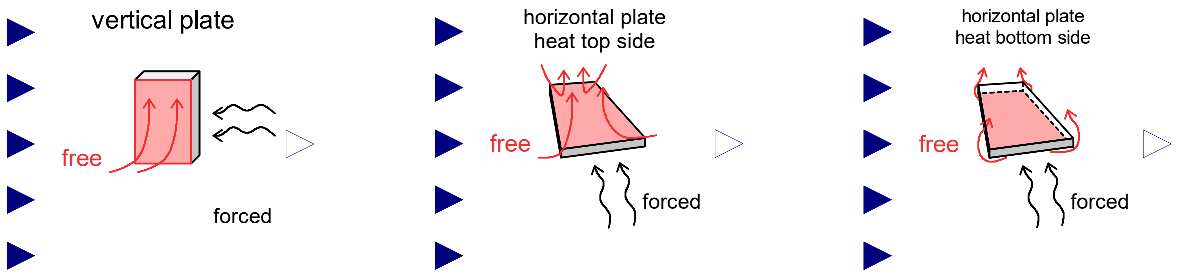

Figure 6: Convection model implemented in Modelica/Dymola applicable for outer and inner surfaces, e.g.: vertical plate (left), horizontal plate (heat top side / cool bottom side) (middle), horizontal plate (heat bottom side / cool top side) (right)

This project has received funding from the European Union's Horizon 2020 research and innovation programme under grant agreement No. 769826. The content of this publication is the sole responsibility of the Consortium partners listed herein and does not necessarily represent the view of the European Commission or its services.

2.3.3. Thermal vehicle model – initial approach

Figure 7 depicts the initial approach to develop a thermal vehicle model for heating mode in Dymola/Modelica using only components from the Modelica Standard Library (MSL) [1]. The approach assumes that flow effects are neglected by considering the total energy balance of the system only using thermal capacities and thermal coupling coefficients (i.e. thermal conductance, convection, radiation). The advantages are that the thermal vehicle model can be straightforwardly set-up to test the key-functionalities of the system (due to the neglection of flow effects the system becomes more easily comprehensible) and that plausibility checks can be performed. The disadvantages are that phenomenological impacts like pressure drops in the heating circuits (e.g. water circuit, air circuit) cannot be investigated due the mentioned non-consideration of flow effects.

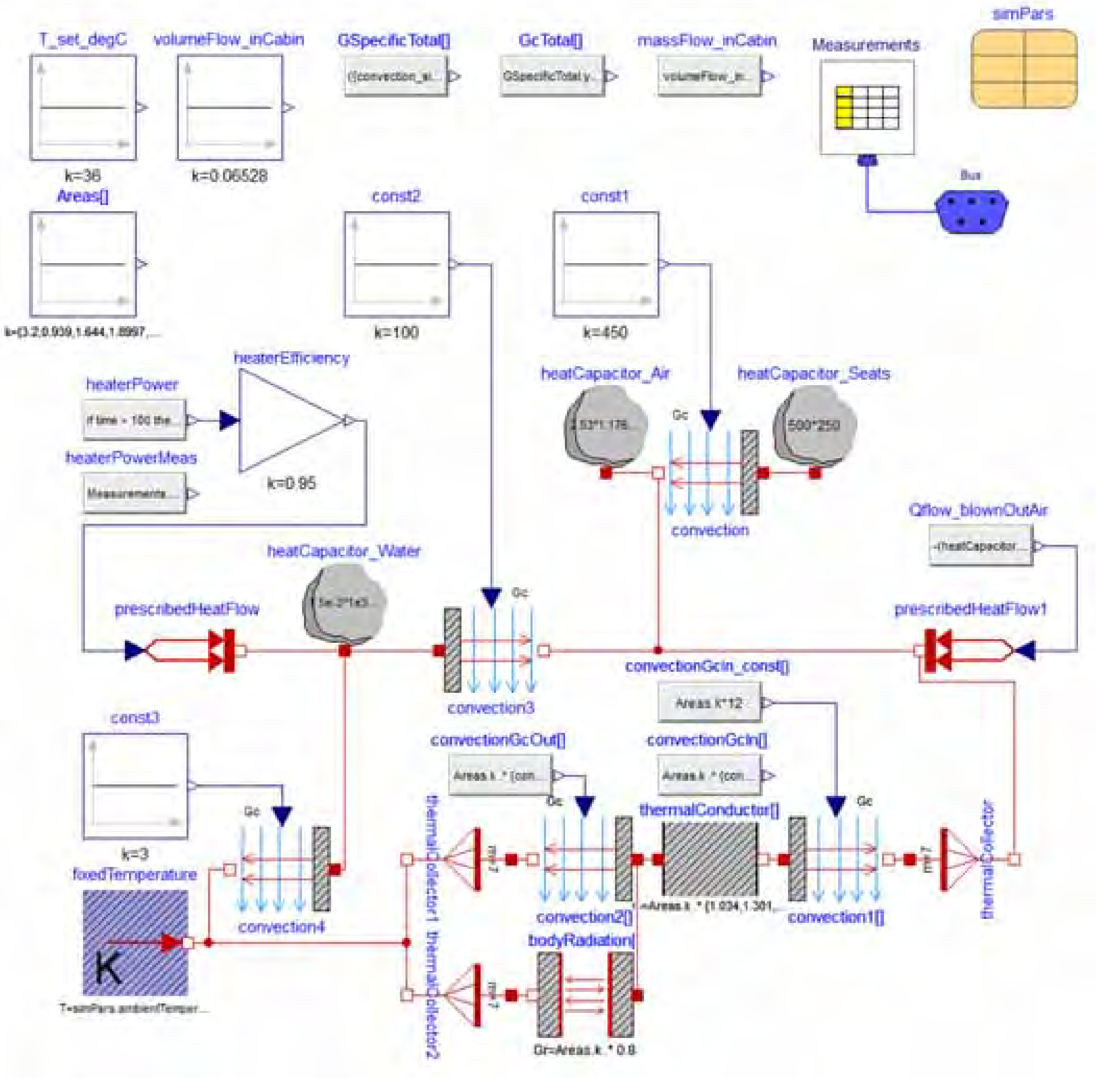

Figure 7: Thermal vehicle model for heating mode (initial approach) using only components from the MSL

The presented initial approach enables to investigate the main effects for energy balance in heating mode. The 3 depicted thermal capacities are implemented for water, air and for the seats/interior, respectively. In this model the air is blown out in fresh mode and it is modeled with dynamic physical properties according to the equations (1), (2) and (3). The thermal capacities and the thermal coupling coefficients (for convection and radiation to ambient) have been parameterised separately for water, air and for the seats/interior using measurement data from AVL and HRE.

This project has received funding from the European Union's Horizon 2020 research and innovation programme under grant agreement No. 769826. The content of this publication is the sole responsibility of the Consortium partners listed herein and does not necessarily represent the view of the European Commission or its services.

2.3.4. Thermal vehicle model – advanced approach

Figure 8 depicts an advanced approach for the thermal vehicle model (heating mode) in Dymola/Modelica using (beside the standard components from the MSL) additional components from the model library TIL Suite [2]. TIL is a commercial library for steady-state and transient simulation of thermodynamic systems. The thermodynamic properties are obtained through TILMedia, a library for the calculation of thermophysical substance properties, providing an interface with the Modelica Media library (MSL). The TIL library includes a variety of models for thermodynamic components (e.g. heat exchangers, pumps, expanders).
The decision to access solutions from the model library TIL Suite was taken to introduce physical thermodynamic component models (which are comparatively easy to use) in the QUIET thermal vehicle model. With the now possible consideration of flow effects phenomenological impacts like pressure drops e.g. in the air paths (cp. the Δp-elements in the orange-coloured connection path between "gasPort_in" and "gasPort_out" in Figure 8; the air path is modelled physically correct by considering the air flow masses) can be investigated as well.

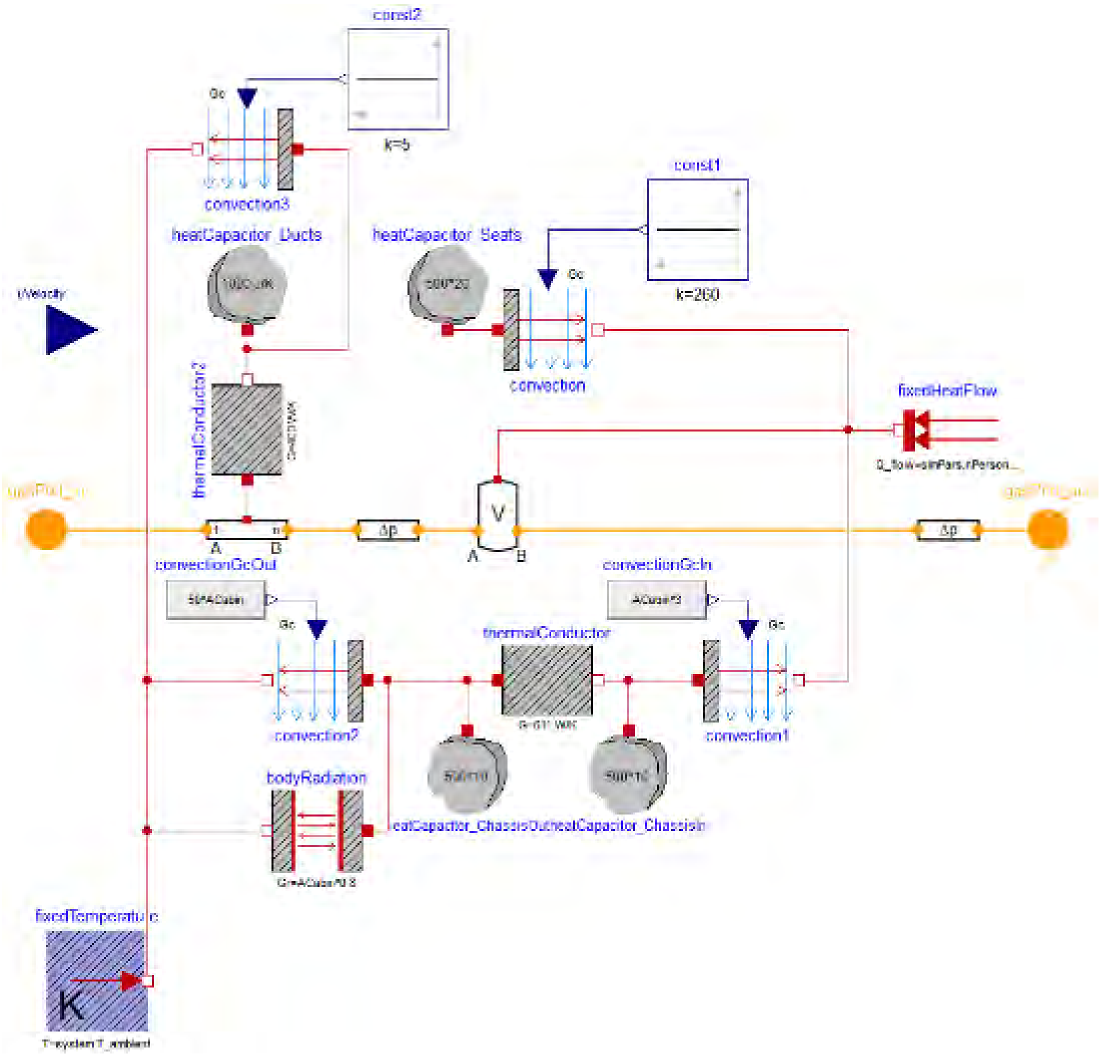

Figure 8: Advanced thermal vehicle model (air path considers also air flow effects)

The presented advanced approach enables (beside the main effects for energy balance in heating mode) also the investigation of flow effects during cooling and heating mode (in fresh air mode) whereby the air characteristics were modelled considering dynamic physical properties. The convection models introduced in

This project has received funding from the European Union's Horizon 2020 research and innovation programme under grant agreement No. 769826. The content of this publication is the sole responsibility of the Consortium partners listed herein and does not necessarily represent the view of the European Commission or its services.

subchapter 2.3.2 allow the continuous calculation of convection parameter-sets during the simulation of the thermal vehicle model. Since the calculated values of the parameter-sets are not varying widely over time and for the benefit of faster computing the convection models were replaced by simplified interfaces (between chassis and ambient) using corresponding mean values instead of calculating permanently parameter-sets. The physical heater core model has been parameterised with geometrical data using data provided by HRE-G.

2.3.5. Results – HVAC modelling

In order to investigate the operating behaviour of the HVAC system in different application scenarios (i.e. heat pump operation at low ambient temperatures and cooling operation at high ambient temperatures), an entire HVAC model has been implemented in Dymola/Modelica using components from the commercial TIL library. The implemented model is depicted in Figure 9 and will be described more in detail later in this section.

This project has received funding from the European Union's Horizon 2020 research and innovation programme under grant agreement No. 769826. The content of this publication is the sole responsibility of the Consortium partners listed herein and does not necessarily represent the view of the European Commission or its services.

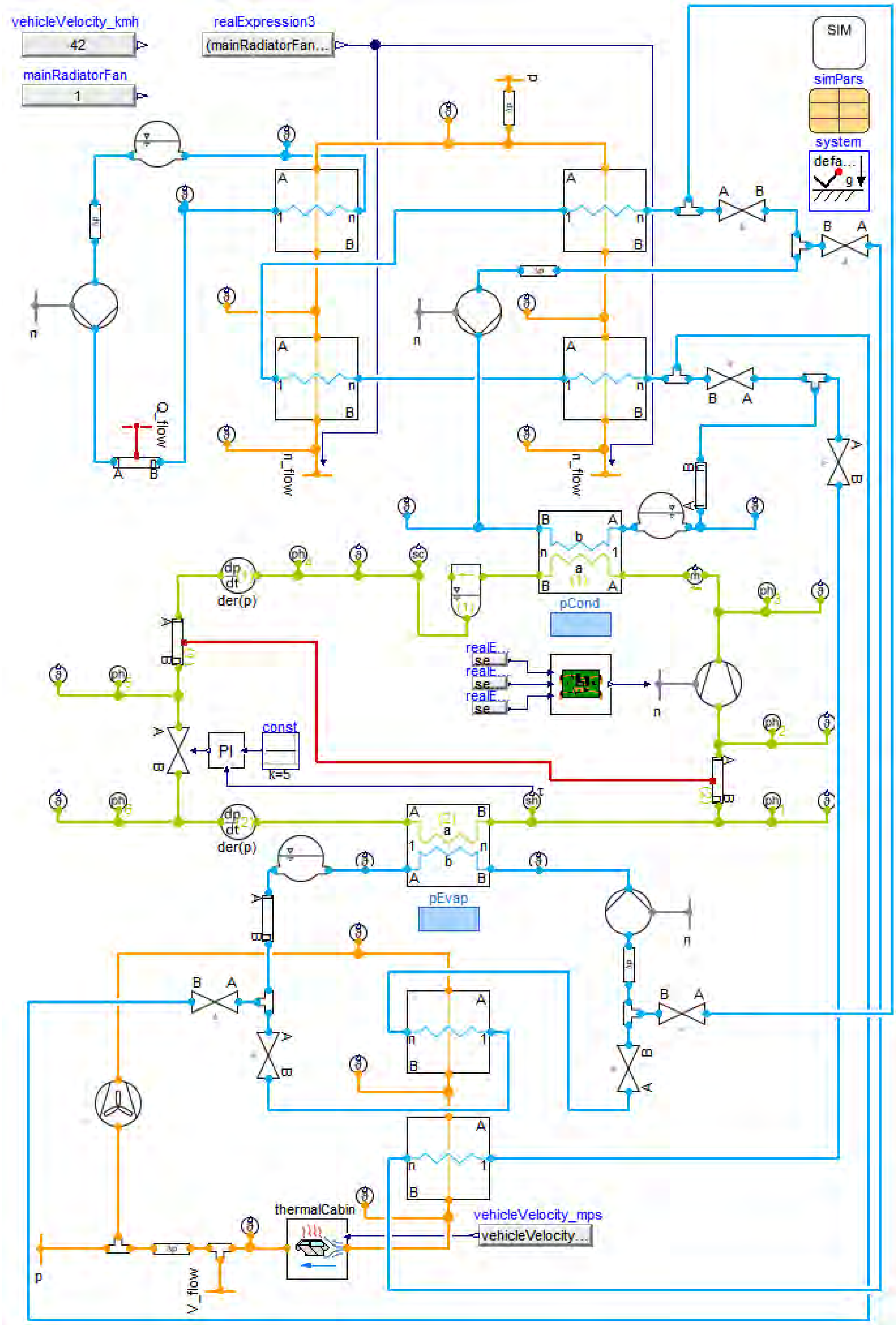

Figure 9: Entire HVAC model

In the first step, each single component has been parameterised separately. Therefore, measurement data from AVL and HRE have been used. The boundary conditions, such as pressure and temperature, in different

This project has received funding from the European Union's Horizon 2020 research and innovation programme under grant agreement No. 769826. The content of this publication is the sole responsibility of the Consortium partners listed herein and does not necessarily represent the view of the European Commission or its services.

operating points have been defined based on the measurements. Then, characteristic quantities that are relevant for the respective component (i.e. mass flow, heat transfer, outlet temperature, outlet pressure) have been analysed during simulation. Based on the comparison between measured and simulated values, the quality of the chosen model parameters can be determined. The parameter tuning process is a very extended process with a lot of iterations when varying the model parameters. Therefore, an automated adaptive tree search algorithm which has been implemented by the AIT for parameter tuning tasks has been used.

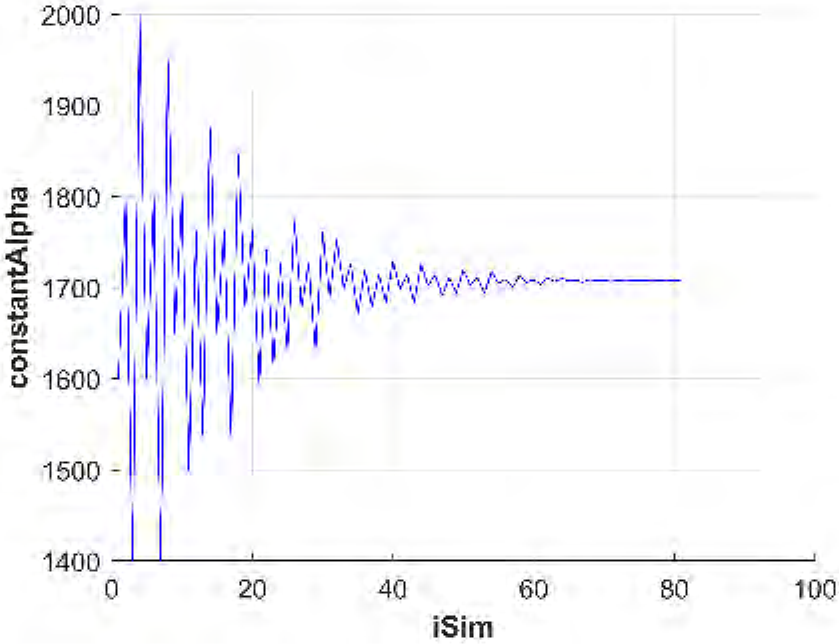

Figure 10: Condenser heat transfer optimisation – constant heat transfer coefficient

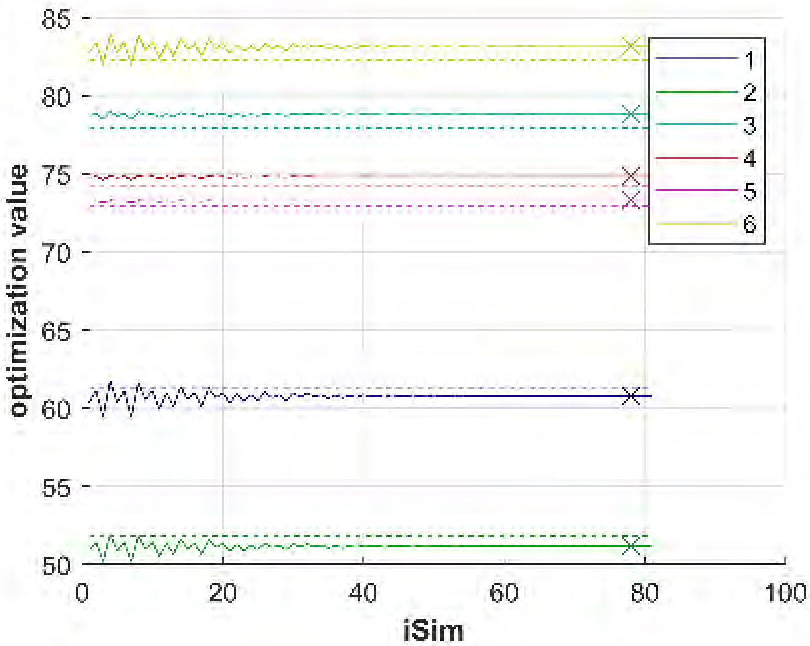

Figure 11: Condenser heat transfer optimisation – comparison of target values and simulation

This project has received funding from the European Union's Horizon 2020 research and innovation programme under grant agreement No. 769826. The content of this publication is the sole responsibility of the Consortium partners listed herein and does not necessarily represent the view of the European Commission or its services.

Figure 10 and Figure 11 show one representative result of the parameter tuning algorithm. For the condenser model, the constant heat transfer coefficient has been varied to find a parameter value, which minimises the error between measurement and simulation in different operating points at the same time. Figure 10 represents the variation of the heat transfer coefficient parameter while Figure 11 depicts the simulated (solid) and measured values (dotted) for the heat transfer of the condenser in six different operating points. The same procedure has been applied to find the parameters of all the other components in the HVAC system.

In the next step, the single models have been connected step-by-step to get the final HVAC model, which is depicted in Figure 9. The model is structured in three different parts: refrigerant cycle (green), water cycles (blue) and air cycles (orange). The refrigerant cycle considers the compressor, condenser, separator, internal heat exchanger, expansion valve and evaporator. The water cycles (for cooling power electronics and for HVAC system) consist of the water side of the condenser, evaporator and front heat exchanger, a PTC heater, pumps and valves. By switching the water cycle valves the refrigerant cycle can be either used in cooling or in heat pump mode. The air cycle considers the front heat exchanger (the heat exchanger is divided into four parts, where one quarter is used for the power electronics and three quarters are used for the HVAC system), the cabin heat exchangers (heater core and low temperature radiator), the front vehicle fan and cabin fan and a cabin volume.

Finally, the total cycle has been validated as a whole system. Therefore, again, the measurement data has been compared to the simulation results. The Validation has been performed for one operating point in cooling mode (at 40 °C ambient temperature) and for one operating point in heat pump mode (at -10 °C ambient temperature). The validation of the HVAC model based on p,h diagrams can be seen in Figure 12 for the cooling mode (blue) and for the heat pump mode (red). In the figure, the grey line is the saturation line of propane, the dashed lines represent the measurements and the solid lines represent the respective simulation results. The results show a very good coherence between the measurement and simulation.

The validated HVAC model has been delivered from AIT to UOZ for determining an optimal vehicle energy management strategy.

In the further course of the project, the developed HVAC model will be used to validate the optimised operating strategy of Task 2.3. The model can be further used for assessing the cooling and heating performance in different application scenarios which cannot be measured directly. Additionally, the model will be used to develop and test the hardware control algorithm for the HVAC components. The control algorithm will be implemented in the programming language Python. Via Socket interfaces, the algorithms in Python can communicate with the Dymola model to set the control variables of the different sub components (e.g. compressor speed, expansion valve opening, speed of the water pumps, fan speeds, etc.). Hence, the software interface can be used to investigate the validity of the control algorithms in a virtual environment. With this approach, the basic functionality of the control algorithms can be tested in advance, even before the whole HVAC system has been set up in hardware. This will enable an improved development speed of the HVAC control system.

This project has received funding from the European Union's Horizon 2020 research and innovation programme under grant agreement No. 769826. The content of this publication is the sole responsibility of the Consortium partners listed herein and does not necessarily represent the view of the European Commission or its services.

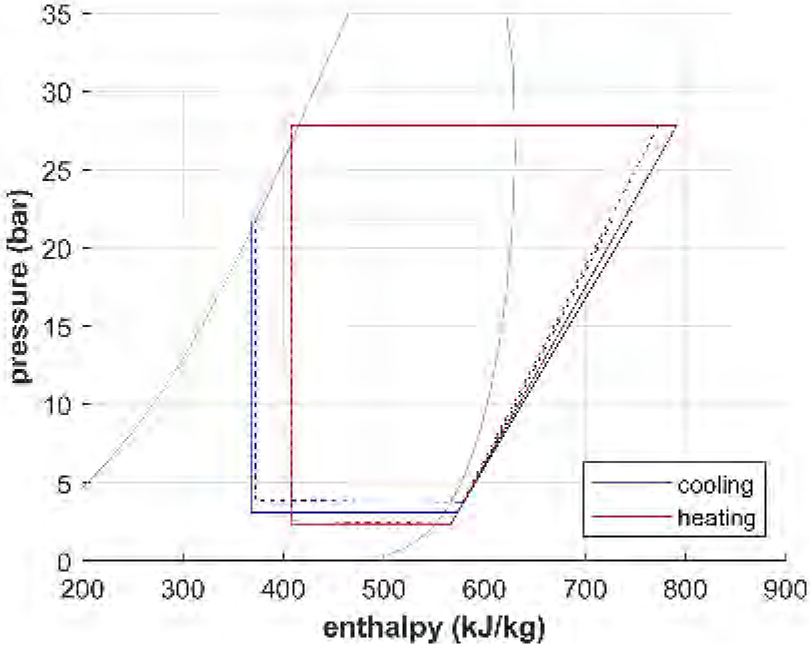

Figure 12: Total cycle validation AC mode (blue) and heat pump mode (red). The grey line is the saturation line of propane; the dashed lines represent the measurements and the solid lines represent the respective simulation results

2.3.6. Results – temperatures

Figure 13 depicts the comparison between the measured temperature in the passenger compartment (by data provided by HRE-G, blue curve: 'TcabinMeas') and the corresponding simulated cabin temperature 'TcabinSim' (red curve) confirming the validity of the developed thermal vehicle model (the validation was performed by comparison with measured temperatures at different locations in the cabin). Moreover, the simulated temperature profile of the water (temperature of coolant, green curve: 'TwaterSim') is depicted. The starting condition for all temperature profiles considers -10 °C ambient temperature followed by a heat up of passenger cabin applying a Worldwide harmonized Light vehicles Test Cycle (WLTC).

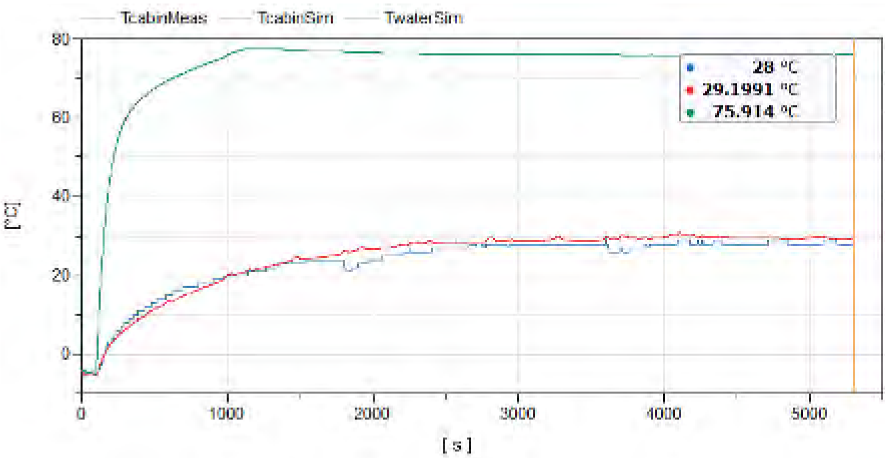

Figure 13: Comparison between measured (blue curve) and simulated (red curve) cabin temperature and temperature profile of coolant water (green curve)

This project has received funding from the European Union's Horizon 2020 research and innovation programme under grant agreement No. 769826. The content of this publication is the sole responsibility of the Consortium partners listed herein and does not necessarily represent the view of the European Commission or its services.

2.3.7. Results – thermal losses

Figure 14, left, depicts the heat flow (i.e. thermal losses) at different surfaces (A1 to A7) where glazed surfaces are accentuated in color blue and the other relevant surfaces in color red. The highest thermal losses were identified at the side windows (A4), the least thermal losses were determined for the vehicle floor (A7). This can be explained by the fact that the battery pack is mounted on the vehicle floor and acts as an insulator. The results are quantified also in Figure 14, right, impacting to improve components e.g. by replacing existing glass windows with polycarbonate glazing in order to save improper thermal losses at the problematic surfaces (A4, A5, A6) and to insulate e.g. doors with composite materials. The wattages outlined in the legend of Figure 14, right, are corresponding with the numbering of the surfaces with related color-labels / colored curve profiles (e.g. 1st value from top i.e. blue marker/curve: A1, 2nd value from top i.e. red marker/curve: A2, ..., 7th value from top i.e. orange marker/curve: A7).

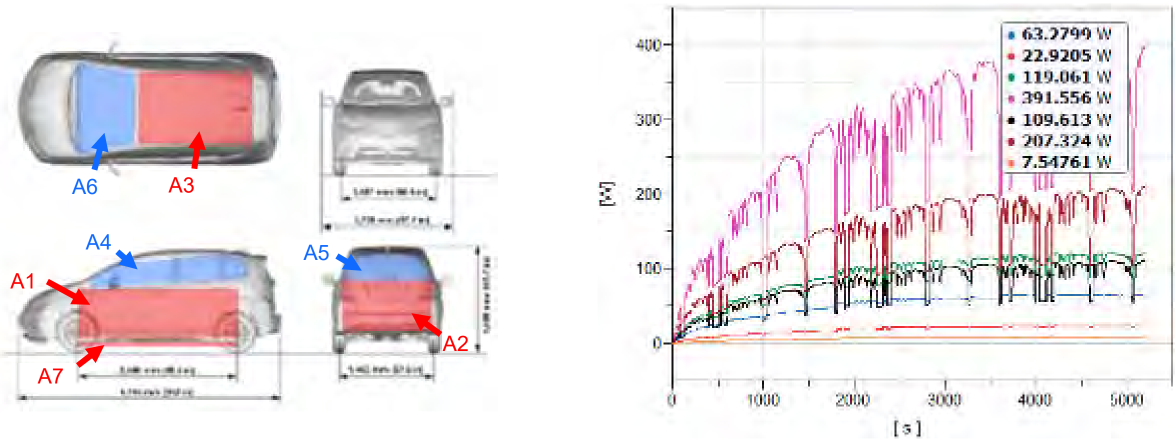

Figure 14: Thermal losses: relevant surfaces (left) and their quantification in Watt (right)

2.3.8. Results – lost thermal energy

Figure 15, left, depicts the cumulated lost thermal energy at different surfaces (i.e. at chassis and windows with 1st value from top i.e. blue marker/curve: A1 to 7th value from top i.e. orange marker/curve: A7). In the figure on the right, the cumulated thermal energy losses via these surfaces (cp. 3rd value from top i.e. green marker/curve with 0.933614 kWh). The cumulated thermal energy losses due to air, which is blown out of the vehicle in fresh air mode are depicted in Figure 15, right (2nd value from top i.e. red marker/curve with 0.586235 kWh) and compared with the cumulated thermal energy losses over the surfaces (3rd value from top i.e. green marker/curve with 0.933614 kWh) and summarized to the total cumulated thermal energy losses (via surfaces and blown out air, 1st value from top i.e. blue marker/curve with 1.51985 kWh).

This project has received funding from the European Union's Horizon 2020 research and innovation programme under grant agreement No. 769826. The content of this publication is the sole responsibility of the Consortium partners listed herein and does not necessarily represent the view of the European Commission or its services.

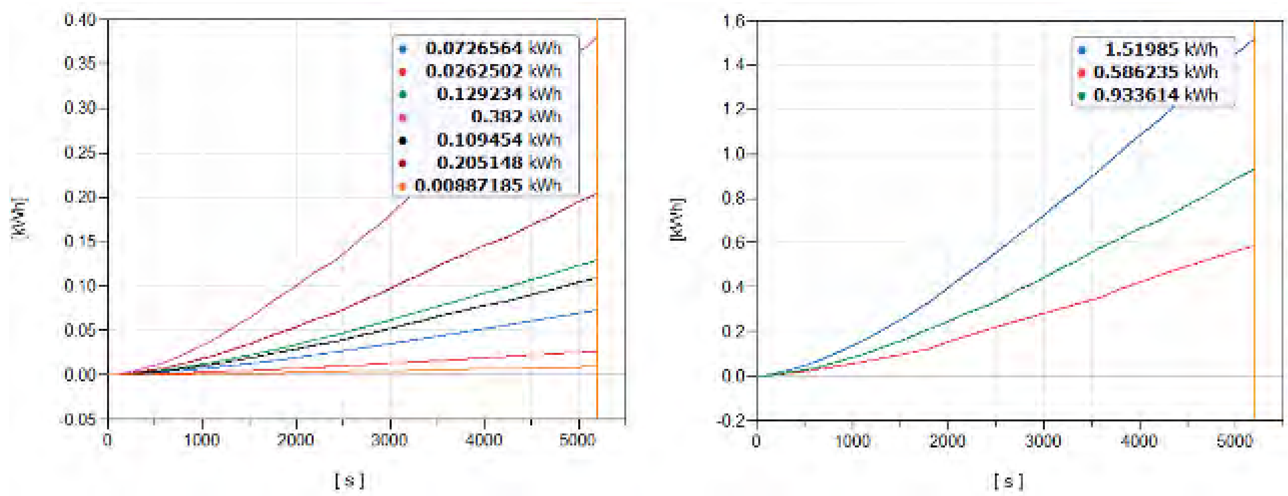

Figure 15: Lost thermal energy using standard glazing at different surfaces (left) and total (right)

Again, the results are impacting to improve components e.g. by replacing existing glass windows with polycarbonate glazing in order to save improper thermal losses at the problematic surfaces (A4, A5, A6).
With the developed thermal vehicle models e.g., the difference between glass and polycarbonate can be elaborated. The improvements by using polycarbonate instead of glass windows are depicted in Figure 16, left (cumulated thermal losses). Figure 16 shows on the right a comparison between the cabin air of the vehicle with standard glazing (blue) and the cabin air of the vehicle with polycarbonate glazing (red). The results show that the novel glazing can lead to lower cabin temperatures in summer conditions by approximately 0.5 °C.

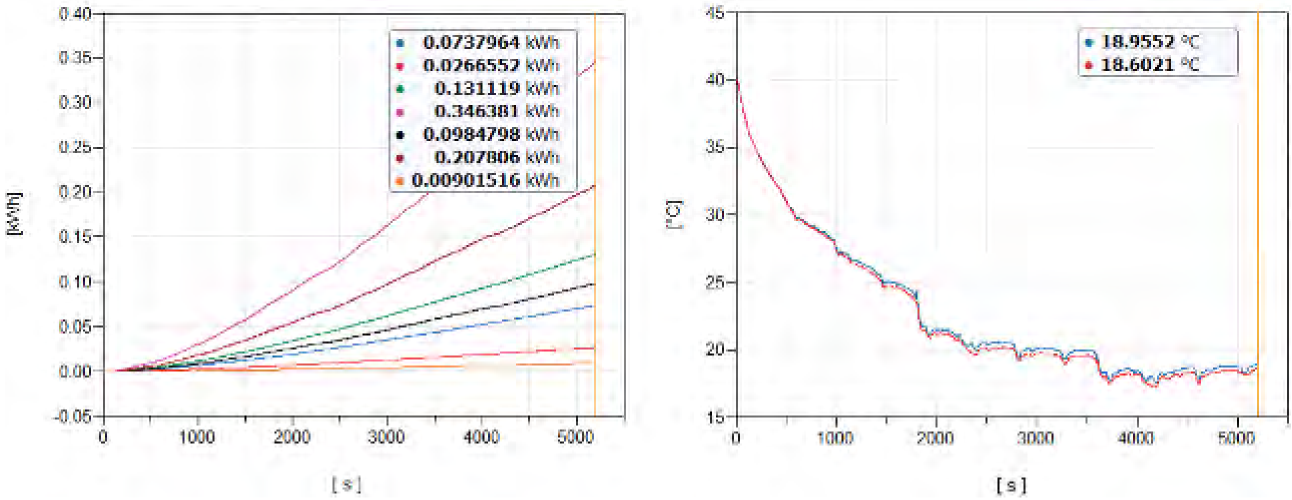

Figure 16: Lost thermal energy using polycarbonate glazing at different surfaces (left) and cabin temperature comparison between standard- and polycarbonate glazing (right)

This project has received funding from the European Union's Horizon 2020 research and innovation programme under grant agreement No. 769826. The content of this publication is the sole responsibility of the Consortium partners listed herein and does not necessarily represent the view of the European Commission or its services.

3. Optimal vehicle energy management strategy for user comfort

The multi-physical model presented in Section 2 is too complex for control design purposes. Therefore, a control-oriented model is firstly established to facilitate the development of numerical tools for control design. The first part of the section (Subsections 3.1. to 3.4.) documents control-oriented HVAC modelling, development of numerical tools for control design and control strategy development and verification on control-oriented model. Developed numerical tools that aid control design include model static mapping, linearization and parameter identification. Dynamic programming control trajectory tool applied to first-order vehicle cabin model and static HVAC model is used to produce the thermal comfort and efficiency benchmark and provide guidelines for cabin thermal comfort control strategy development that is presented in the same subsection. The proposed hierarchical control structure consists of a superimposed cabin air temperature controller that commands the cooling capacity, optimisation-based control allocation algorithm, and inner HVAC control loops. Control allocation sets references for optimised low-level HVAC feedback controllers and also determines auxiliary control variables such as air mass flow rates by maximising thermal comfort and efficiency, while satisfying HVAC system constraints. Control trajectory optimisation is conducted for a cool-down scenario, and the control strategy performance is verified through simulations for same scenario.

The second part of the section (Subsections 3.5 to 3.8) documents the application of the aforementioned tools and hierarchical control strategy to more complex (target) HVAC system described in Section 2. The developed multi-objective optimisation approach is applied for generating the control allocation maps, which are finally implemented in target HVAC system model in the form of analytical functions and validated for both the cooling and heating operating modes.

3.1. Control-oriented modelling and analysis tools

3.1.1. 12th-order vapour-compression cycle (VCC) model

HVAC system working in air-conditioning (cooling) mode or as a heat pump (heating mode) is based on the vapour compression cycle. The designed VCC model is based on a single-fluid single-stage circuit, with the R-134a as a working fluid. The VCC configuration is shown in Figure 17 uses a variable-speed fixed-displacement compressor for compression, an electronic expansion valve (EXV) for throttling, and two cross-flow heat exchangers for thermal energy exchange between refrigerant, tube wall and an unmixed air-stream. Air stream is supplied to evaporator and condenser by a blower fan and an axial fan, respectively. For simplicity, air mass flow rates instead of fan blade speeds are considered as inputs.

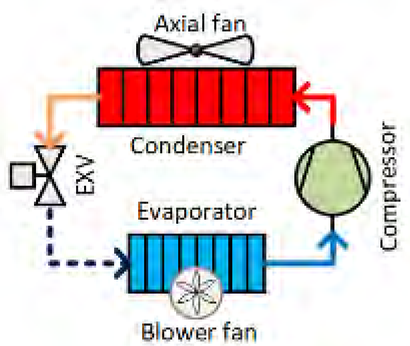

Figure 17: Typical vehicle air-conditioning configuration

Thermal energy exchange of the heat exchangers represents dominant system dynamics. Actuator dynamics are faster by an order of magnitude of the heat exchanger dynamics and can be modelled as static expressions

This project has received funding from the European Union's Horizon 2020 research and innovation programme under grant agreement No. 769826. The content of this publication is the sole responsibility of the Consortium partners listed herein and does not necessarily represent the view of the European Commission or its services.

[11]. The heat exchanger model is based on the moving-boundary model method [12]. The model is suitable only for operating conditions where all nodes are present, since model switching method is not included [13]. An extensive list of symbols used in the model presentation is given in Table 2 in section Abbreviations and Nomenclature.

3.1.2. Actuator models

Static, efficiency based model of reciprocating compressor with clearance is used for refrigerant mass flow rate calculation [14]–[16]:

$$\dot{m}_{com} = \omega_{com} V_{sw} \rho_s \left(1 + C_{com} - C_{com} \left(\frac{p_d}{p_s} \right)^{\frac{1}{n}} \right) \tag{4}$$

It is assumed that the compression process is adiabatic and with constant efficiencies connecting the inlet and outlet enthalpies:

$$h_d = \frac{h_{is} - h_s}{\eta_{is}} + h_s \tag{5}$$

Simplified expansion valve model is adopted from [11], [18], [19], where the mass flow rate through the valve is defined as:

$$\dot{m}_v = a_v C_v A_v \sqrt{\rho_l (p_c - p_e)} \tag{6}$$

where the input value $a_v \in [0,1]$ determines the percentage of the valve opening.

3.1.3. Heat exchanger models

Heat exchanger models are based on principles of conservation of mass, energy and momentum. Several assumptions and restraints are introduced in order to simplify the complex nature of refrigerant flow and phase change. The working fluid flow is considered frictionless, one-dimensional and the thermal energy exchange between the refrigerant and the wall is considered isobaric. This eliminates the need for momentum conservation equations. The heat exchanger is modelled as a horizontal thin tube with constant cross-section area, with negligible axial and radial heat conduction, resulting in a uniform node wall temperature. Void fraction in the two-phase node that represents the quality of the two-phased mixture is considered time invariant. The thermal energy exchange between the wall and air is considered isobaric, air stream incompressible and ideally mixed at the outlet.

Considering these assumptions, the mass conservation equation can be written as:

$$\frac{\partial \rho}{\partial t} + \frac{\partial \dot{m}}{\partial x} = 0 \tag{7}$$

while the energy conservation equation reads:

$$\frac{\partial (\rho h - p)}{\partial t} + \frac{\delta (\dot{m} h)}{\delta x} = \dot{q} \tag{8}$$

The conservation equations are applied on the working fluid as well as on the tube wall. Integrating Eqs. (7) and (8) from one boundary of the heat exchanger, e.g. $x = 0$ (inlet), along the heat exchanger to the beginning of a next phase, e.g. $x = L_1$, is done by using the Leibnitz integral rule which eliminates the spatial dependence of system variables and results in time-dependant differential equations.

$$\int_{x_0}^{L_1(t)} A \frac{\partial \rho}{\partial t} dx + \int_{x_0}^{L_1(t)} \frac{\partial \dot{m}}{\partial x} dx = 0 \tag{9}$$

This project has received funding from the European Union's Horizon 2020 research and innovation programme under grant agreement No. 769826. The content of this publication is the sole responsibility of the Consortium partners listed herein and does not necessarily represent the view of the European Commission or its services.

$$\int_{x_0}^{L_1(t)} A \frac{\partial(\rho h)}{\partial t} dx - \int_{x_0}^{L_1(t)} Ap \, dx + \int_{x_0}^{L_1(t)} \frac{\partial(\dot{m}h)}{\partial x} dx = \int_{x_0}^{L_1(t)} \dot{q} \, dx \tag{10}$$

Thermophysical properties, e.g. density and temperature, are averaged for each node depending on the state of the refrigerant. Phase distribution within each heat exchanger along with their respective state variables and other important parameters for nominal operating conditions is depicted in Figure 18.

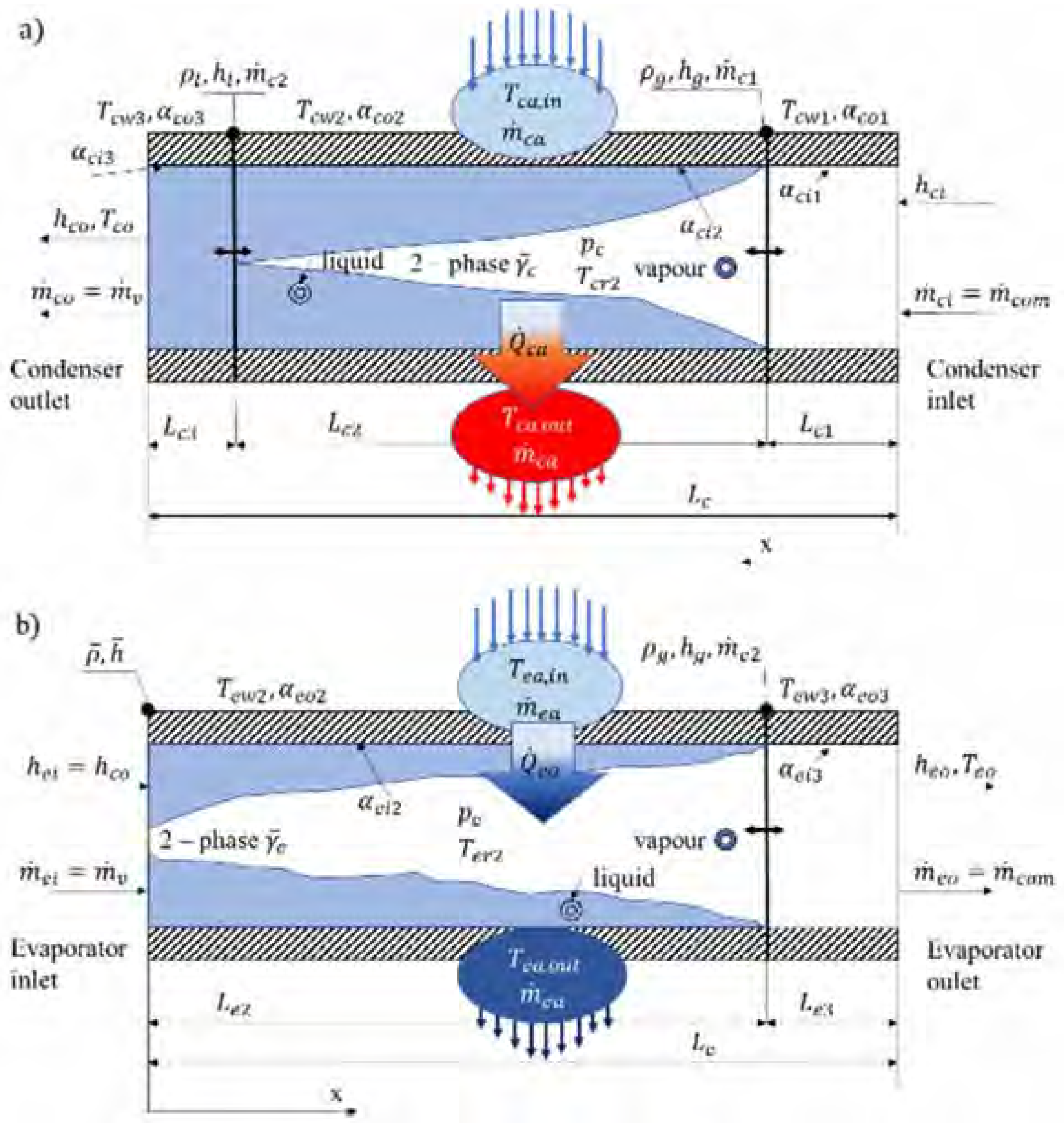

Figure 18: Heat exchanger node specific state variables and parameters

Repeating the integration process for the remaining two nodes and sorting the differential equations to eliminate intermediate mass flows $\dot{m}_1$ and $\dot{m}_2$ between the phases results in a nonlinear 7th order model written in matrix form:

$$\mathbf{A}(\mathbf{x})\dot{\mathbf{x}} = \mathbf{f}(\mathbf{x}, \mathbf{u}) \tag{11}$$

where the state variable vector

This project has received funding from the European Union's Horizon 2020 research and innovation programme under grant agreement No. 769826. The content of this publication is the sole responsibility of the Consortium partners listed herein and does not necessarily represent the view of the European Commission or its services.

$$\mathbf{x} = [L_1 \quad L_2 \quad p \quad h_o \quad T_{w1} \quad T_{w2} \quad T_{w3}]^T \tag{12}$$

includes the lengths of first two nodes L_1 and L_2, refrigerant pressure p, outlet specific enthalpy h_o, and node wall temperatures T_{w1}, T_{w2} and T_{w3}. The condenser model contains all three phases while the evaporator model contains only the two-phase node followed by the superheating node. Thus, the evaporator model is obtained by reducing the above model to a 5th order model (subcooling node length L_1 and wall temperature T_{w1} are omitted). The input vector **u**

$$\mathbf{u} = [\omega_{com} \quad a_v \quad \dot{m}_{ea} \quad \dot{m}_{ca}]^T \tag{13}$$

includes the compressor speed ω_{com}, valve opening a_v, and air mass flow rate over evaporator $\dot{m}_{ea}$ and condenser $\dot{m}_{ca}$. The thermal energy exchange between the refrigerant and heat exchanger wall for each node is given as:

$$\dot{Q}_{kr} = \dot{m}_{ki}h_{ki} - \dot{m}_{ko}h_{ko} = \pm\, \alpha_{ki}A_{ki}(\bar{T}_{kr} - T_{kw}) \tag{14}$$

while the thermal exchange between the wall and ambient air is calculated as:

$$\dot{Q}_{kw} = c_{p,a}\dot{m}_{ka}\left(T_{ka,in} - \bar{T}_{ka,out}\right) = \pm\, \alpha_{ko}A_{ko}(\bar{T}_{ka} - T_{kw}) \tag{15}$$

where index k can refer to either condenser or evaporator.

3.1.4. Overall VCC model

The complete 12th order VCC model is obtained by combining individual model equations, where an output of a model serves as an input to subsequent model and its set of equations (see Figure 19). The model is implemented in the MATLAB/Simulink environment. This enables the simulation as well as the use of different Matlab-embedded tools for linearization and control design. The CoolProp library [17] interface for MATLAB is used to obtain fluid properties by interpolating values from fluid-specific nonlinear thermodynamic tables. The CoolProp functions require at least two arguments, e.g. pressure and temperature to obtain the fluid thermodynamic property.

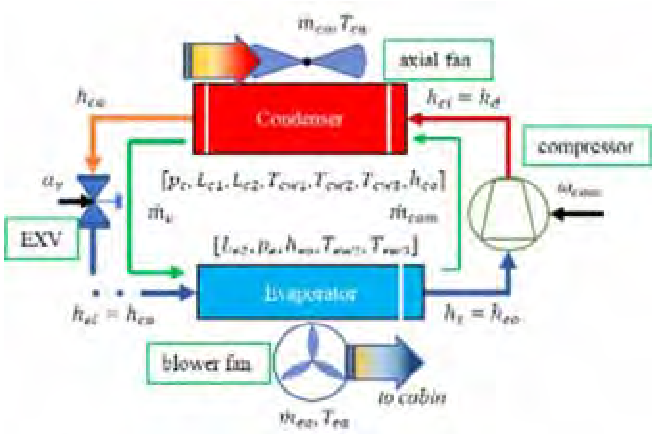

Figure 19: Schematic of the 12th order model of vapour compression cycle with corresponding state variables and control inputs. See **Table 2** for the nomenclature definition.

Expressions of all elements of the system matrix **A**, as well as the balance equation elements of the vector **f** for the evaporator and the condenser are given in the Appendix A1.

This project has received funding from the European Union's Horizon 2020 research and innovation programme under grant agreement No. 769826. The content of this publication is the sole responsibility of the Consortium partners listed herein and does not necessarily represent the view of the European Commission or its services.

3.2. Model reduction method

The highly nonlinear coupled dynamics of the 12th-order model makes it difficult to assess the effect of individual state variables on overall system dynamics and identify suitable states for reduction. However, it is known that the dominating dynamics of the process is that of thermal energy exchange, while the states associated with mass-transport process have faster dynamics [18]. Therefore, an analytical step-by-step reduction method is applied, gradually eliminating certain state variables. Each sub-sequent reduced model is derived from the higher-order model and inherits the previously introduced assumptions. Overview of all reduced-order models and introduced assumptions is given in Table 4. The reduced-order models are validated against the full 12th order model (R12).

Table 4: Overview of model order reduction steps and assumptions

Reduction step / model designation		**1 / R9**	**2 / R8**	**3 / R6**	**4 / R5**	**5 / R3**
Leading assumption		Uniform wall temperature	Static superheating node length	Static outlet spec. enthalpy	Static two-phase length	Equal wall and refrigerant temperature
State variables eliminated	Condenser	T_{cw1}, T_{cw2}, $T_{cw3} \rightarrow T_{cw}$	L_{c1}	h_{co}	L_{c2}	T_{cw}
	Evaporator	T_{ew2}, $T_{ew3} \rightarrow T_{ew}$	---	h_{eo}	---	T_{ew}
Final model order		9	8	6	5	3

3.2.1. Uniform heat exchanger wall temperature (R9)

The wall acts as a boundary between the refrigerant and ambient air stream, and the temperature gradient between the wall and those two fluids greatly influences the process dynamics. Introducing a uniform wall temperature T_{cw}, which replaces individual node-specific wall temperatures $T_{cw1,2,3}$, reduces the order by two for the condenser and one for evaporator resulting in a 9th order (R9) model. The reduction introduces a greater temperature difference between the wall and surrounding fluids, affecting overall thermal energy exchange and phase distribution. However, this can be mitigated by adjusting either (or both) the internal α_i and external α_o heat transfer coefficients to match the heat exchange of the 12th-order model.

3.2.2. Static condenser superheating node length Lc1 (R8)

In the nominal operating conditions, most of the thermal energy exchange occurs in the two-phase node. Therefore, the two-phase node L_{c2} dictates the dynamics while the length of the superheating node L_{c1} has minor effect on the overall condenser. Boundary conditions of the first node are defined by the remaining state variables p_c and T_{cw1} and its inlet h_{ci} and outlet h_{cg} enthalpies, enabling the replacement of the state-variable dynamics with a static expression:

$$L_{c1} = \frac{\dot{m}_{ci}\left(h_{ci} - h_{cg}\right)}{\alpha_{ci1} D_{ci} \pi (\overline{T}_{r1} - T_{cw})} \tag{16}$$

This reduces the model order to 8th order (R8).

This project has received funding from the European Union's Horizon 2020 research and innovation programme under grant agreement No. 769826. The content of this publication is the sole responsibility of the Consortium partners listed herein and does not necessarily represent the view of the European Commission or its services.

3.2.3. Static heat exchanger outlet specific enthalpy (R6)

Specific enthalpy at the outlet h_{ko} is a boundary condition that is a result of the slower, thermal energy exchange done in the heat exchanger and as such can be presumed static. The temperature at the heat exchanger outlet T_{ko} (from which the specific enthalpy can be obtained), can be determined by calculating the energy exchange between the refrigerant and the wall on the third node length L_{k3} (defined by other two nodes).

$$T_{ko} = \frac{2\alpha_{ki3}A_{ki}(L_k - L_{k2})T_{kw} + T_{kr2}\left(2c_{p,kr}\dot{m}_{kr} - \alpha_{ki3}A_{ki}(L_k - L_{k2})\right)}{2c_{kp,r}\dot{m}_{kr} + \alpha_{ki3}A_{ki}(L_k - L_{k2})} \tag{17}$$

$$h_{ko} = f(p_k, T_{ko}) \tag{18}$$

The specific enthalpy at the outlet is h_{ko} used to calculate the refrigerant density ρ_{ko} which in turn is used to determine the refrigerant mass flow rates (Eqs. (4) and (6)), thus forming an algebraic loop. This imposes a limitation on the reduced, 6th order model (R6), as a nonlinear dynamic model becomes viable only with the use of a memory block. Figure 20 shows the response of R12 and R6 (with memory blocks) to a step change in compressor and valve inputs (Figure 20e and f). The dominant, slow heat exchanger pressure dynamics (Figure 20a and b) are preserved after two steps of reduction. The difference in the evaporator outlet air $T_{ea,out}$ dynamics (Figure 20c) is caused by the uniform wall temperature T_{ew} introduced in R9.

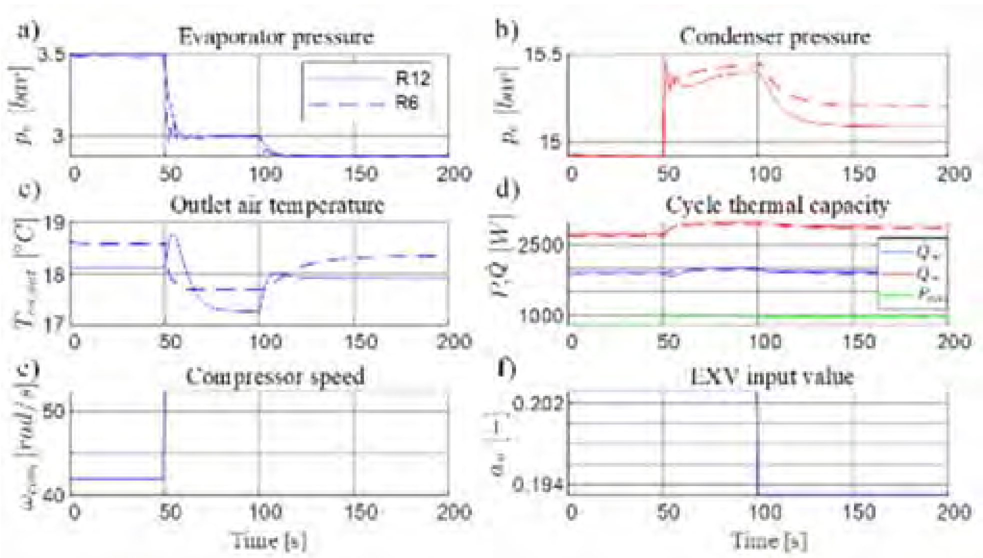

Figure 20. Response of nonlinear R12 and R6 (with memory blocks) models to a step change in compressor and EXV input

R6 system evaporator matrix $\mathbf{A}_{e,R6}$ and condenser matrix $\mathbf{A}_{c,R6}$ with the respective balance equation vector $\mathbf{f}_{e,R6}$ and $\mathbf{f}_{c,R6}$ are given in the Appendix A2.

3.2.4. Static condenser two-phase node length (R5)

Since the phase-distribution within the condenser is not considered to be of primary concern in controller design, the length of two-phase node within the condenser, L_{c2}, can be replaced with a static expression The boundary conditions of now lumped-parameter condenser model can only be defined by assuming outlet conditions, therefore the assumption that the refrigerant is in saturated liquid state at the outlet is introduced, eliminating the need for the subcooling node L_{c3}. Two phase length L_{c2} is presumed to take up the remaining length of the condenser and is calculated by subtracting the superheating node length L_{c1} from the length of the condenser L_c.

This project has received funding from the European Union's Horizon 2020 research and innovation programme under grant agreement No. 769826. The content of this publication is the sole responsibility of the Consortium partners listed herein and does not necessarily represent the view of the European Commission or its services.

$$L_{c2} = \frac{\dot{m}_{ci} h_{cg} - \dot{m}_{co} h_{cl}}{\alpha_{ci2} A_{ci} (T_{cr2} - T_{cw})} \tag{19}$$

3.2.5. Further reduction steps

Zhang et al. [20] presented a second order lumped-parameter VCC model, with system pressures p_e and p_c as only state variables. The elimination of the wall temperature dynamics was based on the assumptions that in nominal operating conditions the wall temperature is almost equal to the temperature of the two-phase section. The thermal wall inertia was lumped into refrigerant thermal mass and the rate of wall temperature change was assumed to be equal to the time rate of change of saturation temperature at refrigerant pressure. This connects the wall dynamics indirectly to pressure dynamics. Temperature at the evaporator outlet T_{eo} is set to have constant superheat temperature difference ΔT_{SH} = 5 °C for all operating points making the 2nd -order model unsuitable for control design, since it lacks the control input for EXV.

Introducing the assumption of equal wall and refrigerant temperature from second-order model to R5 model would result in a 3rd -order model (R3). Thus, the R3 would describe heat exchanger pressure dynamics, p_e and p_c, and additional evaporator two-phase length dynamics, L_{e2}. In this way, the R3 model would keep the expansion valve opening input and superheat temperature output, which are eliminated in second-order model.

3.3. Model static mapping, linearization and identification

3.3.1. Static input-output maps

HVAC system static maps provide a useful tool for analysis of steady-state input-output relationships that can provide insight into HVAC system behaviour. These maps can also serve for the purpose of qualitative model validation in terms of checking if expected trends appear (e.g. evaporator outlet air temperature drop for increased compressor speed). Furthermore, state-variable static maps can facilitate model linearization in terms of providing input, output and state variable steady-state operating point, without need for use cumbersome trim routines. Finally, static maps can conveniently be used in cabin thermal comfort control trajectory optimisation and feedback controller design, where it is assumed that HVAC dynamics are faster than cabin air temperature dynamics (see Subsection 3.4.).

An automated numerical mapping procedure/tool has been developed based on repetitive running of simulation model. The procedure consists of initializing the model in a priori known steady-state condition and slowly ramping one of the inputs from the initial value to the end value at a prescribed rate. Once the end value is reached, all inputs are held constant for certain time to allow the system to reach steady state. The obtained steady-state output and input values (and state variables if needed) are stored in m-dimensional matrix where m is the number of varied inputs (e.g. a 3D matrix for the case of three inputs), while the number of outputs defines the number of produced maps. The procedure is repeated for all values of the first input, and then again for different combination of other inputs. Increase in number of inputs and/or input resolution results in prolonged procedure run-time, so that these parameters should be carefully set depending on target application. Additionally, final maps can be filtered with respect to certain input and/or output thresholds and additional criteria in order to obtain smaller maps. For example, the map in Figure 21a is obtained by imposing the desired superheat temperature (ΔT_{SHd} = 15 °C for $\dot{m}_{ea}$ = 0.02 kg/s and ΔT_{SHd} = 5 °C for $\dot{m}_{ea}$ = 0.075 kg/s and above), for each air mass flow rate input combination (to eliminate the expansion valve opening as an input) and minimum evaporator air outlet temperature ($T_{ea,out}$ = 273 K), and then extracting the subset of operating points from the final map whose superheat temperature is closest to the desired value and evaporator air outlet temperature is greater than the prescribed minimum. This procedure is applicable to white-, grey-, and black-box models.

This project has received funding from the European Union's Horizon 2020 research and innovation programme under grant agreement No. 769826. The content of this publication is the sole responsibility of the Consortium partners listed herein and does not necessarily represent the view of the European Commission or its services.

Figure 21 shows two map examples obtained in MATLAB/Simulink for the 12th order HVAC model presented in Subsection 3.1. Figure 21a shows evaporator outlet air temperature map as a function of three inputs (compressor speed, and two air mass flow rates) for a fixed ambient air temperature and the aforementioned superheat temperature. The map indicates that for a fixed evaporator air mass flow rate $\dot{m}_{ea}$, the evaporator outlet air temperature $T_{ea,out}$ drops with increased compressor speed ω_{com}, while for fixed ω_{com}, the air temperature $T_{ea,out}$ increases with increased $\dot{m}_{ea}$. This suggests that higher evaporator cooling power is needed to lower the air temperature at increased air mass flow rates. For the particular HVAC parameters, at highest evaporator air mass flow rate $\dot{m}_{ea}$ = 0.13 kg/s the air cannot be cooled lower than $T_{ea,out}$ = 15 °C for maximum condenser air mass flow rate. The condenser air mass flow rate $\dot{m}_{ca}$ has a low influence on the evaporator air outlet temperature ($T_{ea,out}$ slightly decreases by increasing $\dot{m}_{ca}$). Figure 21b shows the evaporator outlet air temperature and the superheat temperature as a function of compressor speed and expansion valve opening for fixed ambient air temperature and air mass flow rates. It indicates that in order to keep the superheat temperature in desired range while decreasing the evaporator air outlet temperature, the expansion valve opening should increase with compressor speed.

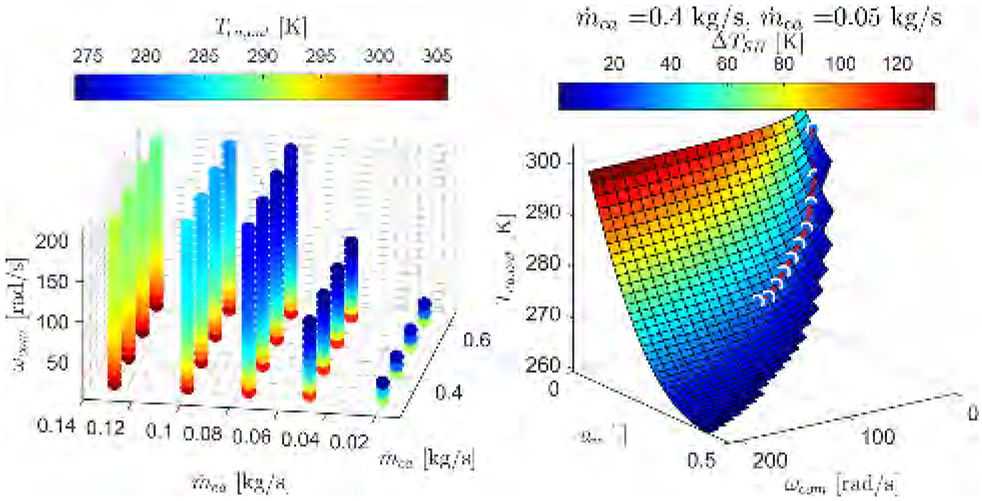

Figure 21: Filtered evaporator outlet air temperature map for fixed superheat temperatures (ΔT_{SHd} = 15 °C for $\dot{m}_{ea}$ = 0.02 kg/s and ΔT_{SHd} = 5 °C for $\dot{m}_{ea}$ = 0.075 kg/s and above) (a) and evaporator outlet air temperature and superheat temperature map for fixed air mass flow rates where the red line relates to the corresponding column in Fig. a (b).

3.3.2. Linearization

A numerical linearization tool has been developed within the MATLAB/Simulink environment. The tool takes a nonlinear model of the system, finds the operating points (using the function *findop*) for specified inputs and desired outputs, or loads the operating point stored in static maps, and linearizes the model around the trimmed operating point. This operation is indifferent to the model order and can be applied to black-box models (created or imported into Simulink), as well. Inputs that are not considered as control variables, such as those stored in memory blocks, are replaced by constant-value operating point-dependent inputs. Linearization results in a linear time-invariant state-space model suitable for further linear analysis and controller design. The obtained linearized models can serve in validation of reduced-order models based on step response or pole-zero map comparisons. Figure 22 shows the comparative step response of full-order R12 model and the reduced-order R6 model, both given in nonlinear and linearized variants. The difference in inital outlet evaporator air temperature $T_{ea,out}$ between R12 and R6 is due to different initial wall temperatures. Namely, the single wall temperature T_{ew} introduced in R9 (and kept in R6) slows down the overall dynamics of evaporator

This project has received funding from the European Union's Horizon 2020 research and innovation programme under grant agreement No. 769826. The content of this publication is the sole responsibility of the Consortium partners listed herein and does not necessarily represent the view of the European Commission or its services.

heat exchange due to lesser temperature gradient between the wall and individual nodes. This difference can be mitigated by adjusting the internal and external heat transfer coefficients.

The pressure dynamics for both evaporator and condenser are well preserved in the reduced-order model. Expectedely, the linearized models gives responses that are close to the original, nonlinear models for the considered small-signal operating mode (for which a linearized model is valid/obtained).

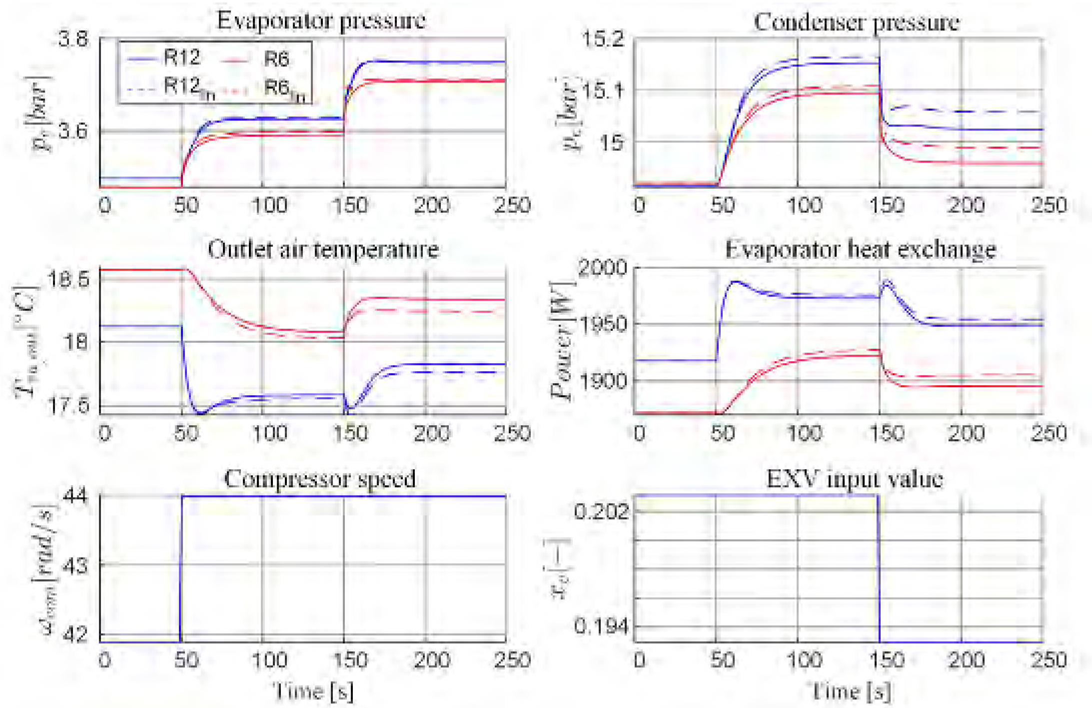

Figure 22: Response of nonlinear and linearized R12 model to a step change in compressor speed and EXV opening

3.3.3. Model identification

Low-order control-oriented linear models can alternatively be obtained by applying model identification methods, either based on high-order nonlinear models or real system experimental responses. Model identification bypasses the need for model-order reduction, and is easily applicable to black-box HVAC models of any structure, which makes it particularly interesting for HVAC control design purposes, particularly for cooperative projects (such as QUIET), where a partner develops the model and delivers it to another partner for designing controls.

A numerical tool for obtaining multi-input multi-output autoregressive exogenous (ARX)-type HVAC model has been developed in MATLAB. For the purposes of HVAC low-level control design, identification of a two-input/two-output discrete-time ARX model is considered, with the the model having following structure:

$$\begin{aligned}
&\mathbf{A}_{11}(z)y_1(k) = -\mathbf{A}_{12}(z)y_2(k) + \mathbf{B}_{11}(z)u_1(k-n_{k11}) + \mathbf{B}_{12}(z)u_2(k-n_{k12}) + \mathbf{e}_1(k) \\
&\mathbf{A}_{22}(z)y_2(k) = -\mathbf{A}_{21}(z)y_1(k) + \mathbf{B}_{11}(z)u_1(k-n_{k21}) + \mathbf{B}_{12}(z)u_2(k-n_{k22}) + \mathbf{e}_2(k) \\
&\mathbf{A}_{ij}(z) = 1 + a_{ij,1}z^{-1} + \ldots + a_{ij,n_{ij,a}}z^{-n_{ij,a}}, \qquad i=1,2, \qquad j=1,2 \\
&\mathbf{B}_{ij}(z) = b_{ij,1} + b_{ij,2}z^{-1} + \ldots + b_{ij,n_{ij,b}}z^{-n_{ij,b}+1}
\end{aligned} \tag{20}$$

This project has received funding from the European Union's Horizon 2020 research and innovation programme under grant agreement No. 769826. The content of this publication is the sole responsibility of the Consortium partners listed herein and does not necessarily represent the view of the European Commission or its services.

where $u_1 = \omega_{com}$, $u_2 = a_v$, $y_1 = T_{ea,out}$, $y_2 = \Delta T_{SH}$, $n_{ij,a}$ is the order of polynomial $\mathbf{A}_{ij}(z)$, $n_{ij,b}$ is the order of polynomial $\mathbf{B}_{ij}(z)+1$, and n_k is the input-output delay and z is the time-shift operator. The order of each polynomial is set separately in advance, and the sum of orders determines the number of coefficients to be determined by setting a linear regression problem and using a least-squares method. Model identification procedure is implemented in MATLAB by using System Identification Toolbox *arx* function. Multiple models with various polynomial orders can be identified in an automated way and assessed taking into account fitness and complexity in order to obtain optimal model structure.

ARX model identification is demonstrated for a single operating point of the 12th-order model, where the evaporator outlet air temperature and the superheat temperature are outputs and the compressor speed and the expansion valve opening are inputs. Simulation data set contains multiple step-responses around the initial operating point: $T_{ea,out}$ = 8 °C, ΔT_{SH} = 8 °C, ω_{com} = 80 rad/s, a_v = 0.3, $\dot{m}_{ca}$ = 0.5 kg/s and $\dot{m}_{ea}$ = 0.075 kg/s. The simulation data are sampled at 0.1 s. Two models are considered: ARX1 with all $\mathbf{A}_{ij}$ and $\mathbf{B}_{ij}$ polynomial orders set to three, and ARX2 with polynomial orders set to six, while input-output delay is set to zero in both cases. Figure 23 a-d show the data set used in model identification based on simulation of R12 model (black lines) and time responses of identified models. The higher-order model (blue line) results in lower normalized root-mean squared error (i.e. higher fitness index denoted in label) than the lower-order model (red line) and matches the transient response of simulated data to better extent, while both models satisfy steady-state accuracy**.** Figure 23 e-h show validation data set (black lines) and time responses of identified models. The results indicate that slight steady-state discrepancy occurs between linear ARX model time responses and simulation data for the case of increased magnitude of inputs, while the transient response is well matched.

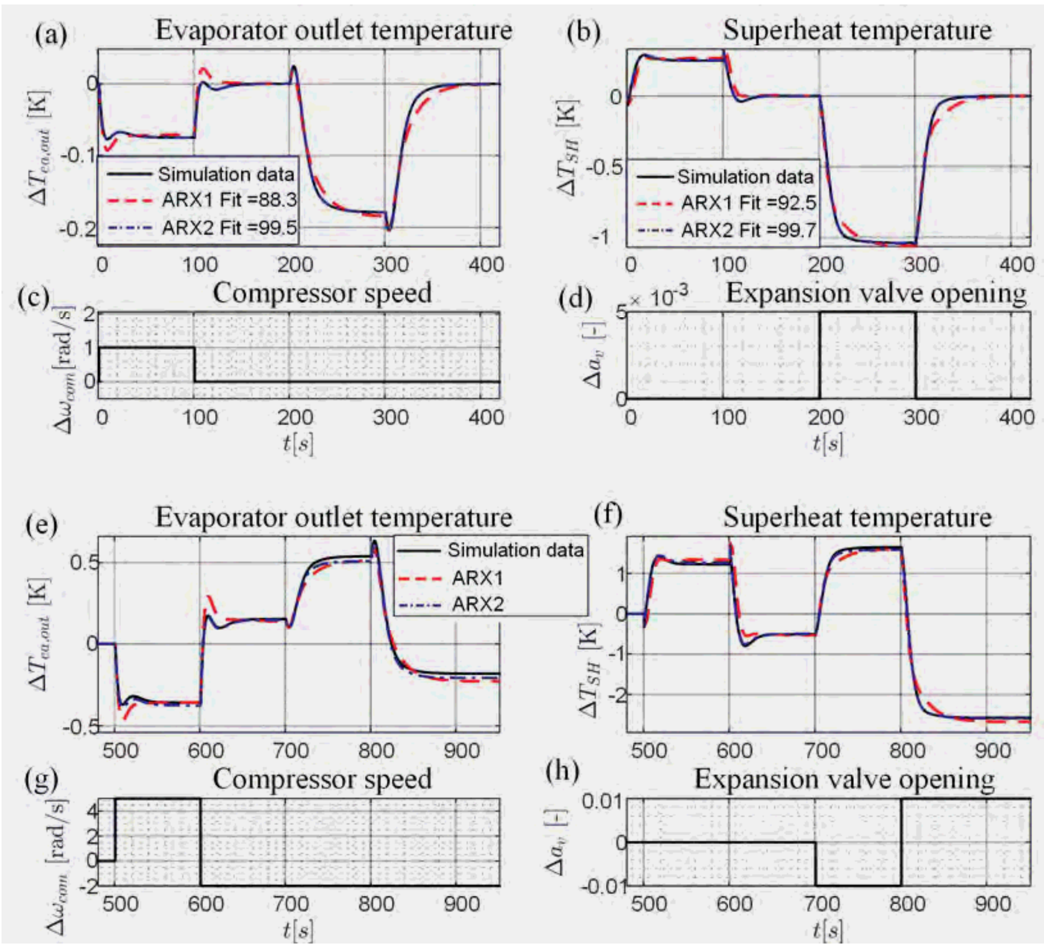

This project has received funding from the European Union's Horizon 2020 research and innovation programme under grant agreement No. 769826. The content of this publication is the sole responsibility of the Consortium partners listed herein and does not necessarily represent the view of the European Commission or its services.

Figure 23: Model identification input data (black lines) and time responses of ARX1 model with third-order polynomials (red line) and ARX2 model with sixth-order polynomials (blue line) for identification data set (a-d) and validation data set (e-h)

3.4. Control trajectory optimisation and optimised control strategy

The models and tools presented in the previous Subsections have been applied for control trajectory optimisation and control strategy development, as will be explained in the following Subsections.

3.4.1. HVAC and cabin modelling

The passenger cabin thermal system connected to the conventional HVAC system is depicted in Figure 24. A detailed lumped-parameter control-oriented model of the HVAC system includes 12 state variables related to evaporator ($\mathbf{x}_e$) and condenser ($\mathbf{x}_c$) dynamics as it is presented in subsection 3.1. Electric motor-powered compressor, electronic expansion valve, blower fan and condenser fan are considered as typical EV HVAC actuators. Therefore, control inputs fed to the HVAC model are compressor speed ω_{com}, electronic expansion valve opening a_v, blower fan air mass flow rate $\dot{m}_{ea}$ and condenser fan air mass flow rate $\dot{m}_{ca}$. Outputs of the HVAC model, which are of particular interest in this paper, include evaporator outlet air temperature $T_{ea,out}$ (i.e. cabin inlet air temperature), superheat temperature ΔT_{SH}, and coefficient of performance defined as the ratio of evaporator air-side cooling power and compressor power consumption $COP = \dot{Q}_{ea}/P_{com}$. The power consumption of expansion valve and blower fan is not considered in COP calculation.

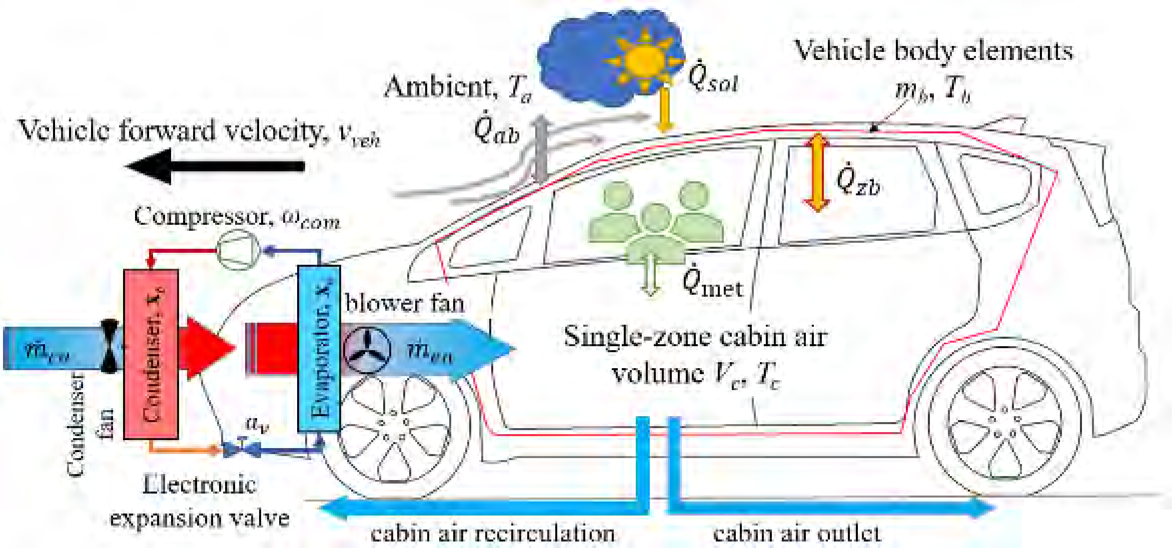

Figure 24: HVAC and cabin model schematic

The considered passenger cabin model [21] consists of two thermal masses: (i) cabin air volume V_c with temperature T_c and (ii) body elements of mass m_b with temperature T_b. The modelled thermal loads include constant metabolic load $\dot{Q}_{met}$ if the cabin air temperature is below 36 °C, solar radiation load $\dot{Q}_{sol}$, ambient air convection heat transfer $\dot{Q}_{ab}$ over outer body surface A_{ab} with variable heat transfer coefficient $\alpha_{ab}(v_{veh})$, HVAC thermal load $\dot{Q}_{HVAC}$ that takes into account cabin air inlet and outlet, and convection heat transfer from body elements to cabin air $\dot{Q}_{cb}$ over inner body surface A_{cb} with heat transfer coefficient α_{cb}. The second-order cabin model obtained by heat balance method [23] then reads:

This project has received funding from the European Union's Horizon 2020 research and innovation programme under grant agreement No. 769826. The content of this publication is the sole responsibility of the Consortium partners listed herein and does not necessarily represent the view of the European Commission or its services.

$$\begin{aligned} c_{pac}\rho_c V_c \dot{T}_c &= \underbrace{\dot{m}_{ea} c_{pae}\left(T_{ea,out}\left(\omega_{com}\right)-T_c\right)}_{\dot{Q}_{HVAC}}+\dot{Q}_{met}\left(T_c\right)+\underbrace{\alpha_{cb} A_{cb}\left(T_b-T_c\right)}_{\dot{Q}_{cb}} \\ c_{pb} m_b \dot{T}_b &= -\underbrace{\alpha_{cb} A_{cb}\left(T_b-T_c\right)}_{\dot{Q}_{cb}}+\dot{Q}_{sol}+\underbrace{\alpha_{ab}\left(v_{veh}\right) A_{ab}\left(T_b-T_a\right)}_{\dot{Q}_{ab}} \end{aligned} \tag{21}$$

where c_{pa} is the air specific heat capacity, ρ_c is the air density and c_{pb} is the body specific heat capacity. The second-order cabin model (23) can further be simplified to first order model by assuming that the body temperature dynamic is slower than the cabin air temperature dynamic, which gives:

$$\begin{aligned} k_c c_{pa}\rho_c V_c \dot{T}_c &= \underbrace{\dot{m}_{ea} c_{pae}\left(T_{ea,out}\left(\omega_{com}\right)-T_c\right)}_{\dot{Q}_{HVAC}}+\dot{Q}_{met}(T_c)+\dot{Q}_{sol}+\underbrace{\alpha_{ab}\left(v_x\right) A_{ab}\left(T_a-T_b\right)}_{\dot{Q}_{ab}} \\ T_b &= T_c+\Delta T_b \le T_{b,\max} \end{aligned} \tag{22}$$

where k_c scales the cabin air temperature thermal inertia to match the second order model dynamics and ΔT_b is the air-to-body temperature offset used for "tuning" the steady state accuracy. Since cabin models consider complete cabin volume, it is assumed that the mean air velocity v_{air} inside the cabin is proportional to the blower fan air mass flow rate $\dot{m}_{ea}$:

$$v_{air} = k_{mve}\dot{m}_{ea} \tag{23}$$

where k_{mve} is proportionality constant e.g. expressed as the ratio of air density and cabin inlet vents cross-section area. Similarly, a linear relationship between the vehicle speed v_{veh} and the condenser fan air mass flow rate $\dot{m}_{ca}$ is assumed:

$$\dot{m}_{ca} = \dot{m}_{ca0} + k_{mvc}v_{veh} \tag{24}$$

where $\dot{m}_{ca0}$ is air mass flow rate for stationary vehicle and k_{mvc} is constant coefficient. The closed-loop dynamics of evaporator outlet air temperature control system of the particular HVAC model is by an order of magnitude faster than the cabin air temperature dynamics. In order to enhance computational efficiency of DP-based control variable optimisation, the HVAC is represented by static maps which describe steady-state input to output relationships. The static maps shown in Figure 25 have been obtained by the numerical method/tool described in subsection 3.3. for the superheat temperature being fixed to its target value of 5 $^{\circ}$C (it is assumed that the superheat temperature is effectively controlled by the expansion valve) and the 12th-order model presented therein.

This project has received funding from the European Union's Horizon 2020 research and innovation programme under grant agreement No. 769826. The content of this publication is the sole responsibility of the Consortium partners listed herein and does not necessarily represent the view of the European Commission or its services.

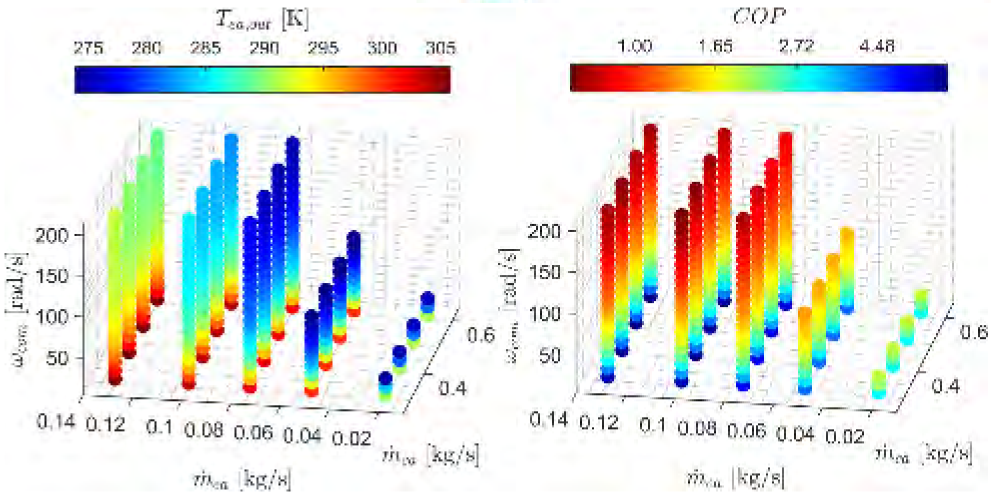

Figure 25: HVAC model static maps related to evaporator outlet air temperature (a) and efficiency defined by COP (b)

3.4.2. Thermal comfort criterion

The cabin thermal comfort is evaluated through Predicted Mean Vote (*PMV*), which is adjusted to take into account the cooling effect of increased air velocity [22]. A positive *PMV* means that the cabin environment is too hot, while a negative *PMV* indicates that it is too cold. The zero *PMV* suggests ideal thermal comfort, while the comfortable range is defined as $|PMV| < 0.5$ [24]. *PMV* takes into account six different parameters: air temperature T_{air}, air velocity v_{air}, mean radiant temperature, air relative humidity *RH*, clothing, and metabolic rate. In order to simplify the *PMV* calculation, it is assumed that the driver is wearing summer clothes and that the mean radiant temperature is equal to the mean air temperature inside the cabin. The *PMV* map shown in Figure 26a is obtained for the relative humidity $RH \in [0, 1]$, air temperature $T_{air} \in [16, 40]$ °C, air velocity $v_{air} \in [0.17, 1.1]$ m/s, clothing thermal resistance of 0.5 clo, and metabolic rate of 1.5 (typical value for driving) [24]. Black circles indicate comfort range, i.e. $|PMV| < 0.5$. An example of *PMV* map for the constant relative humidity of 44% is shown in Figure 26b, where the black solid lines denote the boundaries of comfort range ($|PMV| < 0.5$), shows that the same thermal comfort can be achieved with higher cabin air temperature if the air velocity is increased (and also if the humidity is reduced, Figure 26a)

This project has received funding from the European Union's Horizon 2020 research and innovation programme under grant agreement No. 769826. The content of this publication is the sole responsibility of the Consortium partners listed herein and does not necessarily represent the view of the European Commission or its services.

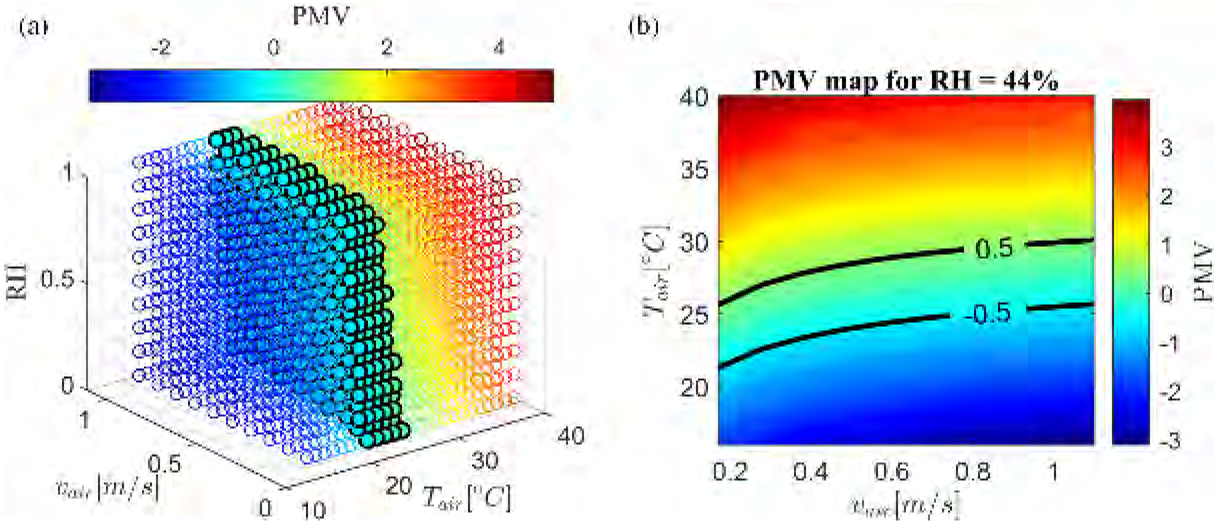

Figure 26: Predicted mean vote (*PMV*) map with three inputs where filled circles show comfort range (|*PMV*| < 0.5) (a) and *PMV* map with two inputs and fixed relative humidity (*RH* = 44%) where black lines denoting comfort range (b)

3.4.3. Control variable optimisation

The presented control variable optimisation approach is based on the dynamic programming (DP) optimisation algorithm [23]. DP optimisation results in globally optimal solution as it starts with final time t_f and calculates optimal control inputs for all possible state variables (satisfying the process model) backwards in time at each time instant. However, DP is computationally very expensive and the computational cost exponentially grows with the number of state variables and control inputs. Therefore, discrete-time counterpart of the first order cabin air temperature model defined by Eq. (22) is used in DP optimisation to describe single state-variable (x) dynamics:

$$x = T_c,$$

with two control inputs contained in control vector $\mathbf{u}$:

$$\mathbf{u} = [\omega_{com} \quad \dot{m}_{ea}],$$

while the condenser fan air mass flow rate $\dot{m}_{ca}$ represents disturbance variable (potentially, it could be included in optimisation as an additional control variable). The HVAC evaporator outlet air temperature $T_{ea,out} = T_{ea,out}(\omega_{com}, \dot{m}_{ea}, \dot{m}_{ca})$ and efficiency $COP = COP(\omega_{com}, \dot{m}_{ea}, \dot{m}_{ca})$ are described by the static maps depicted in Figure 25, where a trilinear interpolation is applied for input combinations that are not defined by the map). The expansion valve opening a_v is not contained in control vector $\mathbf{u}$ since the HVAC static maps have been obtained for constant/target superheat temperature value. The thermal comfort criterion *PMV* is obtained by map shown in Figure 26a, where the trilinear interpolation is again applied for the case of missing input combinations.

The control variable optimisation problem is to find the control vector $\mathbf{u}(k)$, which minimises the cost function J:

$$J = \Phi\left(x\left(t_f\right)\right) + \sum_{k=1}^{N} F\left(x(k), \mathbf{u}(k)\right) \tag{25}$$

at each discrete-time instant k, where the terminal condition function:

$$\Phi\left(x\left(t_f\right)\right) = K_{penf}\left(x_{tf,R} - x\left(t_f\right)\right)^2 \tag{26}$$

This project has received funding from the European Union's Horizon 2020 research and innovation programme under grant agreement No. 769826. The content of this publication is the sole responsibility of the Consortium partners listed herein and does not necessarily represent the view of the European Commission or its services.

ensures that the cabin air temperature reference $x_{tf,R} = T_{c,R}$ is achieved at the end of optimisation time horizon, by applying sufficiently high penalisation coefficient K_{penf}. The sub-integral function $F(\cdot)$ includes minimisation of thermal comfort criterion (*PMV*) and maximisation of efficiency (*COP*), alongside with penalisation of state-variable and control inputs constraint violations:

$$
\begin{aligned}
&F\left(x(k),\mathbf{u}(k)\right) = K_{PMV}\left|PMV(\mathrm{k})\right| + K_{COP}COP(k)^{-1} + \\
&K_{pen}\left[H\left(x(k)-x_{\max}\right)+H\left(x_{\min}-x(k)\right)\right]+K_{pen}\left[H\left(\mathbf{u}(k)-\mathbf{u}_{\max}\right)+H\left(\mathbf{u}_{\min}-\mathbf{u}(k)\right)\right]
\end{aligned}
\quad (27)
$$

where K_{PMV} and K_{COP} are weighting coefficients that set the trade-off between thermal comfort and efficiency, K_{pen} is constraint violation penalisation coefficient that should be sufficiently high, and $H(a)$ is Heaviside function defined as $H(a) = 0$ for $a < 0$ and $H(a) = 1$ for $a \geq 1$. Constraints are used to contain the state-variable in the target range and use control inputs that are within specified hardware-related limits. Note that alternatively the power consumption of the HVAC system can be used instead of COP in the cost function (27).

3.4.4. Low-level control system

The evaporator outlet air temperature (i.e. the cabin inlet air temperature) $T_{ea,out}$ is controlled in a feedback loop to provide accurate and high-bandwidth tracking of the reference set by the high-level control system. The superheat temperature ΔT_{SH} is regulated with respect to fixed reference $\Delta T_{SH,R} = 5$ °C (a safety function), where the main aim of the corresponding feedback controller is to suppress disturbance influence including the one imposed by the action of outlet temperature controller. The linearized input-output HVAC model depicted in Figure 27a is characterised by coupled dynamics, which can be described by four transfer functions linking the control inputs (compressor speed ω_{com} and expansion valve opening a_v) and controlled outputs (evaporator outlet air temperature $T_{ea,out}$ and superheat temperature ΔT_{SH}):

$$
G_{11}(s)=\frac{T_{ea,out}(s)}{\omega_{com}(s)}, \qquad G_{12}(s)=\frac{T_{ea,out}(s)}{a_v(s)}, \qquad G_{21}(s)=\frac{\Delta T_{SH}(s)}{\omega_{com}(s)}, \qquad G_{12}(s)=\frac{\Delta T_{SH}(s)}{a_v(s)}. \quad (28)
$$

Reasonably good control performance of superheat temperature regulation and evaporator setpoint tracking can be obtained for the given HVAC model by applying a simplified, decoupled control structure where only two main controllers $G_{c11}(s)$ and $G_{c22}(s)$ are used (Figure 27a; there are no cross-coupling control actions). The controllers are of proportional-integral (PI) type, and their parameters are tuned by using a search-algorithm optimisation procedure targeted to single-input single-output (SISO) system [24] implemented in MATLAB. The cost function to be minimised combines penalisation of closed-loop control error and control effort. Referring to control structure shown in Figure 27a, the cost functions for the two control loops are defined as:

$$
\begin{aligned}
\min J_{11} &= \frac{1}{1+M}\sum_{k=0}^{M}\left[f_{we11}(k)\left(T_{ea,out,R}-T_{ea,out}(k)\right)^2 + r_{11}\left(\omega_{com,R}-\omega_{com}(k)\right)^2\right] \\
\min J_{22} &= \frac{1}{1+M}\sum_{k=0}^{M}\left[f_{we22}(k)\left(\Delta T_{SH,R}-T_{SH}(k)\right)^2 + r_{22}\left(a_{v,R}-a_v(k)\right)^2\right]
\end{aligned}
\quad (29)
$$

where r_{11} and r_{22} are weighting coefficients which set the trade-off between control error suppression (performance) and control effort reduction (efficiency, relative stability). The weighting functions f_w and f_{ew} are Heaviside functions defined as $f_w(k) = 0$ for $k < W$ and $f_w(k) = 1$ for $k \geq W$, where W is the length of window $[0,W]$ within which the (inevitable) control error is disregarded in optimization, in order to avoid the optimizer's tendency to produce strong control effort and response oscillation in its attempt to reduce the initial control error. To optimize over complete response window, W is set to 0 (which is the case in this subsection). Since the HVAC dynamics model parameters depend on the operating point, gain scheduling maps (two proportional gain maps K_{p11} and K_{p22}, and two integral gain maps K_{i11} and K_{i22}) have been obtained by repeating the PI controller parameter optimisation procedure for multiple operating points with fixed weighting

This project has received funding from the European Union's Horizon 2020 research and innovation programme under grant agreement No. 769826. The content of this publication is the sole responsibility of the Consortium partners listed herein and does not necessarily represent the view of the European Commission or its services.

coefficients r_{11} and r_{22}. The analysis showed that the most significant operating point parameters were the evaporator outlet air temperature $T_{ea,out}$ and the blower fan air mass flow rate $\dot{m}_{ea}$, which results in two-dimensional gain scheduling maps $K_x = f_x(T_{ea,out}, \dot{m}_{ea})$. Final low-level control system structure is shown in Figure 27b and consists of two PI controllers with two pairs of gain-scheduling maps.

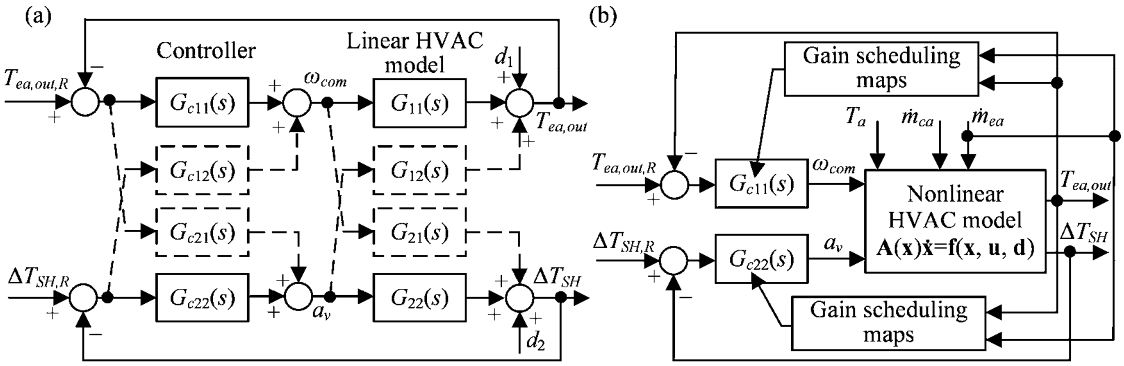

Figure 27: Block diagram of linearized HVAC system and controllers (solid lines) used in controller parameter optimisation (where d denotes disturbance, e.g. varying air mass flow rate) (a), and block diagram of final low-level control system (b); Note: PI controller transfer function is $G_c(s) = K_p(1 + 1/(T_i s))$

The low-level control system performance is illustrated in Figure 28 for the full, 12-th order nonlinear process model, where blue lines denote the performance of control system with fixed controller gains (tuned for $T_{ea,out}$ = 15 °C and $\dot{m}_{ea}$ = 0.05 kg/s), while green lines correspond to the control system with gain-scheduling applied. The evaporator air mass flow rate $\dot{m}_{ea}$ is kept at 0.075 kg/s, the superheat temperature reference is set to $\Delta T_{SH,R}$ = 5 °C and the step reference with magnitude of $\Delta T_{ea,out,R}$ = 5 °C is applied at t = 1000 s (red dashed lines in Figure 28a and b). In comparison with the control system that uses fixed controller gains, the control system with gain scheduling achieves faster evaporator outlet air temperature response (Figure 28a), and lower superheat temperature control error (Figure 28b). The performance improvement is achieved by stronger compressor and expansion valve control efforts (Figure 28c and d). Figure 28e and f show that optimal controller gains vary significantly throughout the operating range, thus making the gain scheduling algorithm necessary to achieve optimal performance over a wide operating range.

It has been found that the closed-loop system performance can be further improved by taking into account the coupled dynamics of HVAC model, which is determined in Figure 27a by the cross-coupling transfer functions $G_{12}(s)$ and $G_{21}(s)$. In this case, the parameters of both PI controller were optimized simultaneously, with an option to include the cross-coupling gains as well (see $G_{c12}(s)$ and $G_{c21}(s)$ in Figure 27a). A multi-objective genetic algorithm was used as optimisation algorithm, because it allows for overcoming the issue of local optima appearance and can present the results in the form of Pareto frontier that enable the designer to select optimal solution based on his/her preference. However, such procedure is more time consuming, especially when gain-scheduling is concerned.

This project has received funding from the European Union's Horizon 2020 research and innovation programme under grant agreement No. 769826. The content of this publication is the sole responsibility of the Consortium partners listed herein and does not necessarily represent the view of the European Commission or its services.

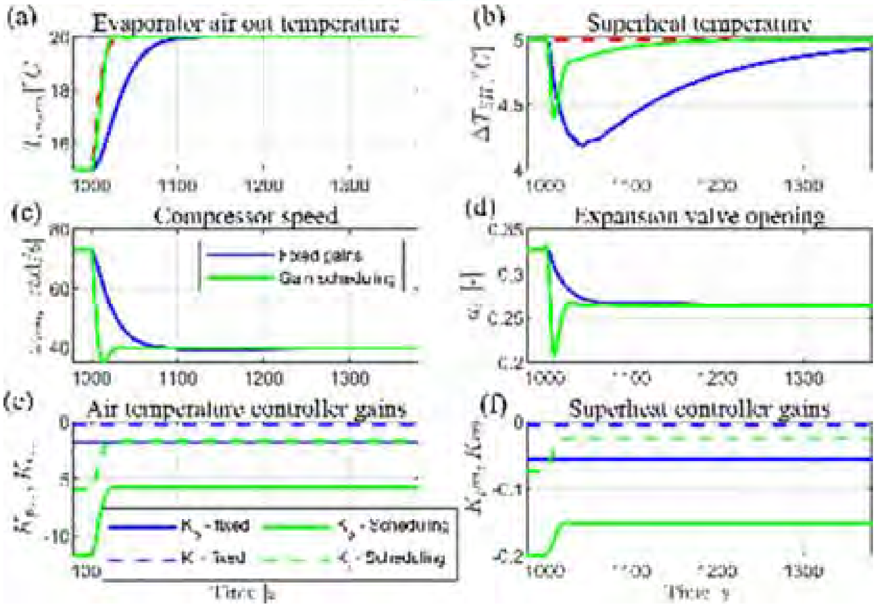

Figure 28: Comparison of low-level controller performance with and without using gain scheduling maps.

3.4.5. High-level control system

In order to achieve favourable thermal comfort inside the vehicle cabin while maintaining best possible efficiency of the HVAC system, a supervisory high-level control system has been developed. According to the block diagram shown in Figure 29, the high-level control system regulates the cabin air temperature T_c by commanding the cooling capacity $\dot{Q}_d$. The cooling capacity $\dot{Q}_d$ is then transformed within a control allocation map to low-level controller inputs/references, which in this case include the evaporator outlet air temperature reference $T_{ea,out,R}$ and the air mass flow $\dot{m}_{ea,R}$ (while in a more general case more inputs are possible, such as the condenser air mass flow $\dot{m}_{ca,R}$ in Figure 29). Note that evaporator outlet air temperature reference and air mass flow are mutually constrained through cooling capacity demand (see Eq. 28). Using the cabin air temperature T_c and the cooling (heating) capacity demand $\dot{Q}_d$ as inputs to the control allocation map allows for omitting the cabin dynamics model from control allocation map design. This facilitates allocation map generation, and more importantly, makes the allocation map independent of cabin model.

To achieve optimal system performance, it is crucial to base the design of control allocation map on optimisation (Johansen 2012). For the specific HVAC system and design case, control allocation is based, herein, on instantaneous, on-line optimisation. A linear search-based method is applied using the minimum blower fan air mass flow setpoint and corresponding evaporator outlet air temperature as initial guesses. On-line optimisation relies on *PMV* and *COP* maps, both of which are prepared off-line as functions of two inputs. However, in more general case when using multiple control inputs, the dimension of *COP* map grows with the number of control inputs, which can lead to poor computational efficiency when using a linear search or may result in local optima when a more advanced, directional search approach is applied. To overcome these weaknesses, an alternative, off-line optimisation approach (e.g. multi-objective genetic algorithm optimization) can be applied, as suggested in [26] and presented in Subsection 3.5 for the target, more complex EV HVAC system. That approach would result in control input maps as functions of cabin temperature and cooling capacity demand (Figure 29), which could be fitted by analytical models/functions, to facilitate the control strategy implementation and calibration. At the superimposed level, a discrete-time fixed-gain PI-type cabin air temperature controller $G_{c,CAB}(z)$ is used (with an option to add a gain scheduling algorithm in more general case; Fig. 6). Since the cabin air temperature dynamics are slow, the cabin air temperature controller and control allocation strategy can have higher sampling time than the low-level controllers (10 s vs. 0.1 s).

This project has received funding from the European Union's Horizon 2020 research and innovation programme under grant agreement No. 769826. The content of this publication is the sole responsibility of the Consortium partners listed herein and does not necessarily represent the view of the European Commission or its services.

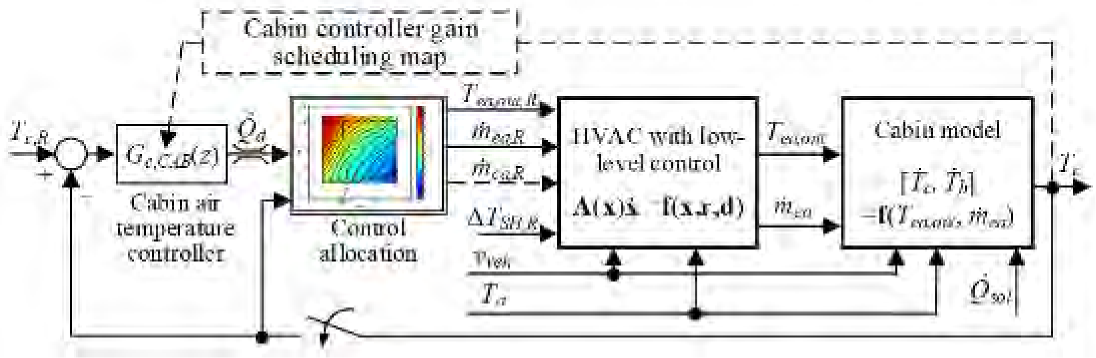

Figure 29: Cabin air temperature control block diagram

The optimal control allocation map is obtained by minimising the following cost function for a wide range of operating points ($\dot{Q}_d$, T_c):

$$J_{ca} = K_{PMV} \left| PMV\left(\dot{m}_{ea,R}, T_c\right) \right| + K_{COP} \frac{1}{COP\left(\dot{m}_{ea,R}, T_{ea,out,R}\right)} \tag{30}$$

where K_{PMV} and K_{COP} are weighting coefficients that set the trade-off between the two conflicting criteria: thermal comfort (*PMV*) and efficiency (*COP*). Control variables are subject to following constraints:

$$\begin{gathered} \dot{Q}_d = \dot{m}_{ea,R} c_{pa} \left(T_{ea,out,R} - T_c\right) \\ \dot{m}_{ea,R,\min} \le \dot{m}_{ea,R} \le \dot{m}_{ea,R,\max} \\ T_{ea,out,R,\min}\left(\dot{m}_{ea,R}\right) \le T_{ea,out,R} \le T_{ea,out,R,\max}\left(\dot{m}_{ea,R}\right) \end{gathered} \tag{31}$$

where c_{pa} is the specific heat capacity of air, $\dot{m}_{ea,R,\max}$ and $\dot{m}_{ea,R,\min}$ are maximum and minimum air mass flow rates, and $T_{ea,out,R,\max}$ and $T_{ea,out,R,\min}$ are maximum and minimum evaporator outlet air temperatures that can be attained at certain air mass flow rate.

3.4.6. Results for cool-down scenario

Control variable optimisation (and, similarly, control system simulation analysis) have been carried out for cool-down scenario at constant vehicle velocity v_{veh} = 40 km/h. The objective of the cool-down scenario is to bring the cabin air temperature down from its initial value that is equal to ambient air temperature $T_{c0} = T_a$ = 40 °C to the final cabin air temperature of $T_{c,R}$ = 26 °C in 10 minutes, i.e. t_f = 600 s, similiarly to experimental tests in carried out on the FIT EV systems in [25].

3.4.6.1. Control variable optimisation results

Dynamic programming has been carried out with the time step Δt = 1 s (number of time samples N_t = 601). The state variable (cabin air temperature) has been discretized with the resolution of 0.5 °C in the range from 20 °C to 40 °C, the evaporator air mass flow rate discretization step is 0.01 kg/s between 0.02 kg/s and 0.13 kg/s, and the compressor speed discretization step is 5 rad/s between 10 rad/s and 210 rad/s.

Three different optimisation cases that have been considered are: (i) thermal comfort-oriented *PMV* minimisation (K_{PMV} = 1 and K_{COP} = 0 are set in the cost function (27)), (ii) HVAC efficiency-oriented *COP* maximisation (K_{PMV} = 0 and K_{COP} = 1), and (iii) combined case of simultaneous *PMV* minimisation and *COP* maximisation (K_{PMV} = 0.5 and K_{COP} = 1). The results shown in Figure 30 indicate that for the HVAC efficiency-oriented case (red line), the optimal control maintains a modest cooling capacity. This is reflected in a relatively slow fall of cabin air temperature (dashed red line in Figure 30a), relatively high evaporator outlet air temperature $T_{ea,out}$ (solid red line in Figure 30a), and correspondingly high evaporator air mass flow $\dot{m}_{ea}$ (Figure 30c). Such control is beneficial for HVAC efficiency (Figure 30f) as it enables the compressor to operate at a

This project has received funding from the European Union's Horizon 2020 research and innovation programme under grant agreement No. 769826. The content of this publication is the sole responsibility of the Consortium partners listed herein and does not necessarily represent the view of the European Commission or its services.

low speed (Figure 30d), thus having a minimal power consumption and maximising the *COP*. Note that the optimal behaviour for this case will change to some extent if the blower fan power consumption is accounted for in *COP*, as the power consumption typically increases with air mass flow.

For the case of *PMV* minimisation (blue line), the optimal control behaviour is to increase the compressor speed and air mass flow (Figure 30d and c) at the beginning of response, in order to lower the cabin inlet air temperature (Figure 30a) and achieve high cooling capacity, thus bringing the thermal comfort criterion *PMV* (Figure 30e) to zero as fast as possible. This results in the lowest *COP* (Figure 30f) until the thermal comfort has been achieved (*PMV* =0, $t \sim 200$ s), while the *COP* increases afterwards as lower compressor speed and lower air mass flow are sufficient to maintain the *PMV* around zero.

In the combined cost function case (green line), optimal control expectedly results in compromise between the previous two extreme cases related to efficiency and thermal comfort maximisation.

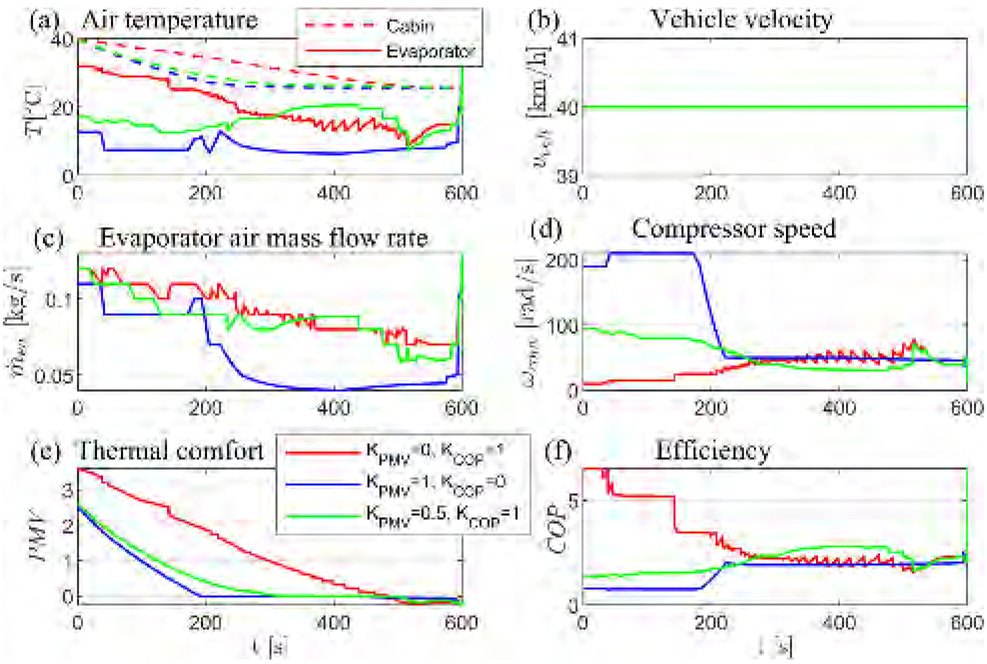

Figure 30: Control variable optimisation results for three optimisation cases: PMV minimisation only (blue), COP maximisation only (red) and combined PMV minimisation and COP maximisation (green)

3.4.6.2. Control strategy results

Control strategy simulation results shown in Figure 31 have been obtained for three characteristic cases of tuning the cost function (30) used in control allocation optimisation: *PMV* minimisation ($K_{PMV} = 1$ and $K_{COP} = 0$), (ii) *COP* maximisation ($K_{PMV} = 0$ and $K_{COP} = 1$), and (iii) combined case of simultaneous *PMV* minimisation and *COP* maximisation ($K_{PMV} = 0.5$ and $K_{COP} = 1$) with fixed cabin temperature PI controller gains $K_p = 125$, $K_i = 0.01$.

The cabin air temperature response shown in Figure 31a (dashed lines) is very similar for all three cases due to the same PI controller used. However, the allocated control inputs, i.e. the evaporator outlet air temperature (Figure 31a, solid lines) and the evaporator air mass flow (Figure 31f), are dependent on weighting coefficients K_{PMV} and K_{COP}. For the case of *COP* maximisation (red line), the compressor speed (Figure 31c) is kept low, which results in highest efficiency (Figure 31e, dashed lines), similarly to DP results shown in Figure 30. However, the evaporator air mass flow (Figure 31f) is kept low here, in order to lower the cabin air inlet temperature (Figure 31a, solid lines) to meet the high cooling capacity demand set by superimposed controller.

This project has received funding from the European Union's Horizon 2020 research and innovation programme under grant agreement No. 769826. The content of this publication is the sole responsibility of the Consortium partners listed herein and does not necessarily represent the view of the European Commission or its services.

For the case of *PMV* minimisation (blue line) the thermal comfort (Figure 31e, solid lines) is achieved at the fastest rate but this results in the lowest efficiency. The results of combined cost function case (green lines) fall between previous two extreme cases. Figure 31b and d show that the performance of superheat temperature control is satisfactory, and it could be further improved by applying more complex cross-coupling control.

Comparison of DP responses in Figure 30 and the control system simulation results in Figure 31 indicate qualitative differences between the two solutions. This is especially pronounced in the *COP* maximisation case, in which the DP keeps the cooling capacity low to slowly bring the cabin air temperature to target value, whereas the superimposed controller commands relatively high cooling capacity (cf. red lines in Figure 30 and 32) and brings the cabin temperature to the target value faster. This is explained by the fixed parameters of superimposed cabin temperature controller, i.e. same cabin temperature (and cooling capacity demand) response for all allocation weighting coefficient settings. In order to bring the control system performance closer to DP results, the superimposed cabin air temperature controller bandwidth should be tuned in correlation with allocation cost function settings, i.e. the superimposed cabin temperature controller should be made slower for the *COP* maximisation case.

Figure 32 shows the control system responses for three different cabin temperature controller integral gains: K_i = 0.005 (red line), K_i = 0.01 (green line) and K_i = 0.02 (blue line) and the combined-criteria cost function (K_{PMV} = 0.5, K_{COP} = 1). The cabin air temperature response (Figure 32a, dashed lines) is faster for higher integral gain K_i, because the cooling capacity demand effort is higher in that case (Figure 32b). This results in faster thermal comfort achievement but deteriorates efficiency (Figure 32c). The increased cooling capacity demand (higher K_i) is optimally satisfied with lower evaporator outlet air mass flow (Figure 32e), which enables lower evaporator air outlet temperature (Figure 32a, solid lines). For the case of slower cabin air temperature tuning (lower K_i), lower cooling capacity demand is met by high evaporator air outlet temperature and high blower fan air mass flow, which results in higher *COP*. Performance of moderate/nominal controller tuning (green line) falls between previous two tunings. The overall control system behaviour is closer to the DP results (cf. Figure 32 and Figure 30) than the previously considered case given in Figure 31. Figure 32d shows distribution of operating points over the *COP* map, from which it follows that the slowest PI controller tuning results in highest efficiency as the operating points in that case are grouped further to the left (higher *COP*).

This project has received funding from the European Union's Horizon 2020 research and innovation programme under grant agreement No. 769826. The content of this publication is the sole responsibility of the Consortium partners listed herein and does not necessarily represent the view of the European Commission or its services.

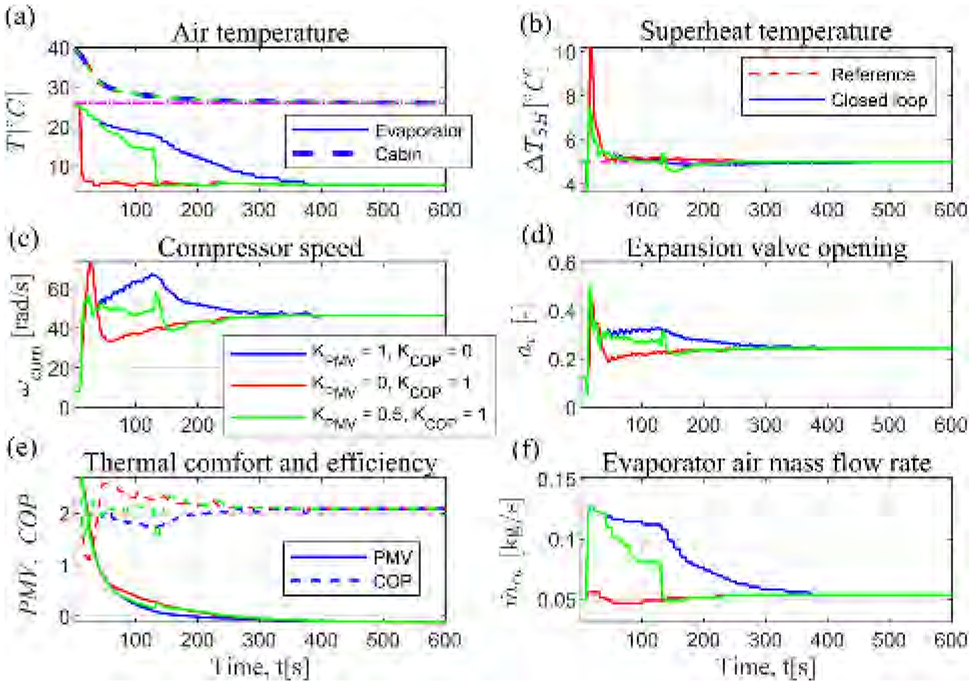

Figure 31: Control strategy simulation results for the case of PMV minimisation (blue line), COP maximisation (red line) and combined cost function case (green line); the superimposed cabin temperature controller has the fixed parameters

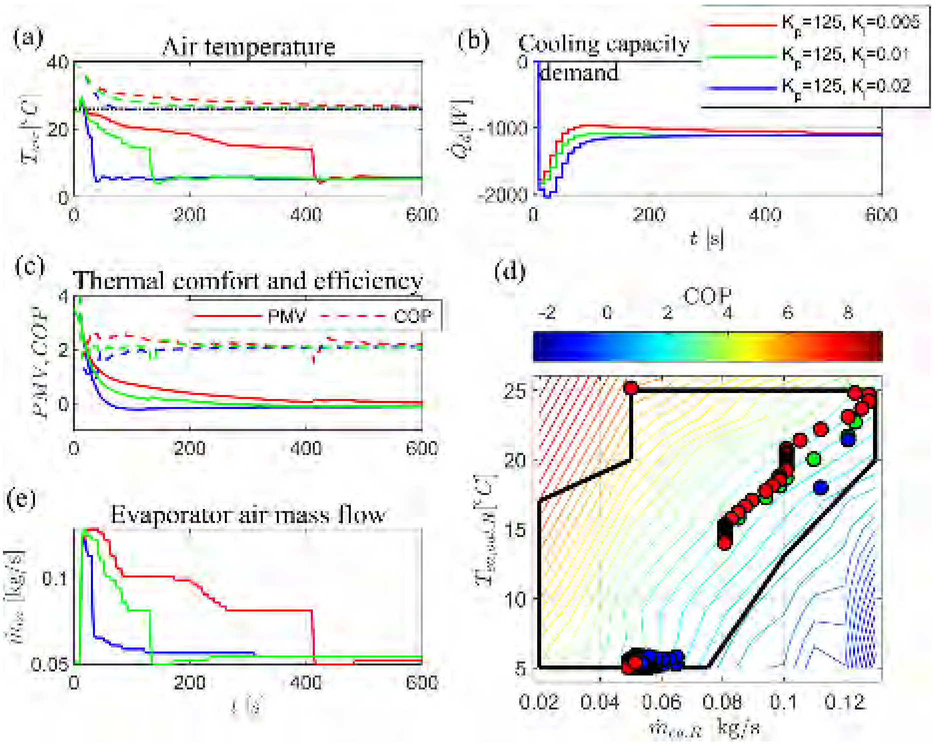

Figure 32: Control strategy simulation results for the case of three different PI controller tunings: Ki = 0.005 (red line), Ki = 0.01 (green line) and Ki = 0.02 (blue line), while the PMV vs. COP trade-off is fixed (to combined penalization)

Table 5 contains performance indices related to simulation results of cool-down scenario for various combinations of control allocation weighting coefficients and cabin air temperature controller tunings. The

This project has received funding from the European Union's Horizon 2020 research and innovation programme under grant agreement No. 769826. The content of this publication is the sole responsibility of the Consortium partners listed herein and does not necessarily represent the view of the European Commission or its services.

considered indices include total energy consumption $E_{com} = \int P_{com} dt$ (recall that the compressor is only consumer in the considered model) during the cool-down scenario and two thermal comfort criteria. The first thermal comfort criterion is cumulative absolute value of *PMV*, i.e. $C_1 = \int |PMV| dt$, and the second one is cumulative absolute value of *PMV* when the *PMV* is greater than a constant thermal comfort threshold (set to 0.22, herein), i.e. $C_2 = \int |PMV| dt$ if $|PMV| > 0.22$. Since the criterion C_2 prohibits integration when *PMV* is close to ideal value of zero, it is more suitable for transient evaluation as it allows the *PMV* to slightly deviate from ideal value in steady-state.

The best overall performance in terms of efficiency is achieved with slow cabin air temperature controller tuning and efficiency-oriented allocation cost. In this case the energy consumption is reduced by 25% compared to chosen nominal setting (blue line in Table 5). However, the best-efficiency setting results in the worst thermal comfort (C_1 is 81% higher and C_2 is 130% higher compared to the nominal setting). Keeping the slow cabin air temperature controller tuning and increasing the allocation cost towards the comfort-oriented case reduces the thermal comfort indices, but it in turn significantly increases energy consumption. Best performance in terms of thermal comfort is achieved with fast cabin air temperature controller tuning and comfort-oriented allocation cost, where the comfort index C_2 is 33% lower than in the nominal case, with only 13% more energy consumption. Also, for the case of fast cabin air temperature controller tuning, different allocation costs result in marginal thermal comfort differences; thus, the efficiency-oriented cost is the most suitable in that case. In the case of moderate controller tuning, combined allocation cost function case appears to be a reasonable choice, as it falls approximately in the middle between the two extreme cases (comfort-oriented and efficiency-oriented ones).

Table 5: Cumulative energy efficiency and thermal comfort indices for cool-down scenario and different control strategy settings.

Cabin controller setting[1]	Control allocation trade-off[2]	E_{com} [Wh]	C_1 [-]	C_2 [-]
Moderate	Comfort-oriented	171.2 (+12%)	159.6 (-5.1%)	117.6 (-3.7%)
Moderate	Efficiency-oriented	144.2 (-5.5%)	178.2 (+5.9%)	136 (+11%)
Moderate	**Combined cost**	**152.6 (0%)**	**168.2 (0%)**	**122.2 (0%)**
Slow	Comfort-oriented	180.7 (+18%)	237.1 (+41%)	217.2 (+77%)
Slow	**Efficiency-oriented**	**114.4 (-25%)**	**305.3 (+81%)**	**282.2 (+130%)**
Slow	Combined cost	146.6 (-3.9%)	257.9 (+53%)	227.3 (+85%)
Fast	Comfort-oriented	172.6 (+13%)	164.2 (-2.4%)	82.1 (-33%)
Fast	**Efficiency-oriented**	**167.8 (+10%)**	**162.3 (-3.5%)**	**82.6 (-32%)**
Fast	Combined cost	168.1 (+10%)	162.4 (-3.5%)	82.5 (-33%)

[1] Moderate: $K_i = 0.01$; Slow: $K_i = 0.02$; Fast: $K_i = 0.005$

[2] Comfort-oriented: $K_{PMV} = 1$, $K_{COP} = 0$; Efficiency-oriented: $K_{PMV} = 0$, $K_{COP} = 1$; Combined cost: $K_{PMV} = 0.5$, $K_{COP} = 1$;

The above analysis related to results presented in Figure 32 and Table 5 implies that in addition to the penalization factors K_{PMV} and K_{COP} of allocation cost function (10), the cabin air temperature controller tuning should be used in setting the trade-off between thermal comfort and efficiency to bring the controller performance even closer to the DP benchmark. Namely, for minimal energy consumption (efficiency-oriented design), the cabin air temperature controller response should be slower, and the control allocation should primarily be focused on efficiency, while for the thermal comfort-oriented design, the cabin air temperature

This project has received funding from the European Union's Horizon 2020 research and innovation programme under grant agreement No. 769826. The content of this publication is the sole responsibility of the Consortium partners listed herein and does not necessarily represent the view of the European Commission or its services.

controller response should be faster and control allocation can be set to combined case or even efficiency-oriented case. Moderate tuning of the cabin air temperature controller and combined cost function gives a reasonable trade-off between the two extreme cases.

3.5. Control strategy development for target EV HVAC system using multi-physical Dymola model

The target HVAC system presented in Section 2 and Figure 9 contains additional actuators (i.e. coolant pumps and valves) compared to the more conventional HVAC system from Subsection 3.1. The hierarchical control strategy for the target HVAC system is shown in Figure 33, and it is similar to the initially developed and verified strategy shown in Figure 29 (see Subsection 3.4.5).

At the lowest level, it combines feedback controllers commanding the compressor speed ω_{com} and expansion valve setpoints a_v, and open-loop actions of the main radiator and blower fans (i.e. the air mass flow rates $\dot{m}_{cf}$ and $\dot{m}_{bf}$, respectively) and the coolant pumps (i.e. pump speeds n_{p1}, n_{p2}, and n_{p3}). At the highest level, the cabin air temperature controller commands the cooling/heating capacity demand, which is transformed to low-level control system references/open-loop actions by means of optimal allocation maps. The allocated control inputs are:

- The speeds of coolant pumps 2 and 3, as these pumps directly transfer heat from the condenser to main radiator and evaporator to low-temperature radiator in the air conditioning mode, i.e. from the main radiator to evaporator and from condenser to heater core in the heat pump mode.
- The cabin inlet temperature reference $T_{cab,in,R}$ and blower fan air mass flow $\dot{m}_{bf}$, which directly influence the cabin inlet air temperature dynamics; it should be noted that these two inputs are mutually constrained through the cooling/heating capacity demand, so that only one of them is allocated ($T_{cab,in,R}$, herein) while the second one is then calculated from the power demand (see next Section for details).

The main radiator air mass flow $\dot{m}_{cf}$ is excluded from the optimisation as it may not directly affect cabin cooling or heating, and the power consumption of the main radiator fan is not accurately modelled due to influence of vehicle velocity. Thus, it is kept at the constant value defined by the Dymola model (0.3 kg/s). Similarly, the speed of Pump 1, n_{p1}, is set to a constant (20 Hz, as used in Dymola), as it does not affect the cabin cooling in the air-conditioning mode (Pump 1 cools the powertrain), and it is not used in the heat-pump without powertrain waste heat reuse operating mode (considered herein). As needed, the inputs $\dot{m}_{cf}$ and n_{p1} can readily be included in future optimizations. The superheat temperature reference $\Delta T_{SH,R}$ is set to the constant value of 5 K, which is a typical value for safe operation of the compressor.

Unlike in Subsection 3.4, where an instantaneous, on-line optimisation was applied, the allocation maps for the target HVAC control system are obtained using multi-objective genetic-algorithm-based optimisation, and they are then approximately implemented in a form of analytical functions. The allocation map optimisation procedure and corresponding results for both the cooling and heating modes are described in greater detail in the following subsection. The cabin temperature controller tuning, low-level feedback controller optimisation and gain-scheduling maps are reported in Subsection 3.7.

This project has received funding from the European Union's Horizon 2020 research and innovation programme under grant agreement No. 769826. The content of this publication is the sole responsibility of the Consortium partners listed herein and does not necessarily represent the view of the European Commission or its services.

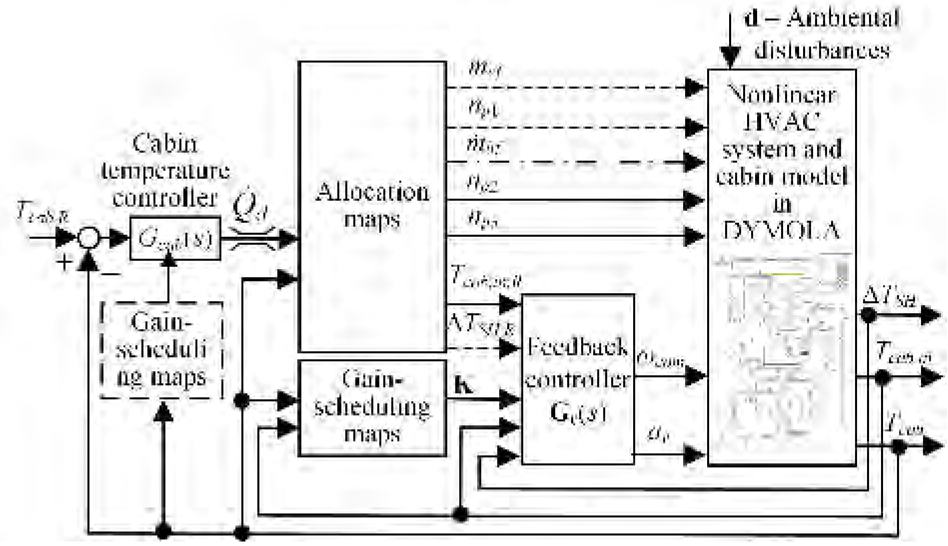

Figure 33: Block diagram of HVAC control system related to Dymola model HVAC dynamics

3.6. Optimal allocation of low-level control inputs

3.6.1. Optimal allocation problem

An off-line optimisation procedure has been developed to find optimal allocation maps of the overall control strategy from Figure 33. The optimal allocation problem is to find the control inputs (i.e. the coolant pump speeds and the cabin inlet air temperature reference) that minimize (or maximize) specified objective functions, while satisfying imposed set of constraints. Similar to the cabin thermal control strategy presented in Subsection 3.4, the cabin model is omitted from allocation map optimisation by imposing the cooling/heating capacity demand $\dot{Q}_d$ constraint at a specified cabin air temperature T_{cab}. The cooling capacity demand in the air-conditioning (A/C) operating mode $\dot{Q}_{d,AC}$ or heating capacity demand in heat-pump (HP) operating mode $\dot{Q}_{d,HP}$ is defined as

$$\begin{aligned} \dot{Q}_{d,AC} &= \dot{m}_{bf} c_{p,a} \left(T_{cab} - T_{cab,in,R}\right) \\ \dot{Q}_{d,HP} &= \dot{m}_{bf} c_{p,a} \left(T_{cab,in,R} - T_{cab}\right) \end{aligned} \tag{32}$$

respectively, where $c_{p,a}$ is the specific heat capacity of the cabin inlet air (set to the constant value of 1008 J/kg, the cabin inlet temperature reference $T_{cab,in,R}$ is the output of allocation map, while the blower fan air mass flow $\dot{m}_{bf}$ is determined by Eq. (32). Initially, the cabin air enthalpy h_a and cabin inlet air enthalpy were considered for evaluation of the thermal demand constraint Eq. (32), instead of the cabin and cabin inlet temperatures, as air enthalpy includes cabin air relative humidity φ_a, i.e. $h_a = f(T_a, \varphi_a)$. However, such approach is more complicated in terms of setting the optimisation constraints, hence a more simplified approach with fixed relative humidity and fixed air pressure is chosen and used throughout the report. Combination of the imposed thermal demand $\dot{Q}_d$ and cabin air temperature T_{cab} determines the operating point for the HVAC system and accounts for different thermal loads of the cabin (which are accounted for by the superimposed cabin air temperature controller) at different cabin temperatures.

Figure 34 shows the operating point grid used in optimisation for cooling (Figure 34a) and heating (Figure 34b) modes, respectively. Repeating the optimization procedure for each operating point yields optimal allocation maps of control inputs for a certain objective and imposed constraints. The optimisation results for

This project has received funding from the European Union's Horizon 2020 research and innovation programme under grant agreement No. 769826. The content of this publication is the sole responsibility of the Consortium partners listed herein and does not necessarily represent the view of the European Commission or its services.

the A/C mode showed that fewer points for cooling/heating capacity demand $\dot{Q}_d$ range were actually needed, so that the the grid for heating mode has been made less populated.

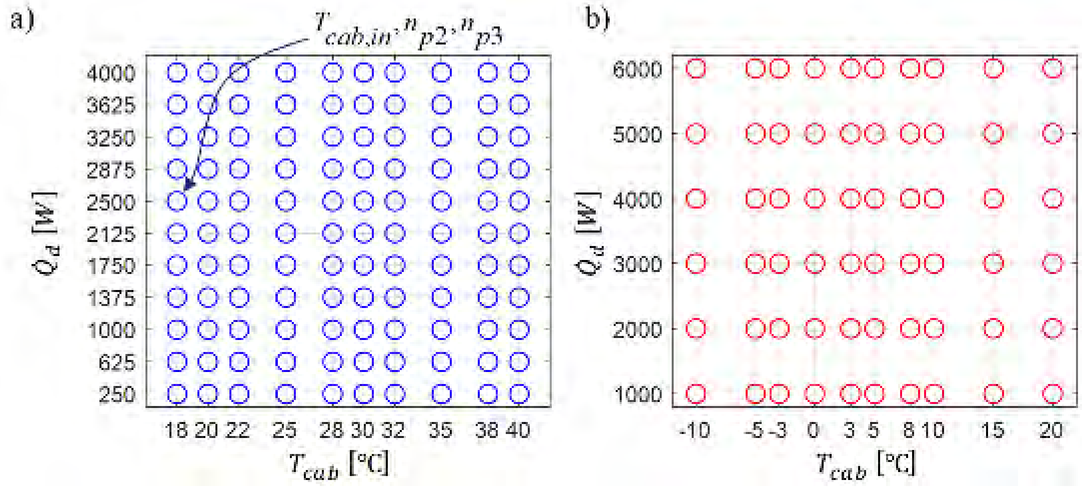

Figure 34: Control parameter optimisation operating point grid for air-conditioning mode (a) and heat pump mode (b)

Two different objective functions have been considered in optimisation. The first (and major) objective function J_1 maximizes the HVAC system efficiency defined in the form of coefficient of performance (COP):

$$J_1 = \max\,(COP) \tag{33}$$

where the COP is defined as:

$$\begin{aligned} COP_{AC} &= \frac{(\dot{Q}_{lat} + \dot{Q}_{sens})_{LTR}}{P_{com} + P_{p1} + P_{p2} + P_{p3}} \\ COP_{HP} &= \frac{\dot{Q}_{HC}}{P_{com} + P_{p1} + P_{p2} + P_{p3}} \end{aligned} \tag{34}$$

COP calculation accounts for the compressor power consumption P_{com} and the pump speeds power consumptions $P_{p1,2,3}$, while the unmodelled fan power consumptions (P_{af}, P_{bf}) are not included in the COP calculation. Both sensible $\dot{Q}_{sens}$ (which enters the cabin) and latent $\dot{Q}_{lat}$ (which is needed to dehumidify the cabin inlet air) heat power are accounted for in the air-conditioning mode.
The second (auxiliary) objective function maximizes the passenger thermal comfort by minimising the absolute value of predicted mean vote (PMV):

$$J_2 = \min\,(|PMV|) \tag{35}$$

where PMV is calculated using the map given in Figure 26 and described in Subsection 3.4.2.

For the case of a single objective function optimisation (typically J_1 or eventually J_2), a single optimal solution exists, while for the case of a multi-objective optimisation (simultaneous optimisation of J_1 and J_2) multiple optimal results form a Pareto frontier, which enables the designer to set an arbitrary trade-off between HVAC efficiency and passenger thermal comfort.

Two main constraints, which ensure optimal solution feasibility, are imposed to optimisation. The first one ensures that the cabin inlet temperature reference value (set by optimizer as control input) is achieved by the

This project has received funding from the European Union's Horizon 2020 research and innovation programme under grant agreement No. 769826. The content of this publication is the sole responsibility of the Consortium partners listed herein and does not necessarily represent the view of the European Commission or its services.

cabin inlet air temperature low-level feedback controller if possible (this may not be possible if the compressor speed is saturated), and it is expressed as:

$$|T_{cab,in,R} - T_{cab,in}| < 1\ °C$$

The second one ensures that the target cooling/heating capacity demand specified by the operating point is achieved at cabin inlet if possible (this may not be possible if the blower fan is saturated), and it is expressed as:

$$|\dot{Q}_d - \dot{m}_{bf} c_{p,a}\ (\underline{T_{cab}} - T_{cab,in})| < 100\ \mathrm{W}.$$

Constraints on other control inputs (pump speeds, blower fan air mass flow, compressor speed and EXV opening area) are set to reflect the hardware constraints:

$$\begin{gathered} 60\ \mathrm{rpm} \le n_{p2,3} \le 6610\ \mathrm{rpm}, \\ 0.01\ \mathrm{kg/s} \le \dot{m}_{bf} \le 0.15\ \mathrm{kg/s}, \\ 300\ \mathrm{rpm} \le \omega_{com} \le 9000\ \mathrm{rpm}, \\ 10^{-8}\ \mathrm{m}^2 \le a_v \le 10^{-6}\ \mathrm{m}^2. \end{gathered} \tag{36}$$

Finally, cabin inlet air temperature reference input $T_{cab,in,R}$ is constrained as given by:

$$\begin{gathered} 5\ °C \le T_{cab,in,R,\mathrm{AC}} \le 30\ °C, \\ 40\ °C \le T_{cab,in,R,\mathrm{HP}} \le 65\ °C. \end{gathered} \tag{37}$$

3.6.2. Optimisation method

The optimal allocation problem described in the previous subsection 3.6.1 is solved by using a multi-objective genetic algorithm-based optimisation tool, which was originally developed and validated for the generic HVAC system, and described in greater detail in [26].

The tool implements a three-stage allocation and feedback controllers' parameter optimisation approach [26], and it consists of the following steps:

1. Rough optimisation of all control inputs in an open-loop manner (all solid-line inputs to the nonlinear HVAC model in Figure 33) as described in Subsection 3.6.1;
2. Optimisation of feedback controller parameters ($\mathbf{G}_c\ (s)$ in Figure 33) for the optimal HVAC operating point obtained in the first step, as described in Subsection 3.4.4
3. Refined optimisation from Step 1 but for the open-loop control inputs only (pump speeds and fan air mass flows in Figure 33), while having the feedback controllers running, and thus automatically setting the remaining inputs (ω_{com} and a_v).

Note that repeating the optimisation procedure for the full operating point grid from Figure 34 yields the allocation and gain-scheduling maps in Figure 33. In [26] it was demonstrated on the example of conventional HVAC system model (presented in Subsection 3.1) that the three-stage approach substantially improves the optimisation computational efficiency when compared to a single-stage optimisation approach relying on fine execution of the first step only (optimising all control inputs).

Since the Dymola model used herein included initial, fixed-gain proportional-integral (PI) feedback controllers, the first optimisation step was omitted. Hence, the third optimisation step is conducted first to obtain the allocation maps. Then, the second optimisation step is conducted to obtain gain-scheduling maps for the optimal operating points obtained by the third optimisation stage.

This project has received funding from the European Union's Horizon 2020 research and innovation programme under grant agreement No. 769826. The content of this publication is the sole responsibility of the Consortium partners listed herein and does not necessarily represent the view of the European Commission or its services.

3.6.3. Implementation of the optimisation method

Optimisation of HVAC control inputs has been carried out in modeFrontier software using the multi-objective genetic algorithm MOGA-II. The implemented workflow is shown in Figure 35a, and its central part corresponds to a MATLAB node (orange line). The MATLAB node feeds the control inputs determined by the genetic algorithm (green line) to the MATLAB-Dymola interface, which then returns constraint-related variables (red line), cost function variables (purple line), and other outputs (black line) for evaluation within the modeFrontier. The genetic algorithm then generates a new control input population based on the cost function and constraints evaluation and the overall optimisation process continues to run in the loop for a specified number of iterations. Before running the optimization routine, starting population of control variables (i.e. initial design) is generated as a quasi-random, Sobol sequence.

The MATLAB-Dymola interface contained in the MATLAB node and implemented in the form of MATLAB script, is used as a communication and post-processing intermediate between modeFrontier and Dymola model. Figure 35b illustrates this communication process. First, the HVAC model is compiled in Dymola (this has to be done once) and an executable file *dymosim.exe* is generated with appropriate initialization file *dsin.txt*.

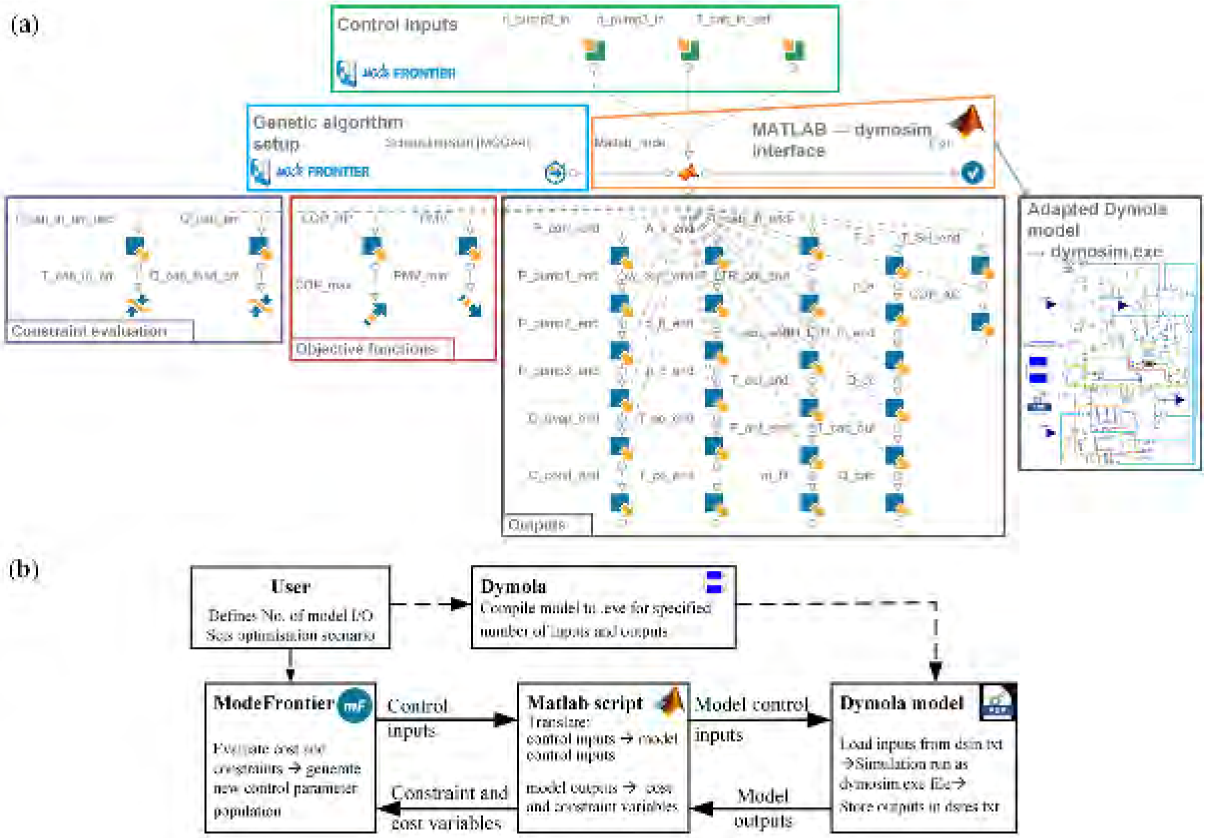

Figure 35: Multi-objective optimisation framework in modeFrontier (a), Flowchart depicting the optimisation loop and input/output processing within each environment (b)

The Dymola model used in the optimisation uses the control inputs (blower fan air mass flow, cabin inlet air temperature reference, pump speeds) and the initialization file contains all simulation-related parameters including the control inputs. The MATLAB script modifies the initialization file, namely changes the control inputs according to the values received from modeFrontier, runs an executable Dymola model, and finally calculates constraint-related and cost function related variables based on the simulation outputs and feeds them back to modeFrontier.

This project has received funding from the European Union's Horizon 2020 research and innovation programme under grant agreement No. 769826. The content of this publication is the sole responsibility of the Consortium partners listed herein and does not necessarily represent the view of the European Commission or its services.

An example of simulation response obtained within operating point optimization is shown in Figure 36. The control inputs are kept constant during the entire simulation response. Appropriately long period (1200s here) is provided for the system to settle after the initialization, i.e. reach steady-state output values that are stored and fed back to the optimization algorithm.

The optimization takes around 30 minutes for a single operating point and for 256 iterations of genetic algorithm. For the grid defined in Figure 34, the optimisations takes around 55h for A/C operating mode (110 operating points) and 30h for HP operating mode (60 operating points). It should be noted that the optimizations with three parallel design evaluations were conducted on personal computer based on Intel® Xeon® central processing unit operating at 3.6 GHz.

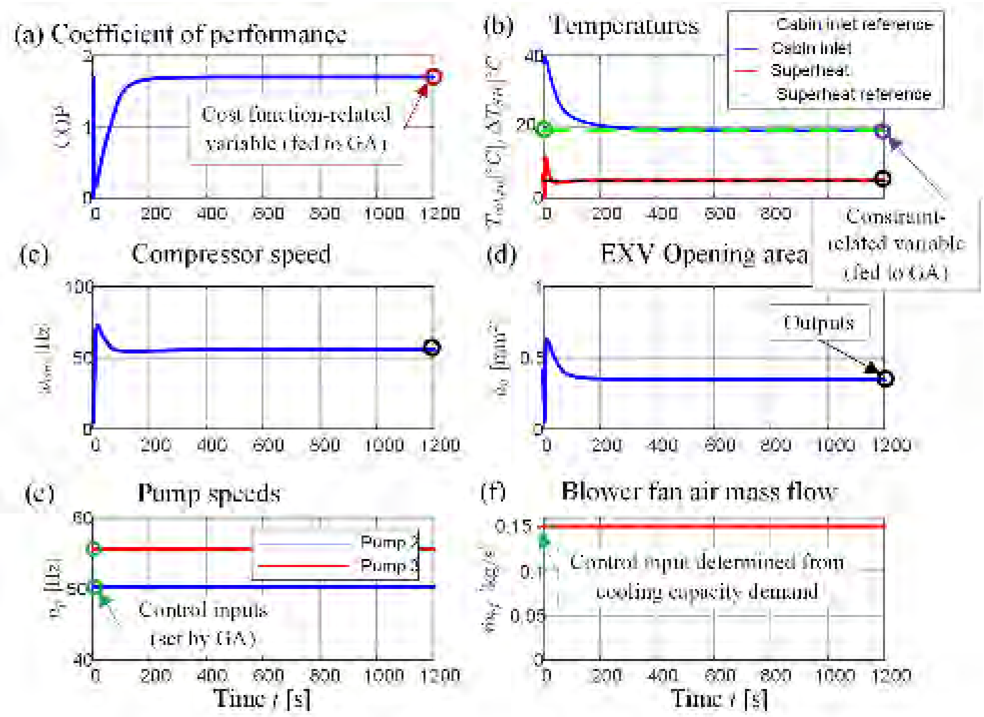

Figure 36: Time response of single Dymola model simulation executed within control input optimisation loop

3.6.4. Optimisation results for air-conditioning (A/C) operating mode for maximum system efficiency

Figure 37a-f show the A/C mode optimisation results (given by coloured lines) for the maximization of efficiency case, i.e. single-objective cost related to COP (Eq. (33)) subject to constraints Eq. (36) and Eq. (37). The HVAC system is in air-conditioning mode with fresh air intake and without reheat. The ambient air conditions are set to $T_a = 40$ °C, $\varphi_a = 25\%$, the vehicle velocity is kept at the constant value of $v_{veh} = 40\ km/h$ resulting in the front axial radiator mass flow rate $\dot{m}_{cf} = 0.3\ kg/s$.

The optimised pump speeds of evaporator-side pump and condenser-side pump, n_{p2} and n_{p3} (shown in Figure 37a and Figure 37b solid coloured lines) increase nearly linearly with the cooling capacity demand $\dot{Q}_d$ for a fixed cabin air temperature T_{cab}. For maximum efficiency, the cabin inlet air temperature references $T_{cab,in,R}$ (Figure 37c) are kept as close to the ambient value of 40 ºC as possible, i.e. its upper limit of 30 ºC, because this enables the compressor to operate at lower speed (Figure 37f), thus resulting in lower compressor power consumption P_{com} and greatly improving COP (Figure 37e). In return, to provide the demanded cooling power, the blower fan air mass flow is saturated to its upper limit (Figure 37d) for most of the operating points (note

This project has received funding from the European Union's Horizon 2020 research and innovation programme under grant agreement No. 769826. The content of this publication is the sole responsibility of the Consortium partners listed herein and does not necessarily represent the view of the European Commission or its services.

that leaning to high blower air mass flows may be connected with absence of blower fan power consumption model). The COP peaks at around 6.5 for the case of high cabin temperature T_{cab} and low cooling capacity demand $\dot{Q}_d$ (low compressor speed), while it tends to take the lowest value of 1 for highest cooling capacity demand $\dot{Q}_d$ (the compressor speed is high in those cases).

Distribution of optimal control input values given in Figure 37a-c makes them suitable for approximation with analytical expressions as a function of either cooling capacity demand $\dot{Q}_d$, cabin air temperature T_{cab} or both. To analyse the influence of individual pump speed (n_{p2}, n_{p3}) on the overall system efficiency and operation, four different approximations were considered: constant approximation based on the minimum, maximum and mean pump optimal speed and linear fit of data as a function of cooling capacity demand $\dot{Q}_d$. Quality of control input approximations is evaluated using the absolute ($COP_{abs,diff}$) and relative ($COP_{rel,diff}$) difference, i.e. the difference between the COP achieved with optimal control inputs (COP_{opt}) and approximated control inputs (COP_{approx}):

$$COP_{abs,err} = |COP_{opt} - COP_{approx}|$$
$$COP_{rel,err} = \frac{|COP_{opt} - COP_{approx}|}{COP_{opt}} * 100\ [\%] \tag{38}$$

The minimum/maximum constant approximations of pump speeds had major impact on system efficiency, whereas the linear fit expectedly resulted in small increase of COP over the complete operating range. The linear fit is conducted numerically in MATLAB using the functions from the Curve Fitting toolbox and the following functions are obtained:

$$n_{p2,lin}[\mathrm{rpm}] = 0.5199\dot{Q}_d[\mathrm{W}] + 1398.63$$
$$n_{p3,lin}[\mathrm{rpm}] = 0.5954\dot{Q}_d[\mathrm{W}] + 1551.76 \tag{39}$$

Note that for the simplicity of implementation and calibration the pump speeds are approximated as functions of cooling capacity demand only (i.e. the secondary influence of cabin temperature T_{cab} is disregarded). Linear approximation of pump speeds given by Eq. (39) is shown in Figure 37a-b by black solid line.

The cabin inlet air temperature reference $T_{cab,in,R}$ is approximated as a linear function of both the cooling capacity demand $\dot{Q}_d$ and cabin air temperature T_{cab}, and additional saturation-type constraint is imposed on the approximation:

$$T_{cab,in,R,lin}[°\mathrm{C}] = 0.9987T_{cab}[°\mathrm{C}] - 0.0067\dot{Q}_d[\mathrm{W}]$$
$$10 \leq \left(T_{cab,in,R,lin}\right)_{AC} < 30\ [°\mathrm{C}] \tag{40}$$

This additional constraint is imposed since optimised control input values for low cabin temperatures T_{cab} = {18, 20, 22} [°C] are distinctively nonlinear, but roughly constant. Figure 37c shows the optimal cabin inlet air temperature (solid coloured lines) and approximated cabin inlet temperatures (dashed coloured lines).

Figure 37g and h show the absolute and relative COP difference caused by using linear approximation of all control inputs. The relative COP difference is below 10% in a wide range of operating conditions, with some operating points exhibiting high degradation (related to high cabin inlet temperature difference, cf. operating point T_{cab} = 35°C, $\dot{Q}_d$=250 W). Most importantly, the relative COP difference is low in the region of high cabin temperature (T_{cab} > 30°C) and high cooling capacity demands ($\dot{Q}_d$ > 1500 W), and low cabin temperatures (T_{cab} ~ 25°C) and low cooling capacity demands ($\dot{Q}_d \leq$ 1000 W), which are characteristic operating points to typical HVAC operation (e.g. in the cool-down scenario).

This project has received funding from the European Union's Horizon 2020 research and innovation programme under grant agreement No. 769826. The content of this publication is the sole responsibility of the Consortium partners listed herein and does not necessarily represent the view of the European Commission or its services.

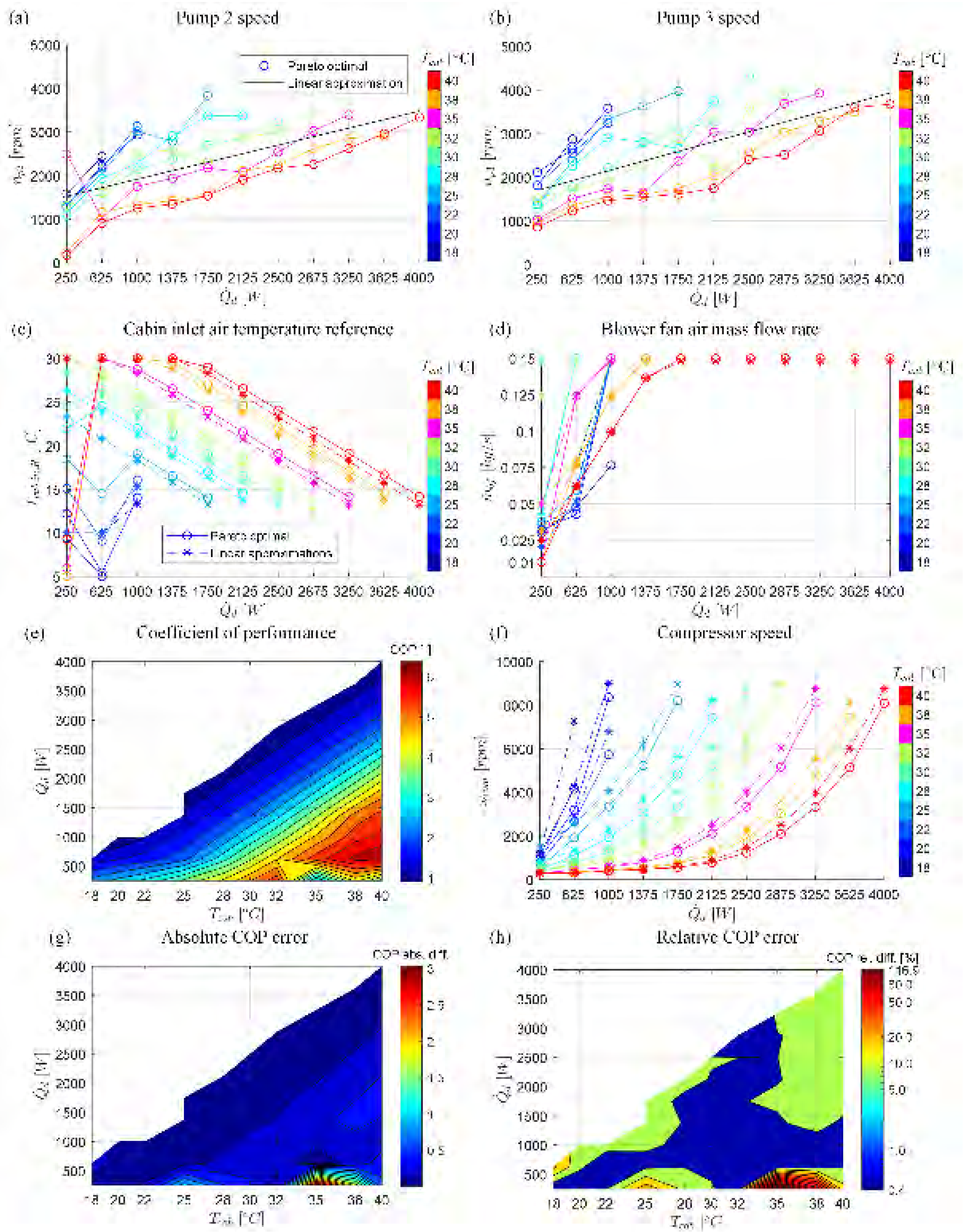

Figure 37: Control input allocation optimisation results for air-conditioning operating mode and COP maximisation case showing. Note that in subplots (a)-(f) solid lines correspond to optimal solutions and dashed lines to approximated solutions

This project has received funding from the European Union's Horizon 2020 research and innovation programme under grant agreement No. 769826. The content of this publication is the sole responsibility of the Consortium partners listed herein and does not necessarily represent the view of the European Commission or its services.

3.6.5. Influence of different ambient conditions on air-conditioning mode optimisation results

The optimisation results presented in Subsection 3.6.4 correspond to the nominal case related to the ambient temperature of 40°C and the vehicle velocity of 40 km/h. To investigate the influence of ambient temperature and vehicle velocity (and indirectly radiator fan speed) on optimisation results, the optimisation problem set in Subsection 3.6.3 has been solved for two additional cases: (i) ambient temperature reduced to 30°C with the vehicle velocity kept at 40 km/h, and (ii) vehicle velocity increased to 90 km/h with the ambient temperature kept at 40°C.

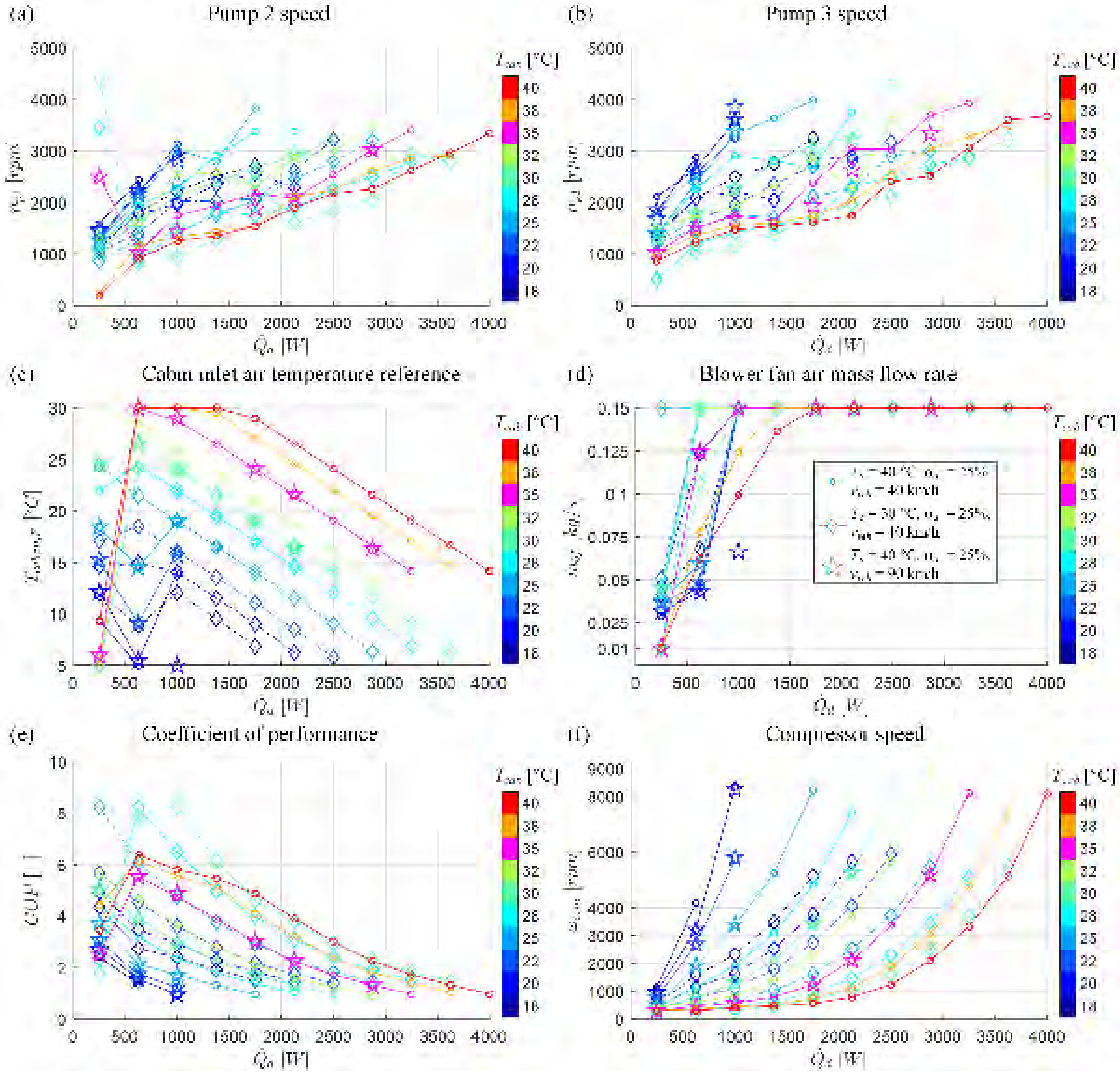

Figure 38: Comparison of air-conditioning mode optimisation results between nominal case (solid line w/ circles), decreased ambient temperature case (dashed line w/ diamonds) and increased vehicle velocity case (stars)

Figure 38 shows the comparison between optimisation results for the three aforementioned cases. The operating points corresponding to medium to high cooling capacities ($\dot{Q}_d > 2500$ W) become feasible at lower cabin temperature T_{cab} for the case of decreased ambient temperature. This is clearly visible in the cabin inlet temperature reference $T_{cab,in,R}$ in Figure 38c for the cabin inlet temperature references below 15°C. The cabin inlet temperature reference $T_{cab,in,R}$ and the blower fan air mass flow $\dot{m}_{bf}$ are the same for same cooling capacity

This project has received funding from the European Union's Horizon 2020 research and innovation programme under grant agreement No. 769826. The content of this publication is the sole responsibility of the Consortium partners listed herein and does not necessarily represent the view of the European Commission or its services.

demand $\dot{Q}_d$ and cabin temperature T_{cab} in all three cases, so that there is no need to reallocate these control inputs when the ambient temperature or vehicle velocity changes.

The pump speeds are grouped similarly in all three cases (Figure 38a and b), so that the allocation maps may be kept independent of ambient temperature and vehicle velocity. In the case of lower ambient temperature, the optimal pump speeds are, though, somewhat shifted to lower values for the same cooling capacity and cabin air temperature, because of lower thermal energy exchange between the coolant and ambient air (namely due to lower temperature difference). For the case of increased vehicle velocity, only the main radiator secondary coolant loop Pump 3 speed is affected to a certain degree as the heat dissipation at the radiator is increased.

It should also be noted that decrease in the ambient temperature results in higher COP, especially at higher cooling capacity demands (Figure 38e), because the compressor operates at lower speeds in this case (Figure 38f). On the other hand, the vehicle velocity has negligible influence on the overall HVAC efficiency.

3.6.6. Optimisation results for heat pump (HP) operating mode

Figure 40 shows the HP mode optimisation results for the maximization of efficiency case, i.e. the single-objective cost related to max(COP) (Eq. (33)), subject to the constraints given by Eq. (36) and Eq. (37). The HVAC system again operates with fresh air intake and does not use powertrain waste heat. The ambient air conditions are set to $T_a = -10$ °C, $\varphi_a = 80\%$, the vehicle velocity is kept at the constant value of $v_{veh} = 40\ km/h$ resulting in the front axial radiator mass flow rate $\dot{m}_{cf} = 0.3\ kg/s$.

Similar to the A/C operating mode (cf. Figure 38), the optimised pump speeds, n_{p2} and n_{p3} (shown in Figure 40a and Figure 40b with solid coloured lines) exhibit a linear-like increase with the heating capacity demand $\dot{Q}_d$, and do not largely depend on the cabin air temperature T_{cab}. Again, maximum efficiency is achieved for the cabin inlet air temperature reference $T_{cab,in,R}$ kept as close as possible to the ambient temperature (Figure 41c), i.e. set to its lower limit of 40°C, because this again enables the compressor to operate at lower speed (Figure 40f), thus greatly improving the COP (Figure 40e). Since the cabin inlet temperature reference is saturated at its lower limit for most of the operating points, the blower fan air mass flow $\dot{m}_{bf}$ linearly increases with increase of heating capacity demand (Figure 40d), and it also increases with the cabin temperature T_{cab} to meet the heating capacity demand. The COP peaks at around 3 for a not very realistic case of low cabin temperature T_{cab} and low heating capacity demand $\dot{Q}_d$ (low compressor speed), while it tends to take the lowest value of around 1.5 for high heating capacity demands $\dot{Q}_d$ and also high cabin temperatures (the compressor speed is high in those cases) – trend is similar to the A/C case.

Based on the above observations, the pump speeds are again approximated as linear functions of heating capacity demand (see bold lines in Figs. 41a and 41b):

$$\begin{aligned} n_{p2,lin}[\text{rpm}] &= 0.3569\dot{Q}_d[\text{W}] + 1155 \\ n_{p3,lin}[\text{rpm}] &= 0.6545\dot{Q}_d[\text{W}] + 943.5 \end{aligned} \tag{41}$$

Unlike in the A/C operating mode, the cabin inlet air temperature reference $T_{cab,in,R}$ is highly nonlinear with respect to cabin inlet temperature T_{cab} and heating capacity demand $\dot{Q}_d$. Therefore, the optimal blower fan air mass flow curves, $\dot{m}_{bf}$, are selected to be fitted, while $T_{cab,in,R}$ is then calculated from Eq. (32). The fit curves are described by a second-order polynomial function of the cabin air temperature T_{cab}, with the polynomial coefficients set to vary with the heating capacity demand $\dot{Q}_d$:

This project has received funding from the European Union's Horizon 2020 research and innovation programme under grant agreement No. 769826. The content of this publication is the sole responsibility of the Consortium partners listed herein and does not necessarily represent the view of the European Commission or its services.

$$\dot{m}_{bf} = k_1(\dot{Q}_d)T_{cab}^2 + k_2(\dot{Q}_d)T_{cab} + k_3(\dot{Q}_d) \quad (42)$$

The coefficients k_1, k_2, and k_3 are mapped as shown in Figure 39.

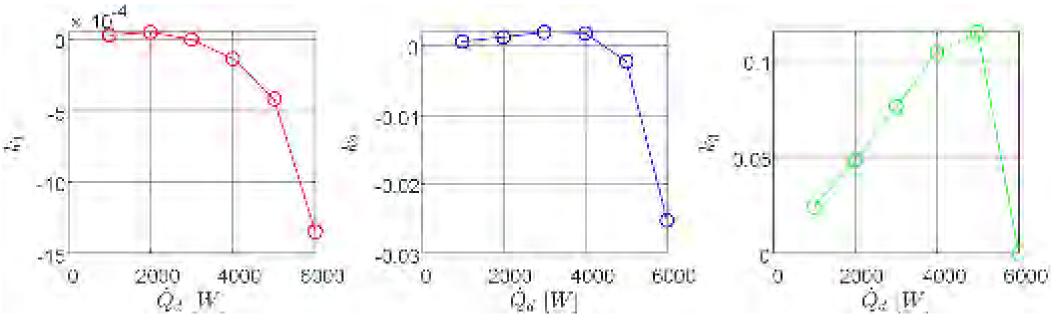

Figure 39: Blower fan air mass flow polynomial coefficients with respect to heating capacity demand

The quality of control input approximations is evaluated using the absolute and relative COP difference defined by Eq. (38). Figure 40g and h show the absolute and relative COP difference caused by approximating the control input curves. The relative COP difference is again below 10% in a wide range of operating conditions, and it is below 1% in the critical operating ranges characterized by low cabin temperature (T_{cab} < 10°C) and high heating capacity demands ($\dot{Q}_d$ > 3000 W), and high cabin temperatures (T_{cab} > 15°C) and low heating capacity demands ($\dot{Q}_d \leq 3000$ W).

This project has received funding from the European Union's Horizon 2020 research and innovation programme under grant agreement No. 769826. The content of this publication is the sole responsibility of the Consortium partners listed herein and does not necessarily represent the view of the European Commission or its services.

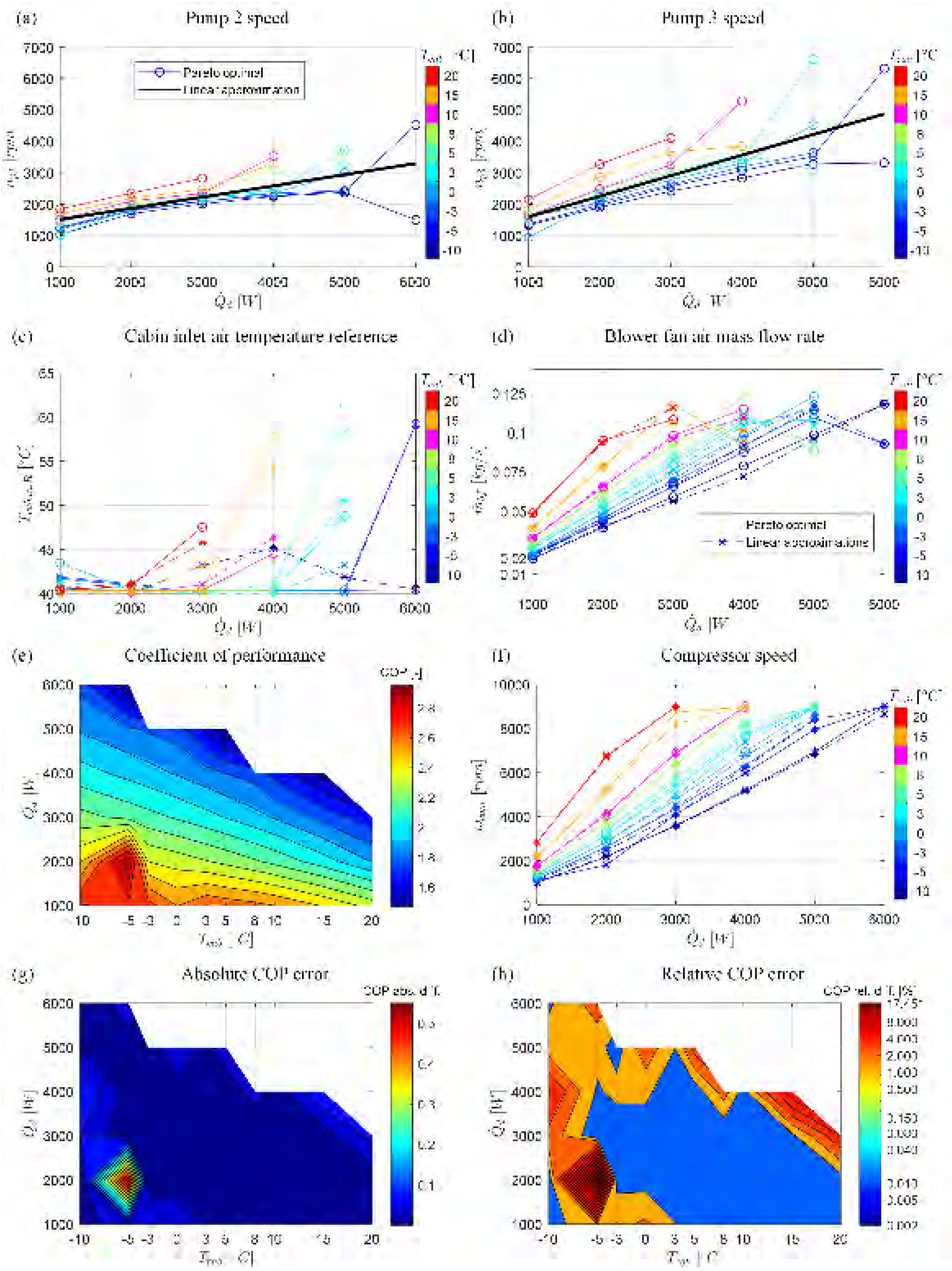

Figure 40: Control input allocation optimisation results for heat pump operating mode and COP maximisation case showing: Pump 2 speed n_{p2} (a), Pump 3 speed n_{p3} (b), cabin inlet air inlet temperature $T_{cab,in,R}$ (c), blower fan air mass flow $\dot{m}_{bf}$ (d) optimal COP (e), compressor speed ω_{com} (f), and absolute COP difference (g) and relative COP difference (h) when using approximation curves (bold or dashed lines) instead of real optimisation results (solid lines)

This project has received funding from the European Union's Horizon 2020 research and innovation programme under grant agreement No. 769826. The content of this publication is the sole responsibility of the Consortium partners listed herein and does not necessarily represent the view of the European Commission or its services.

3.7. Multi-objective optimisation

Results presented in the previous subsections corresponded to optimisation of solely the HVAC efficiency, which may generally result in unfavourable thermal comfort, especially around the cabin temperatures which are considered to be comfortable (around 23°C). This may be emphasised in the A/C operating mode, where the HVAC efficiency-oriented optimisation often saturates the blower fan to its maximum value, while the thermal comfort is worsened by increasing the blower fan air mass flow at cabin temperatures below 25°C (see Figure 26b).

In this subsection, optimisations are conducted for both A/C and HP operating modes for the case of simultaneously maximising the COP cost defined by Eq. (34) and minimising the PMV index given by Eq. (35), subject to constraints defined by Eq. (36) and (37). Note that the grid sizes depicted in Figure 34 are reduced with respect to number of cabin temperature points (with the cooling/heating capacity demand discretisation remained the same), in order to reduce the optimisation execution time because the number of GA iterations is increased from 256 to 2000 for this more demanding, multi-objective optimisation.

3.7.1. Multi-objective optimisation results for A/C operating mode

Figure 41 shows the Pareto frontiers obtained for four different cabin air temperatures and different cooling capacity demands for A/C operating mode, alongside the optimisation results of single cost function optimisation. At the cabin air temperature of 20°C (Figure 41a), there is a possibility for trade-off between efficiency (COP) and comfort (PMV), i.e. the thermal comfort can be increased at the expense of lower efficiency, but only at lower cooling capacity demands. The highest possibility for trade-off between efficiency and comfort exists at 25°C (Figure 41b), where it is possible to decrease the PMV for all cooling capacity demands. At higher cabin temperatures (Figure 41c and d), there is no trade-off between the efficiency and thermal comfort. Namely, both cost functions have the optimum for same control inputs, regardless of cooling capacity demand. This is explained by the fact that at high cabin temperatures, high blower fan air mass flow simultaneously decreases PMV (see Fig. 27b) and increases COP.

Figure 42 shows details of the optimisation results for operating points corresponding to the cabin air temperature of 25°C, for which the highest possibility for efficiency vs. thermal comfort trade-off was observed. Relatively steep Pareto frontiers (Figure 42a) suggest that PMV can be significantly improved without sacrificing COP to great extent. E.g., for the cooling capacity demand of 1000 W, the PMV can be decreased to comfort range threshold of 0.5 (i.e. by 36% compared to maxCOP case) at the cost of decreased COP by 20%. The higher thermal comfort is achieved by blower fan air mass flow and cabin inlet temperature decrease, where the latter is saturated at its lower limit for the case of highest possible thermal comfort (i.e. minimum PMV). The cabin inlet air temperature has to decrease to maintain the cooling capacity demand in the presence of blower fan air mass flow reduction (note the hyperbolic curves in Figure 42c and Eq. (32). However, for relatively low cooling capacity demands, the HVAC efficiency-oriented solution (max(COP)) falls in the comfort range anyway ($|PMV| < 0.5$), thus indicating that it may not be necessary to trade-off the COP for PMV. This is explained by low blower fan air mass flow and relatively high cabin inlet air temperature (Figure 42c) in that case. The optimal pump speeds for different Pareto solutions and the same cooling power demand are grouped in a narrow range (Figure 42b), thereby indicating that previously proposed linear approximations can be used in the multi-objective optimisation case, as well.

This project has received funding from the European Union's Horizon 2020 research and innovation programme under grant agreement No. 769826. The content of this publication is the sole responsibility of the Consortium partners listed herein and does not necessarily represent the view of the European Commission or its services.

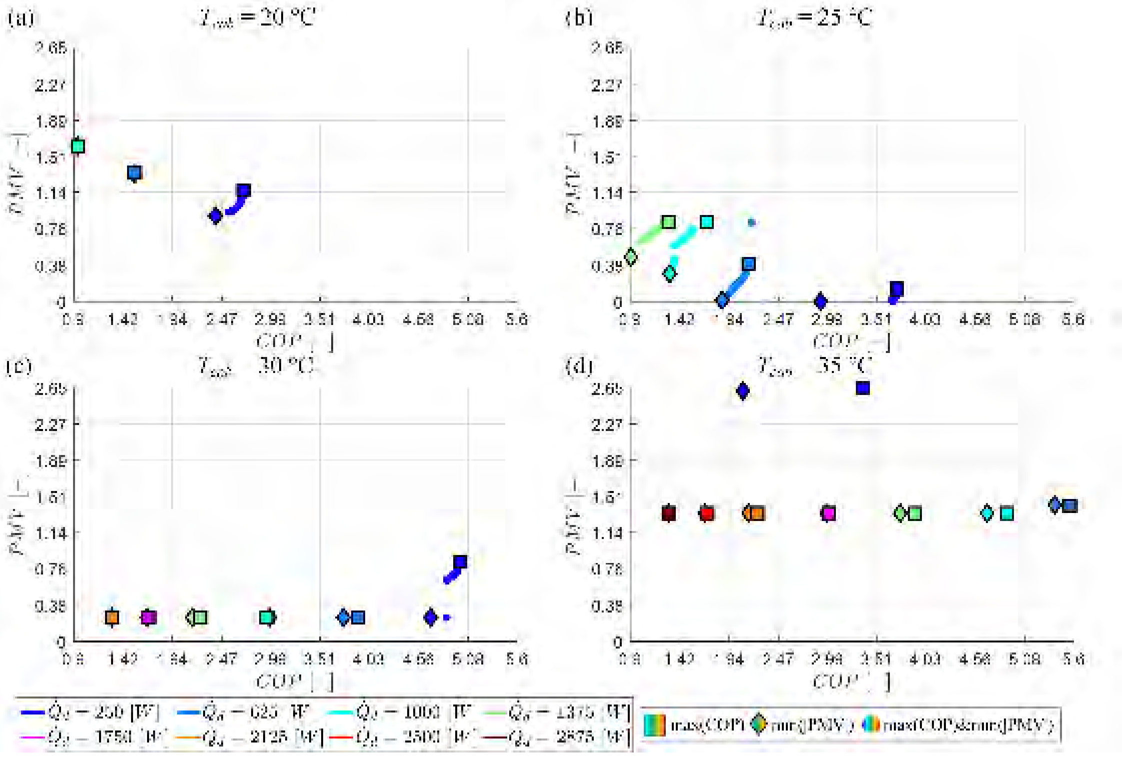

Figure 41: Multi-objective optimisation results for A/C mode, showing potential for achieving trade-off between COP maximisation and $|\mathrm{PMV}|$ minimisation for different cooling capacity demands and cabin air temperatures: T_{cab} = 20°C (a), T_{cab} = 25°C (b), T_{cab} = 30°C (c) and T_{cab} = 35°C (d)

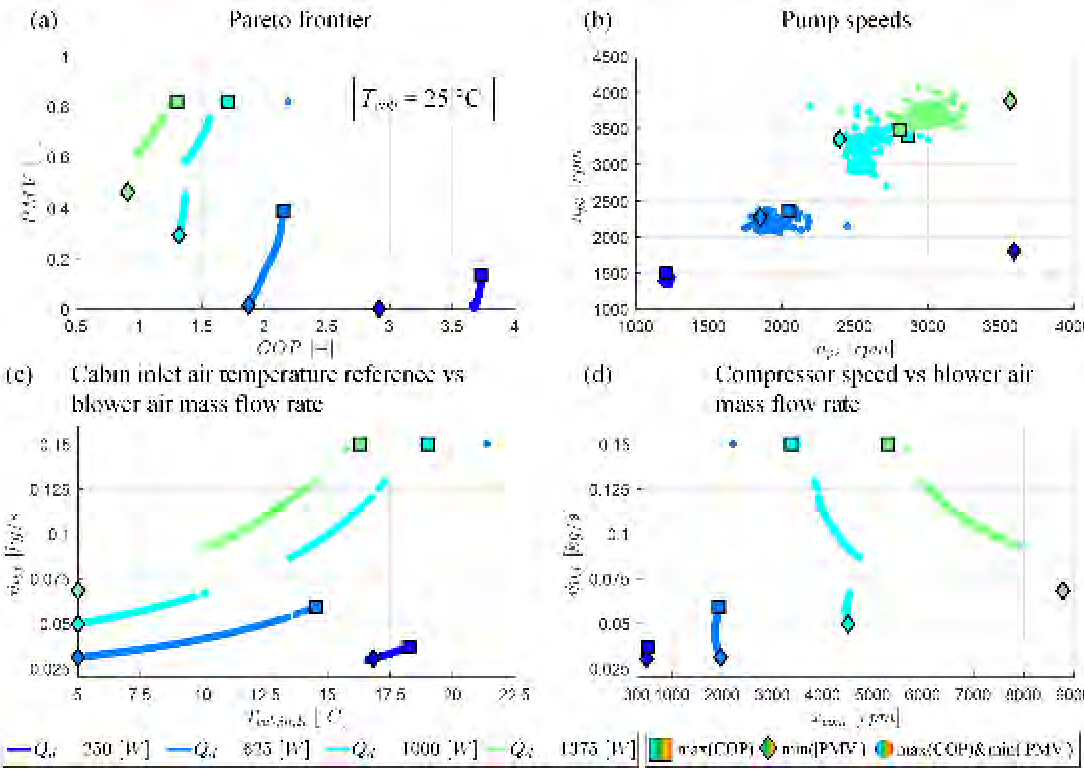

Figure 42: Detailed multi-objective optimisation results for cabin air temperature of 25°C and different cooling capacity demands: trade-off between PMV and COP (a), pump speeds (b), blower fan air mass flow vs cabin inlet air temperature reference (c) and compressor speed (d)

This project has received funding from the European Union's Horizon 2020 research and innovation programme under grant agreement No. 769826. The content of this publication is the sole responsibility of the Consortium partners listed herein and does not necessarily represent the view of the European Commission or its services.

3.7.2. Multi-objective optimisation results for HP operating mode

Figure 43 shows the Pareto frontiers obtained for the HP operating mode, and for four different cabin temperatures and several heating capacity demands. The trade-off between thermal comfort (minimum PMV) and efficiency (maximum COP) is now possible at all cabin temperatures. However, at lower cabin temperatures and low cooling capacity demands, the Pareto frontiers are almost flat, thus indicating that only marginal improvements of (already very low) thermal comfort can be achieved by significantly sacrificing HVAC efficiency. Therefore, in that operating region, the HVAC efficiency-oriented optimal solutions (squares) should be selected in application. As the cabin temperature increases towards comfort range (e.g. for 20°C), the Pareto frontiers become somewhat steeper and there is a good trade-off between comfort and efficiency (a clear comfort gain with a reasonable efficiency sacrifice). At the comfortable temperature of 25°C, all solutions of the Pareto frontier are in the comfort range (PMV < 0.5) and the Pareto frontiers are narrower (similar to the A/C case).

Figure 44 shows details of the optimisation results corresponding to the cabin air temperature of 25°C. Higher thermal comfort for certain operating point is achieved by decreased blower fan mass flow and increasing the cabin inlet temperature (this is also valid for lower cabin temperatures). However, at very low heating capacity demands, the Pareto frontier converges to single solution due to activation of the lower cabin inlet temperature limit (40°C). Similarly to the A/C case, the pump speeds of all solution are grouped in narrow range, i.e. their mapping is not connected with selecting the COP vs PMV optimal solution.

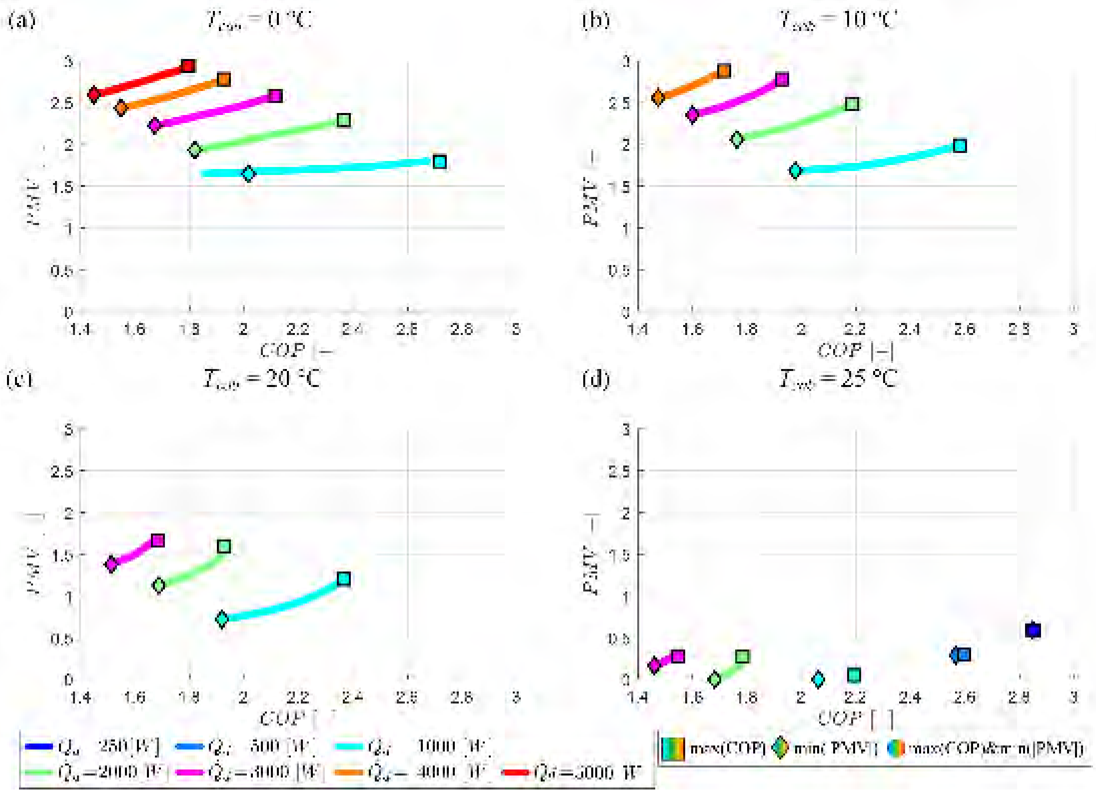

Figure 43: Multi-objective optimisation results for HP mode, showing potential for achieving trade-off between COP maximisation and │PMV│ minimisation for different cooling capacity demands and cabin air temperatures:

This project has received funding from the European Union's Horizon 2020 research and innovation programme under grant agreement No. 769826. The content of this publication is the sole responsibility of the Consortium partners listed herein and does not necessarily represent the view of the European Commission or its services.

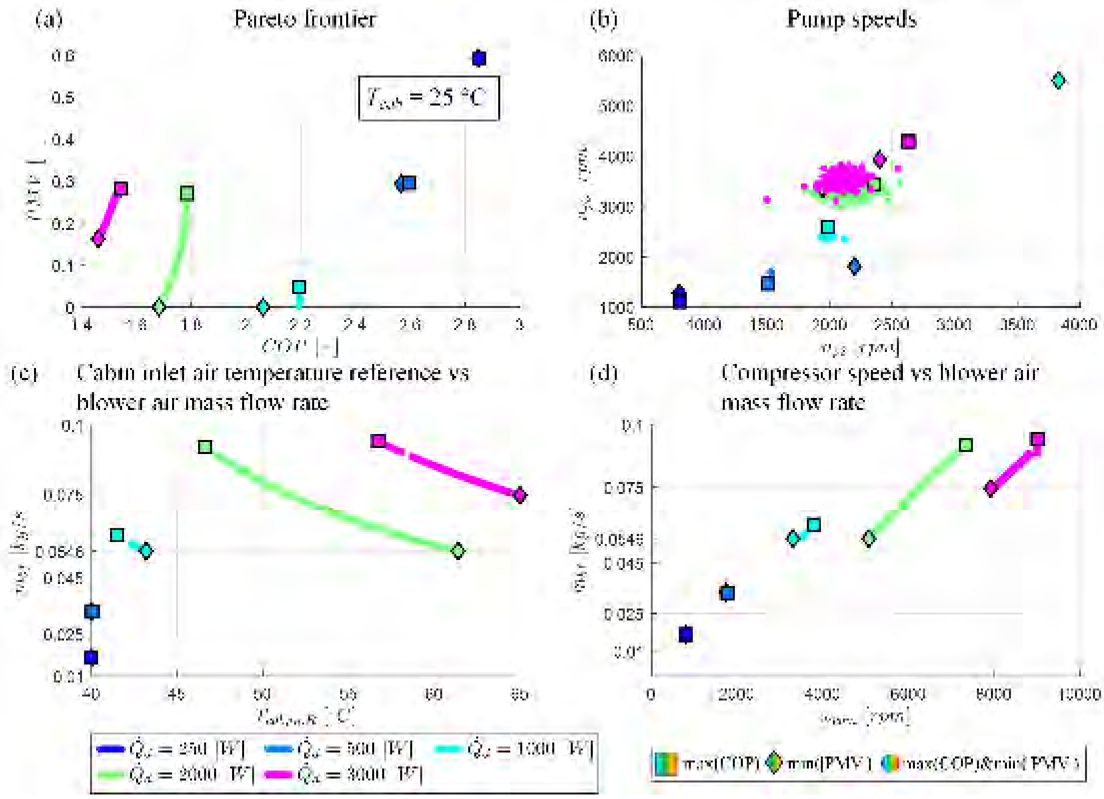

Figure 44: Detailed multi-objective optimisation results for cabin air temperature of 25°C and different heating capacity demands: trade-off between PMV and COP (a), pump speeds (b), blower fan air mass flow vs cabin inlet air temperature reference (c) and compressor speed (d)

This project has received funding from the European Union's Horizon 2020 research and innovation programme under grant agreement No. 769826. The content of this publication is the sole responsibility of the Consortium partners listed herein and does not necessarily represent the view of the European Commission or its services.

3.8. Tuning of high- and low-level feedback controllers

3.8.1. Optimisation of low-level feedback controller parameters

The modified PI controller structure shown in Figure 45 is used for superheat temperature and cabin inlet air temperature regulation. The modified PI controller includes the proportional gain placed in the feedback path only (instead of acting on the control error signal, cf. Figure 27) which has been found to be convenient from the standpoint of reducing the control effort with respect to change of reference signal. The controller parameters K_{p11}, T_{i11}, K_{p22}, and T_{i22} are obtained using the search-algorithm optimisation procedure described in Subsection 3.4.4. To facilitate the optimisation for different operating points, a two-pass optimisation is conducted with different r_{11}, r_{22}, and W settings (see the following subsections). In the first pass, the control effort is not penalized, i.e. $r_{ii} = 0$, $W = 0$, to obtain the fastest possible time response with optimisation window length M set to 3 times the highest time constant of MIMO system. In the second pass, the nominal control effort penalisation is used, and the parameter W is obtained from first pass time response as $W = k_{RT}W_0$, where $W_0 = \min(\text{index}(y(k) > 0.98\, y_R))$ and k_{RT} is multiplier (typically set to 1), i.e. W is set to rise-time of the first pass time response. The total optimisation window length is shortened to $M = 10W$.

Before running the optimisation, a linear MIMO ARX model of the HVAC system (see Subsection 3.3.3) is obtained by applying the previously developed identification tool (Subsection 3.3.3.) to the Dymola model open-loop step response for each operating point of the grid from Figure 18. Repeating the optimisation procedure for all operating points yields gain-scheduling maps. To further facilitate the implementation and on-vehicle calibration of gain-scheduling, a smaller number of operating points is chosen for final gain-scheduling map implementation. The results are given in the next two subsections for the A/C and HP modes.

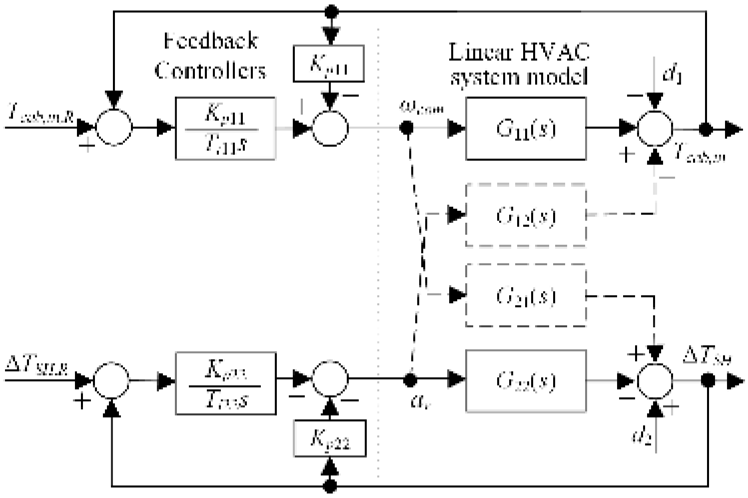

Figure 45: Block diagram of low-level control system comprising independent modified PI controllers and linearized HVAC system model

3.8.2. Low-level controller gain scheduling maps for A/C mode

Gain-scheduling maps for cooling regime (air-conditioning mode) are obtained for all operating points obtained for the case of HVAC efficiency maximisation. The control effort penalisations are set to $r_{11} = 0.1$ and $r_{22} = 0.01$. Figure 46 shows the contour plot of obtained gain-scheduling maps for all operating points, while Figure 47 shows the same results in a multiple 2D plot form. Note that the red crosses indicate the operating points that are chosen for obtaining reduced gain-scheduling map that is finally implemented in Dymola. The cabin inlet air temperature controller proportional gain K_{p11} increases in magnitude as the cooling capacity demand $\dot{Q}_d$ increases for fixed cabin temperature T_{cab}, while the corresponding integral time constant

This project has received funding from the European Union's Horizon 2020 research and innovation programme under grant agreement No. 769826. The content of this publication is the sole responsibility of the Consortium partners listed herein and does not necessarily represent the view of the European Commission or its services.

T_{i11} is practically constant for higher cabin air temperatures and high cooling capacity demands. Similarly, the superheat temperature controller proportional gain K_{p22} is practically constant for all operating points, while the integral time constant T_{i22} significantly increases only at lowest cooling capacity demand.

Figure 47 includes the comparison between optimised gains (solid lines) and implemented gain-scheduling map (dashed lines). For all four controller gains, the difference between optimised and implemented gains is small, which indicates that the gains can be optimized for smaller number of operating points and linearly interpolated for other operating points without loss of performance. Note that after initial verification test, the proportional gain K_{p11} has been limited to -50 (see Figure 47a) to reduce high compressor speeds and to ease initialization of the integral term.

For the purpose of low-level control system design verification, Figure 48 shows the closed-loop time response of linearized MIMO system (i.e. the one with included coupling dynamics of process, Figure 45) using optimised gains (green line) and implemented gains (blue line). The response is given for a typical operating point (the cabin air temperature of 25°C and the cooling capacity demand of 1000 W) in the small-signal operating mode. The target cabin inlet air temperature is reached within 100 s, while the superheat temperature is closely regulated around its target value. By limiting the cabin inlet temperature controller gain K_{p11} to -50, the compressor speed and EXV opening effort is reduced (Figure 48c,d), without any significant influence on control variable response (Figure 48a,b).

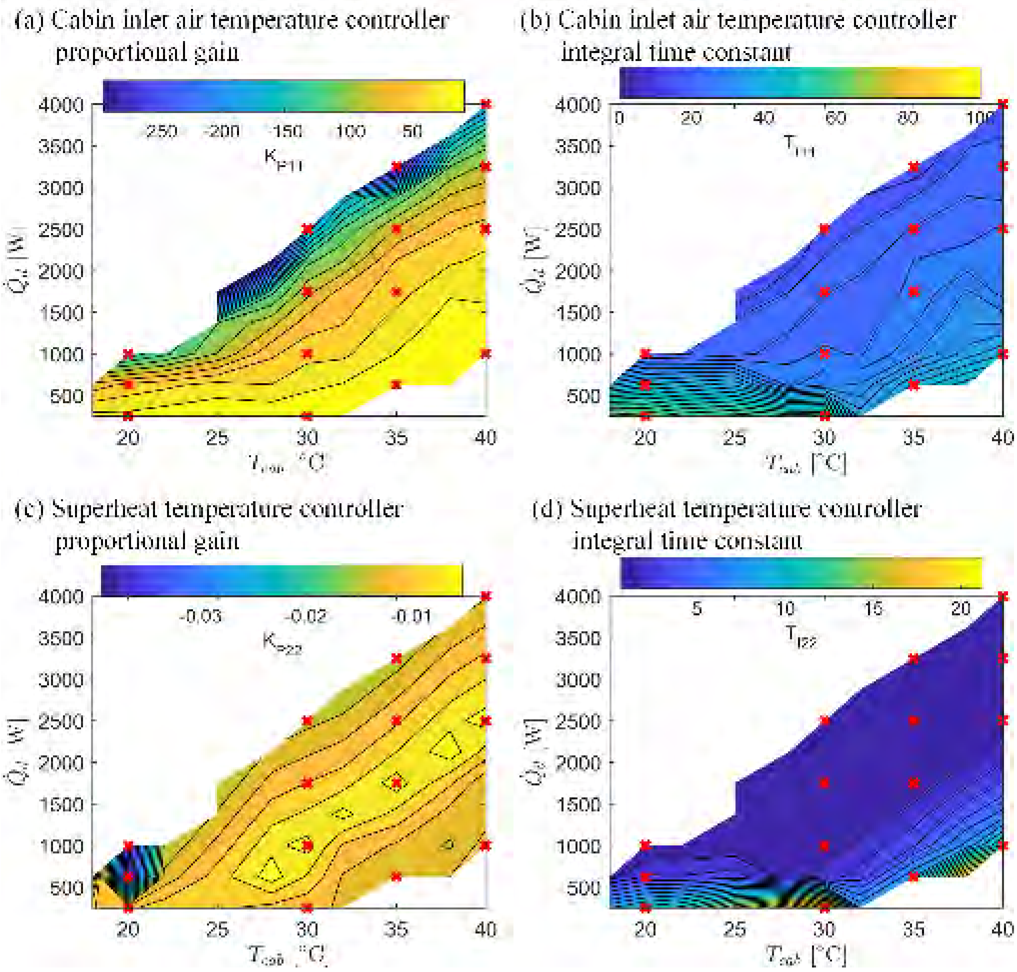

Figure 46: Contour plot showing optimised low-level feedback controller parameters for A/C operating mode (red crosses indicate operating points chosen for final mapping for implementation)

This project has received funding from the European Union's Horizon 2020 research and innovation programme under grant agreement No. 769826. The content of this publication is the sole responsibility of the Consortium partners listed herein and does not necessarily represent the view of the European Commission or its services.

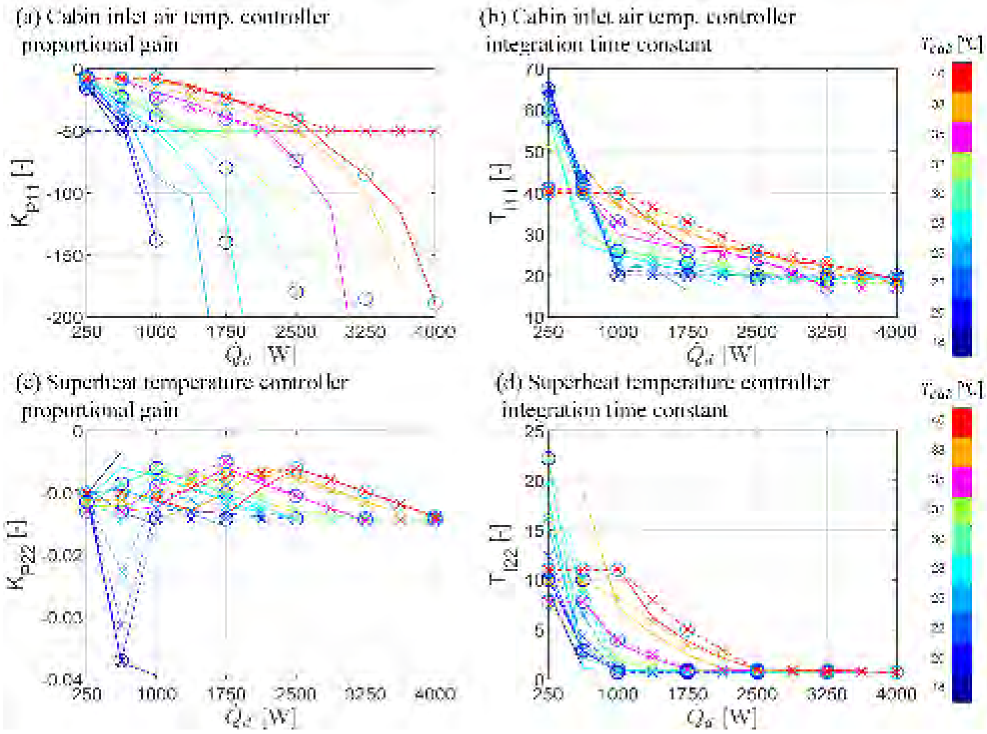

Figure 47: Comparison between optimized low-level controller gain-scheduling map (solid lines) and implemented/interpolated gain-scheduling map (dashed lines) for air-conditioning operating mode

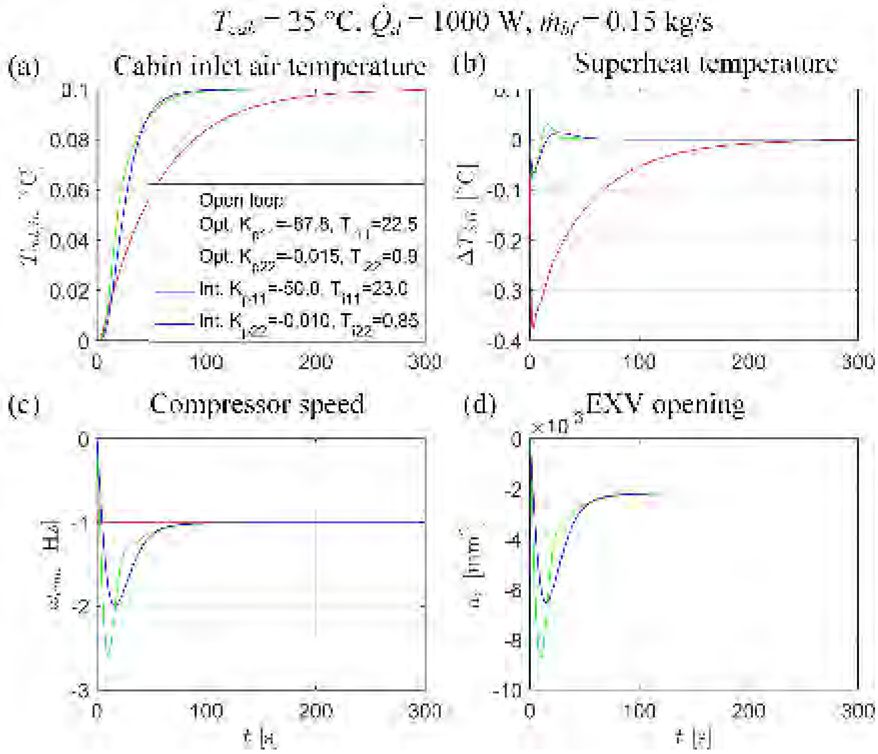

Figure 48: Closed-loop performance of linear MIMO system in open-loop (red line), using optimised gains (green line) and implemented gains (blue line) for air-conditioning operating mode

This project has received funding from the European Union's Horizon 2020 research and innovation programme under grant agreement No. 769826. The content of this publication is the sole responsibility of the Consortium partners listed herein and does not necessarily represent the view of the European Commission or its services.

3.8.3. Low-level controller gain-scheduling maps for HP mode

Gain-scheduling maps for heating regime (heat pump mode) are obtained for all operating points obtained for the max(COP) case. The control effort penalisations are set to r_{11} = 0.01 and r_{22} = 0.01. Figure 49 and Figure 50 show the contour and multi-2D plots of obtained gain-scheduling maps for all operating points. Note that the red crosses again indicate the operating points that are chosen for reduced gain-scheduling map that is finally implemented in Dymola. Cabin inlet air temperature controller proportional gain K_{p11} is again limited to 50, following the insights obtained from the air-conditioning mode. In the heat pump mode it is at this maximum value for almost all operating points. The integral time constant T_{i11} is lowest at highest heating capacity demands and increases as the heating capacity demand decreases for fixed cabin temperature. Similarly to the cabin air temperature controller parameters, the superheat temperature controller proportional gain K_{p22} is practically constant for all operating points, while the integral time constant T_{i22} increases with heating capacity demand decrease. Similarly to the A/C mode, the difference between optimised and implemented gains is marginal (Figure 50).

Figure 51 shows the closed-loop time response of linearized MIMO system using optimised gains (green line) and implemented gains (blue line) for a typical operating point (15°C and 2000 W) and in the small-signal operating mode. The target cabin inlet air temperature is reached within 100 s, while the superheat is closely regulated around the target temperature. Note that in heat-pump mode, the compressor speed and EXV opening overshoot is greatly increased compared to the air-conditioning mode (cf. Figure 48), thus indicating that the compressor might be often saturated in the large signal regime. This is mainly due to the slower dynamics of the heat pump mode compared to the air-conditioning mode, which may be caused by lower blower fan air mass flow setpoints in the heat pump case (the blower fan was saturated in the A/C operating mode, cf. Figure 48 and Figure 51).

This project has received funding from the European Union's Horizon 2020 research and innovation programme under grant agreement No. 769826. The content of this publication is the sole responsibility of the Consortium partners listed herein and does not necessarily represent the view of the European Commission or its services.

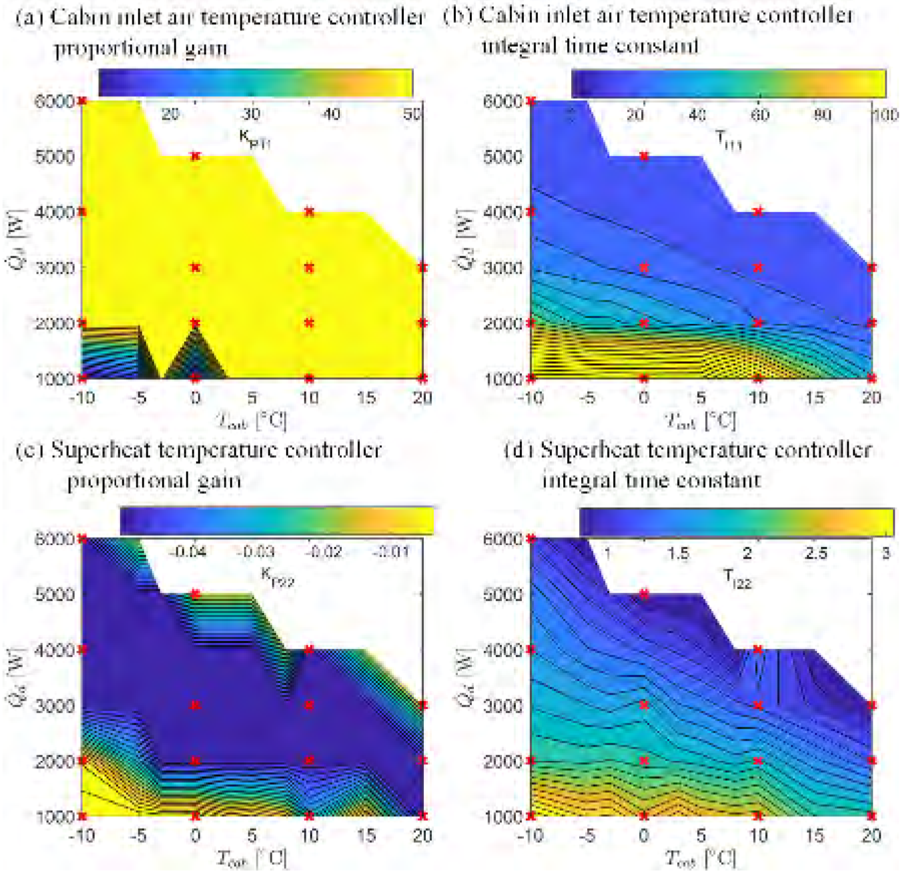

Figure 49: Contour plot showing feedback controller parameters for heat pump operating mode for all operating points (red crosses indicate operating points chosen for interpolation)

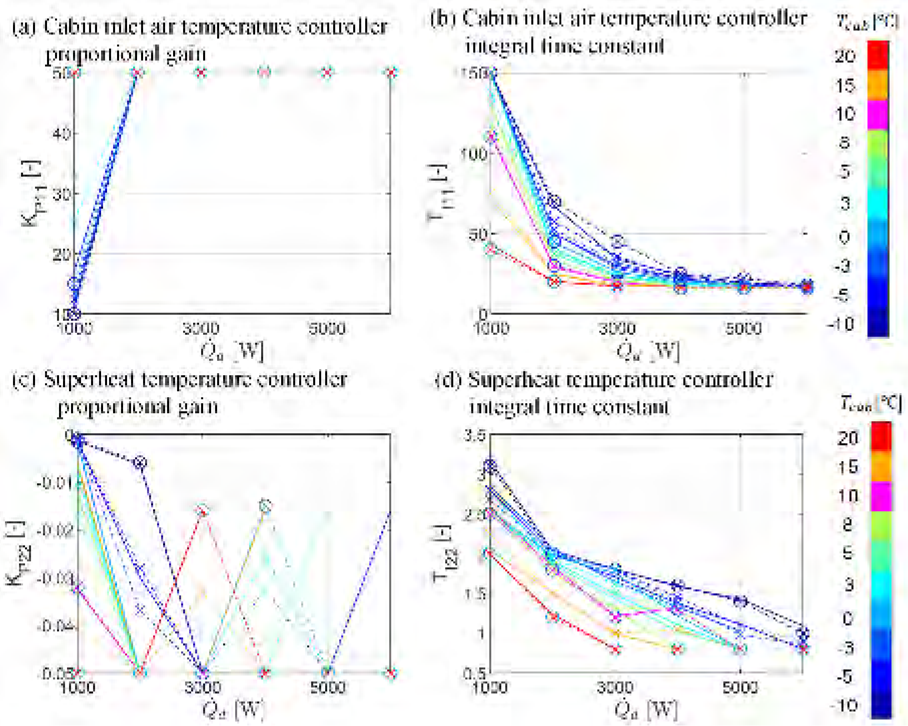

Figure 50: Comparison between optimized gain-scheduling map (solid lines) and interpolated gain-scheduling map (dashed lines) for heat pump operating mode

This project has received funding from the European Union's Horizon 2020 research and innovation programme under grant agreement No. 769826. The content of this publication is the sole responsibility of the Consortium partners listed herein and does not necessarily represent the view of the European Commission or its services.

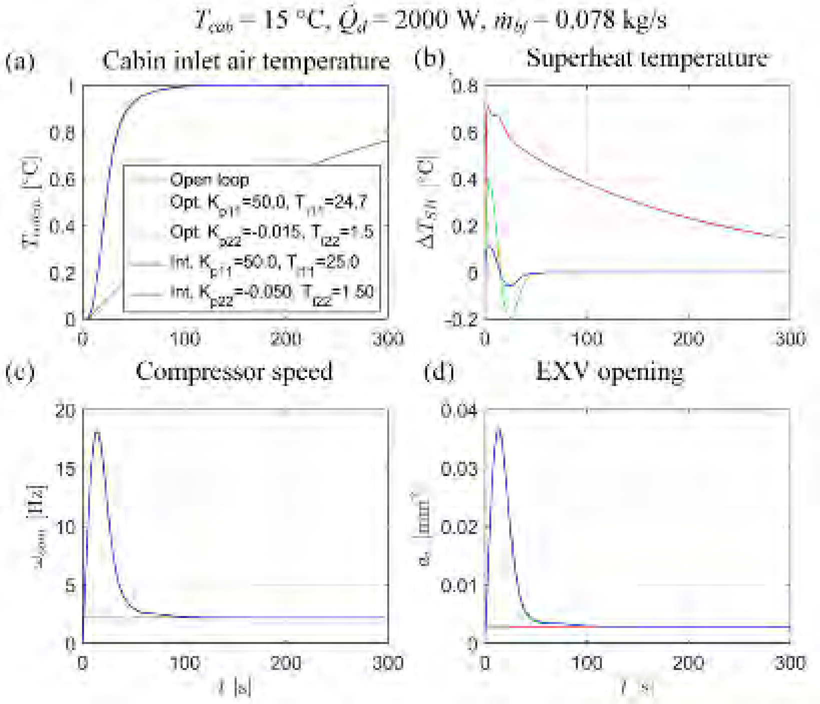

Figure 51: Closed-loop performance of linear MIMO system in open-loop (red line), using optimised gains (green line) and implemented gains (blue line) for heat pump operating mode

3.8.4. Tuning of superimposed cabin air temperature controller

The proportional-integral (PI) controller of superimposed cabin air temperature (Figure 33, see also Subsection 3.4.6) is implemented with fixed parameters (no gain-scheduling). Since the cabin air temperature dynamics are close to linear in terms of description of lumped cooling/heating capacities, and the environment distrubances to cabin air temperature are slow-acting, the controller with fixed gains shouldly result in satisfying performance.

Implementation of gain-scheduling might be considered to: (i) tune the cabin air temperature dynamics with respect to driver and/or powertrain commands, i.e. to set a trade-off between thermal comfort and efficiency in the cool-down/heat-up (see Subsection 3.4.6 for a detailed discussion and illustration), (ii) further improve the closed-loop performance in the presence of nonlinear effects. This would require identification of the inner control system (including the allocation maps) with respect to cooling/heating capacity demand step and preferably analytical method of superimposed control loop design.

This project has received funding from the European Union's Horizon 2020 research and innovation programme under grant agreement No. 769826. The content of this publication is the sole responsibility of the Consortium partners listed herein and does not necessarily represent the view of the European Commission or its services.

3.9. Dymola implementation of control strategy and verification of optimisation results

3.9.1. Overview of HVAC controller implementation in Dymola

Figure 53 shows the Dymola implementation of the overall HVAC control strategy represented by the block diagram in Figure 33. The same structure is valid for both the A/C and HP operating modes – only control parameters and allocation functions change with the operating mode. In the upper part of the Figure 53, a PI cabin air temperature controller is shown. It is extended with variable cooling/heating capacity limit with respect to cabin temperature (implemented in the form of look-up table that corresponds to the border of operating range, cf. Figure 37e and Figure 40e), to account for decrease in the cooling/heating capacity as the cabin temperature approaches the ambient temperature. In order to prevent high integrator value when the controller is saturated (so-called windup), a back-calculation anti-windup mechanism is implemented, with the back-calculation time constant set to square root of integral time constant. The middle part of the figure contains control input allocation blocks, i.e. pump speeds, cabin inlet temperature and blower fan air mass flow approximations as functions of cooling/heating capacity demand and cabin temperature (Eqs. (39) and (40) for the A/C case, and Eqs. (41) and (42) for HP case). The bottom part contains two modified PI controllers for superheat temperature and cabin inlet temperature regulation.

Figure 52 shows Dymola implementation of the modified PI controller including the gain-scheduling maps, which are implemented in the form of 2D look-up tables, see Figure 47 and Figure 50. The modified PI controllers also have back-calculation anti-windup mechanism with anti-windup time constant set to square root of integral time constant.

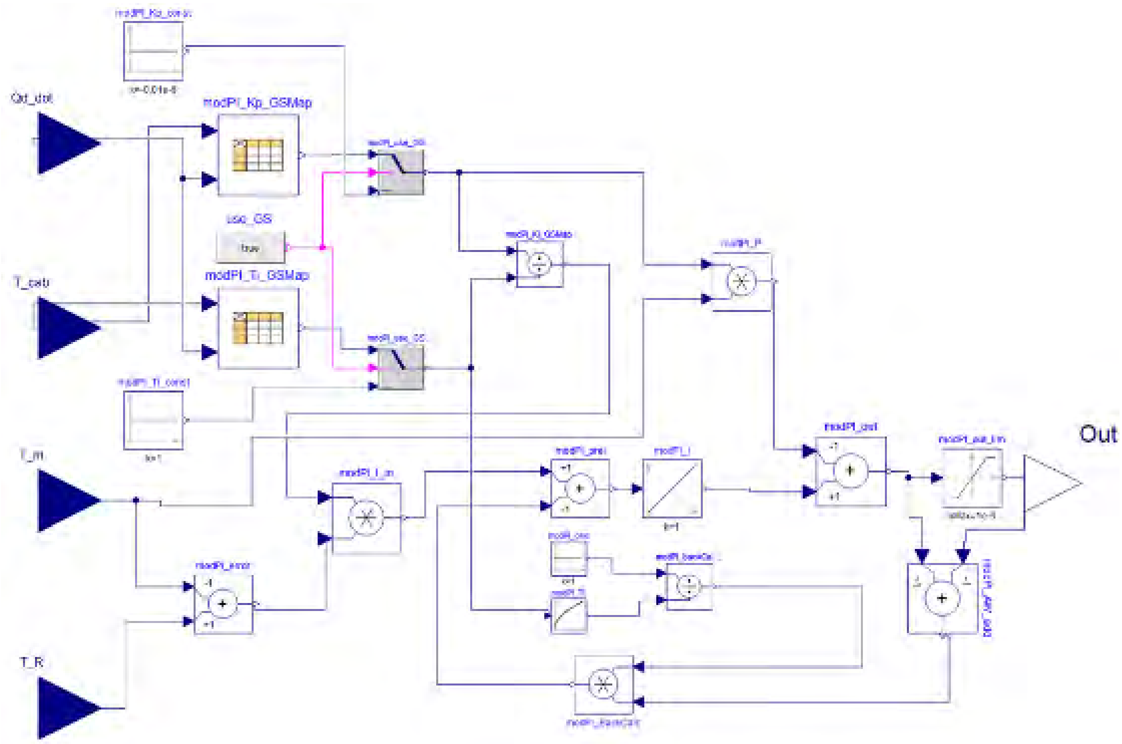

Figure 52: Modified PI controller with saturation logic and gain-scheduling maps, implemented in Dymola

This project has received funding from the European Union's Horizon 2020 research and innovation programme under grant agreement No. 769826. The content of this publication is the sole responsibility of the Consortium partners listed herein and does not necessarily represent the view of the European Commission or its services.

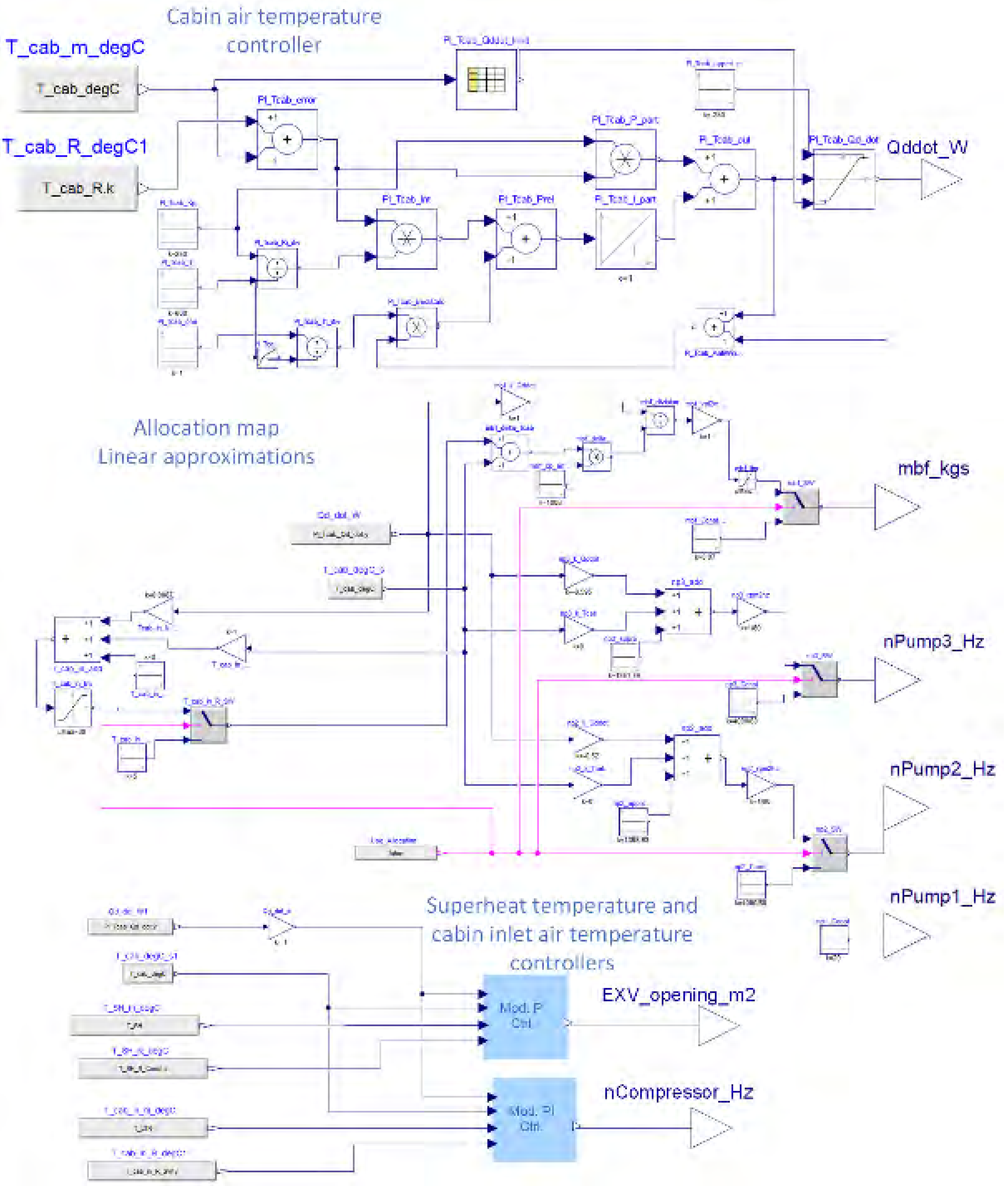

Figure 53: HVAC control strategy implemented in Dymola

3.9.2. Cool-down scenario simulation results

The control strategy parameterised for the A/C mode is verified in the cool-down scenario (cf. Subsection 3.4.6) for the case of ambient temperature of 40°C and vehicle velocity of 40 km/h. The target cabin air temperature is 25°C. The cabin temperature controller tuning is oriented towards thermal comfort (higher gains, cf. Figure 32) as the implemented allocation maps correspond to the case of maximal efficiency.

This project has received funding from the European Union's Horizon 2020 research and innovation programme under grant agreement No. 769826. The content of this publication is the sole responsibility of the Consortium partners listed herein and does not necessarily represent the view of the European Commission or its services.

Figure 54 shows the cool-down scenario results obtained in Dymola. The cabin air temperature (Figure 54a, green line) reaches the reference value (Figure 54a, black dashed line) in approximately 5 minutes, while the cabin inlet air temperature (Figure 54a, red line) reaches its reference set by the optimal allocation map in approximately 2 minutes (Figure 54a, blue line). The cooling capacity demand (Figure 54c) is saturated at the start of cool-down scenario and decreases as the cabin temperature approaches setpoint. Accordingly, the compressor is saturated and operates at the maximum speed at the start of cool-down response (Figure 54e). The allocation map sets the blower fan air mass flow (Figure 54b) close to maximum value, increases the cabin inlet temperature reference and decreases pump speeds (Figure 54d) as the cooling capacity demand decreases towards the steady conditions. The coefficient of performance (COP, Figure 54g) increases as the compressor speed decreases towards its steady-state value. Finally, the superheat temperature (Figure 54f) is accurately regulated around 5 K and the disturbances occuring from compressor speed changes are well supressed.

Figure 54i shows the cooling capacity demand vs cabin air temperature during the cool-down scenario. At the start of cool-down transient (high cabin temperature) the cooling capacity is close to maximum value and it remains close to the limit of operating range during the cool-down. This is in accordance with aforementioned high-gain tuning of the cabin temperature controller, i.e. to reaching a fast transient for good thermal comfort. Finally, the cooling capacity demand decreases as the cabin temperature is approaching the target value of 25°C. The actual cooling capacity (magenta crosses) is low at the start of the cool-down (this explains why the COP is close to 0 at the start of cool-down in Figure 54g), because the cabin inlet temperature is low, i.e. close to the ambient temperature. The actual and demanded cooling capacity differ until the cabin inlet temperature gets close to its setpoint value (the cabin temperature T_{cab} is around 30°C at that instant).

This project has received funding from the European Union's Horizon 2020 research and innovation programme under grant agreement No. 769826. The content of this publication is the sole responsibility of the Consortium partners listed herein and does not necessarily represent the view of the European Commission or its services.

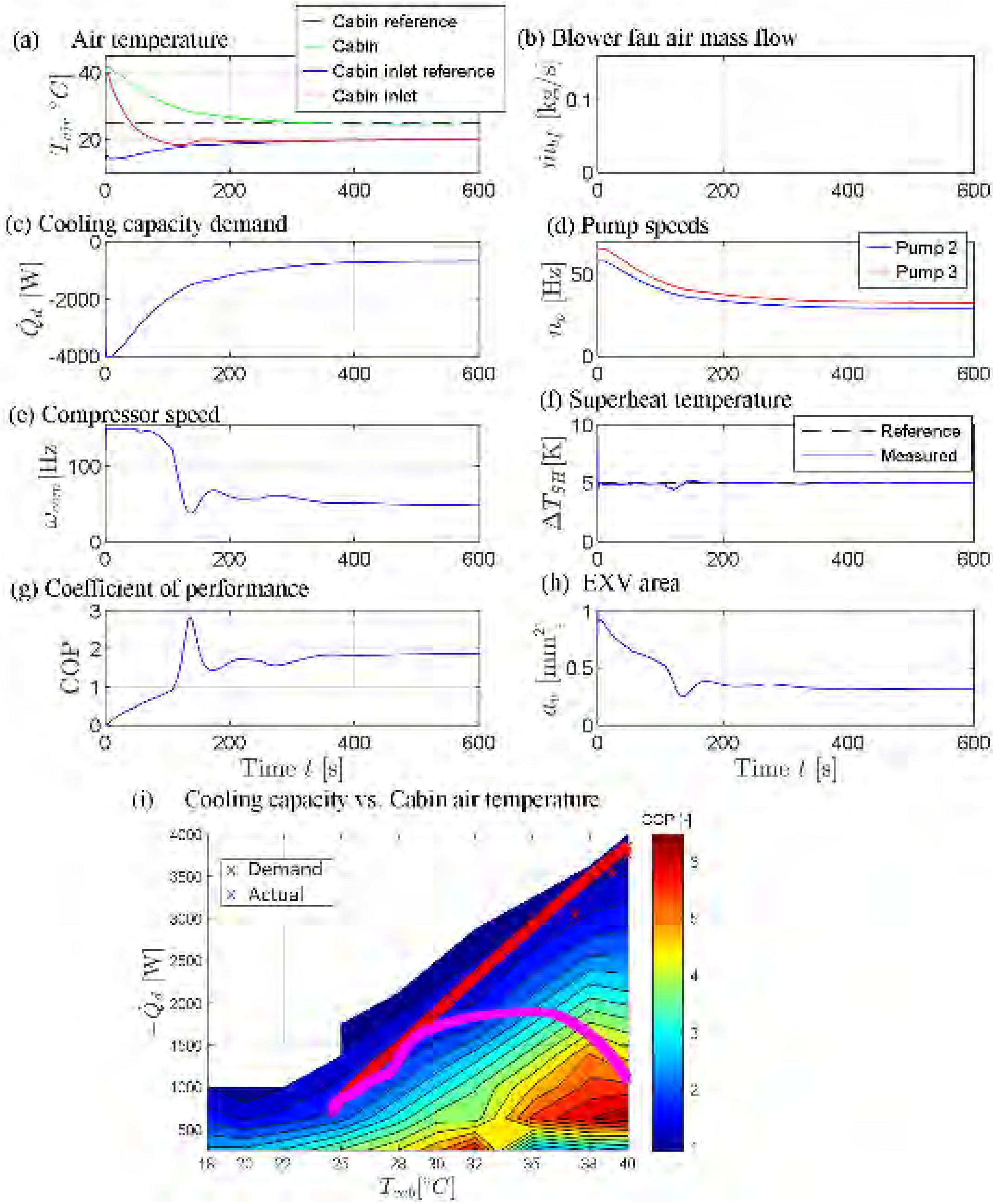

Figure 54: Simulation response of overall A/C control system implemented in Dymola, given for cool-down scenario

3.9.3. Heat-up scenario simulation results

The control strategy parameterised for the heat pump mode is verified in the heat-up scenario for the case of ambient temperature of -10°C and vehicle velocity of 40 km/h. The target cabin air temperature is 20°C.

Figure 55 shows the heat-up scenario response obtained in Dymola. The cabin air temperature (Figure 55a, green line) reaches its reference value (Figure 55a, black dashed line) in approximately 7 minutes, while the cabin inlet air temperature (Figure 55a, red line) reaches its reference set by allocation map (Figure 55a, blue line) in approximately 4.5 minutes. Similarly as in the cool-down scenario, the compressor is saturated and operates at maximum speed (Figure 55e) until the cabin inlet temperature reference is reached. Then, the

This project has received funding from the European Union's Horizon 2020 research and innovation programme under grant agreement No. 769826. The content of this publication is the sole responsibility of the Consortium partners listed herein and does not necessarily represent the view of the European Commission or its services.

compressor speed decreases to steady-state value. The heating capacity demand (Figure 55c), which is saturated at the start of heat-up scenario, decreases as the cabin temperature approaches its setpoint and settles to steady-state value required for maintaining the cabin temperature setpoint. Unlike in the air-conditioning operating mode, the allocation map sets the cabin inlet temperature (Figure 55a) to the minimum value of 40°C and decreases the blower fan air mass flow (Figure 55b) and also pump speeds (Figure 55d) as the heating capacity demand decreases. Similarly to the A/C mode, the coefficient of performance (Figure 55g) increases as the compressor speed decreases to its steady-state value and the superheat temperature (Figure 55f) is accurately regulated around 5 K.

Figure 55i shows the heating capacity demand vs cabin air temperature during the heat-up scenario. At the start of the heat-up (high cabin temperature) the heating capacity is close to maximum value and remains close to the limit of operating range during the heat-up transient. As the cabin temperature approaches the target value of 20°C, the heating capacity decreases to match the thermal load in steady-state conditions. Similarly as in the cool-down scenario, the actual heating capacity (blue crosses) is low at the start of the heat-up and matches the demanded heating capacity once the cabin inlet temperature reaches its setpoint value (the cabin temperature T_{cab} is around 15°C at that instant).

This project has received funding from the European Union's Horizon 2020 research and innovation programme under grant agreement No. 769826. The content of this publication is the sole responsibility of the Consortium partners listed herein and does not necessarily represent the view of the European Commission or its services.

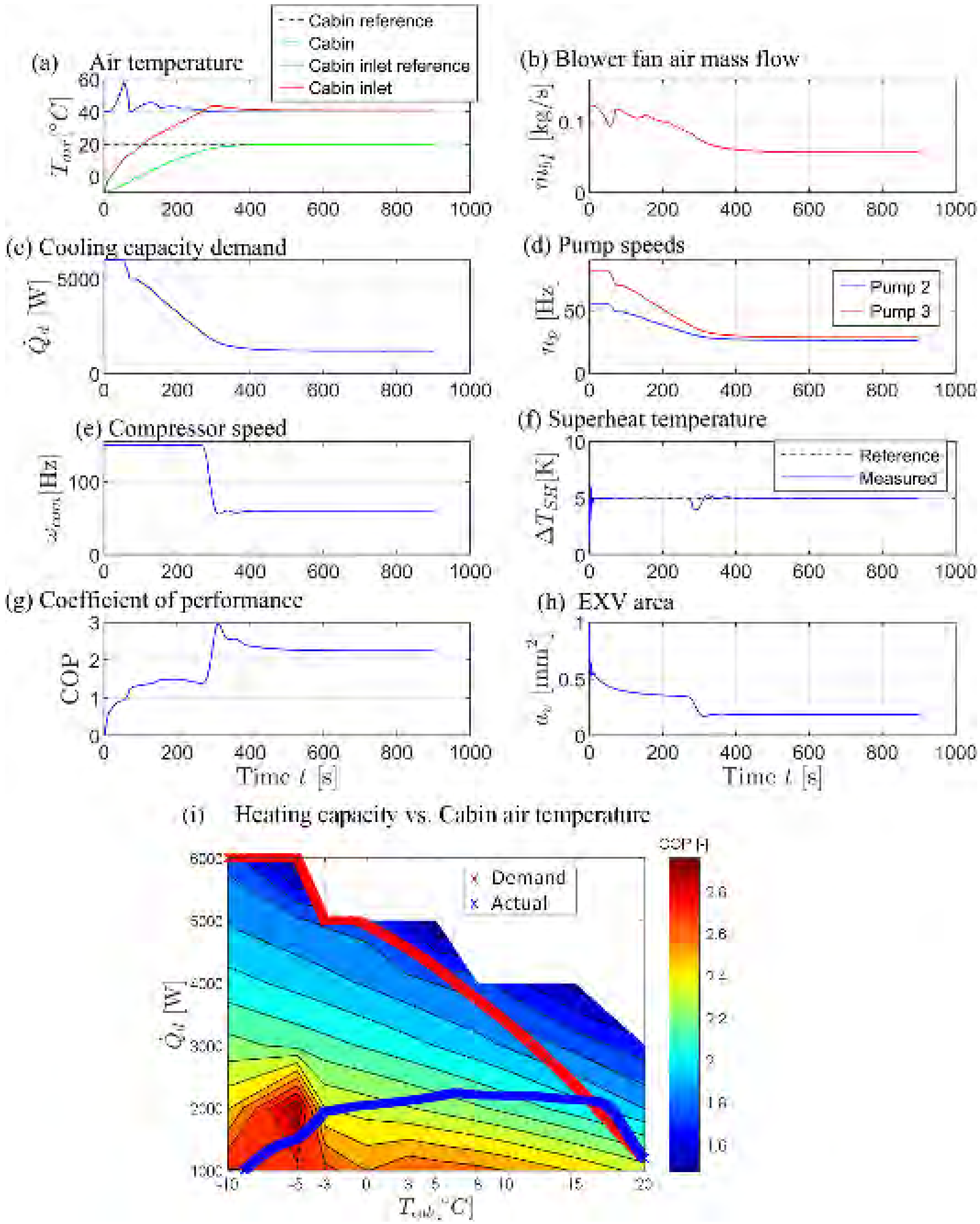

Figure 55: Simulation response of overall HP control system implemented in Dymola, given for heat-up scenario

This project has received funding from the European Union's Horizon 2020 research and innovation programme under grant agreement No. 769826. The content of this publication is the sole responsibility of the Consortium partners listed herein and does not necessarily represent the view of the European Commission or its services.

3.10. Update of Dymola model and control strategy with infrared heating panels functionality

Dymola model has been extended with infrared (IR) heating panels to investigate the potential of further thermal comfort improvement. Figure 56: Dymola model extension related to infrared heating functionality: look-up table-based cabin air mass flow and temperature distribution (a), single PMV calculation submodel (b),
IR heating panel model (c) shows the Dymola implementation of (i) cabin air mass flow and temperature distribution around the passenger (in the form of look-up tables based on CFD simulation; Figure 56: Dymola model extension related to infrared heating functionality: look-up table-based cabin air mass flow and temperature distribution (a), single PMV calculation submodel (b),
IR heating panel model (c)a) that account for the cabin air distribution (vents) setting, (ii) PMV calculation for individual body parts (driver's and codriver's head, torso and legs) that accounts for change in radiant temperature due to exposure to IR panels (Figure 56: Dymola model extension related to infrared heating functionality: look-up table-based cabin air mass flow and temperature distribution (a), single PMV calculation submodel (b),
IR heating panel model (c)b) and mean PMV calculation, and (iii) IR panel dynamics model (Figure 56: Dymola model extension related to infrared heating functionality: look-up table-based cabin air mass flow and temperature distribution (a), single PMV calculation submodel (b),
IR heating panel model (c)c). In total, six IR panels are modelled in the cabin. The control input for the IR panel is the panel target temperature multiplier $IR \in [0,1]$, where $IR = 0$ sets panel target temperature to cabin air temperature, i.e. turns the panel off, while $IR = 1$ sets the panel target to maximum value. Inner IR panel controller regulates the panel temperature by commanding the electrical power, which is modelled as heat source for IR panel body. Additional convection losses to cabin air are implemented in the IR panel, as well. However, the cabin air temperature dynamics is not affected by those losses. Note that COP calculation takes into account electrical power consumption of IR panels.

This project has received funding from the European Union's Horizon 2020 research and innovation programme under grant agreement No. 769826. The content of this publication is the sole responsibility of the Consortium partners listed herein and does not necessarily represent the view of the European Commission or its services.

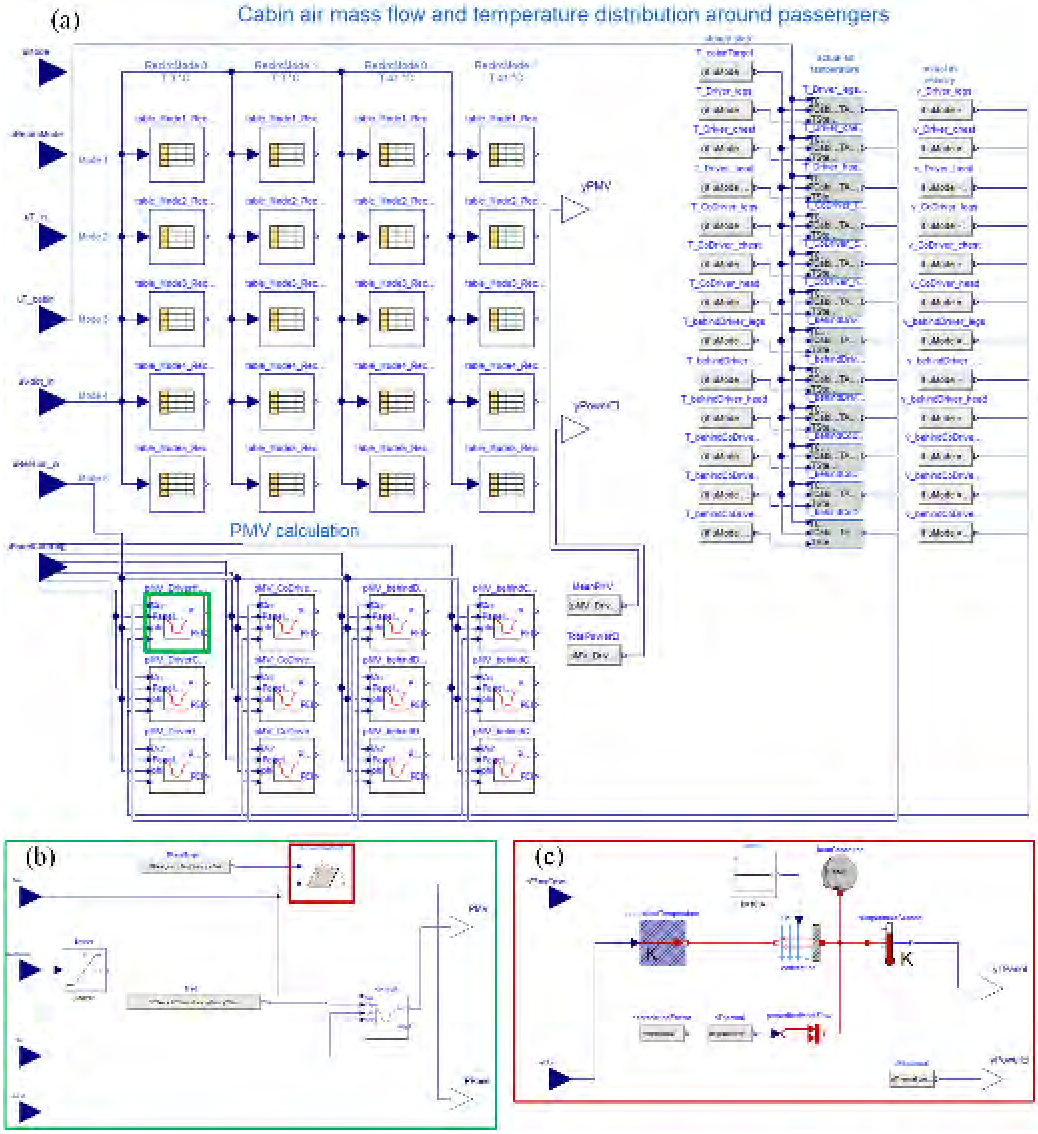

Figure 56: Dymola model extension related to infrared heating functionality: look-up table-based cabin air mass flow and temperature distribution (a), single PMV calculation submodel (b), IR heating panel model (c)

The core control strategy from Figure 53 has been extended with IR panel control designed to improve thermal comfort during the transient until the cabin air temperature reaches target value. Mathematical description of the implemented nonlinear proportional IR controller is:

$$IR = \begin{cases} sat(k_{PMV} e_{PMV}, IR_{\max}), & \text{for } e_{PMV} > \Delta PMV, \\ 0, & \text{otherwise} \end{cases} \tag{43}$$

where k_{PMV} is the controller gain (tuned separately for each panel), $IR_{\max}$ is IR control panel setpoint maximum (tuned separately for each panel), and ΔPMV is PMV error threshold for turning off the IR panel (set to 0.5 herein, which corresponds to comfort range threshold for particular PMV target value defined below; see Figure 26), and e_{PMV} is cabin mean PMV error (always greater than 0 if the passenger is cold):

$$e_{PMV} = PMV_R - PMV$$

where PMV_R is target PMV (herein set to 0).

This project has received funding from the European Union's Horizon 2020 research and innovation programme under grant agreement No. 769826. The content of this publication is the sole responsibility of the Consortium partners listed herein and does not necessarily represent the view of the European Commission or its services.

Figure 57 shows comparison of heat-up scenarios with and without IR heating. The target air temperature is set to 22°C and the ambient temperature is -10°C. Since the IR panels do not influence the cabin air temperature (it acts on the passenger through radiation), the cabin air temperature dynamics and the core control strategy including the control allocation inputs remain the same as in the HVAC-only case (Figure 57a – f, h and j; no difference between solid and dashed lines). In the case of no IR heating (solid lines), the perceived thermal comfort is in the too cold region, i.e. the mean cabin PMV (solid red line in Figure 57g) does not reach lower threshold of -0.5 (dot-dash blue line in Figure 57g). On the other hand, when the IR heating is used (dashed lines), the perceived thermal comfort is reached in about 5 minutes, i.e. PMV (dashed red line in Figure 57g) crosses lower threshold of -0.5 in that time interval and remains inside the comfort range, i.e. between lower threshold of -0.5 and upper threshold of +0.5 (dot-dash red line in Figure 57g). Note that for low cabin air temperatures and moderate blower fan air mass flow, the PMV is below -3 (it is -15 at the start). The IR panel setpoints (shown for driver head, chest and legs panel) are set to maximum value in the warm-up period (Figure 57k) and they then decrease linearly once the thermal comfort is close to target value. The IR panel target temperatures (Figure 57i) at the start are set to 20°C for legs, around 25°C for chest and 40°C for head, and increase as the cabin air temperature increases. The panels reach target temperatures in 1.5 min (legs), 2 min (chest) and around 3 min (head), and once the IR panels are turned off, their temperature slowly decreases. Within the warm-up interval the COP (dashed black line in Figure 57g) is lower for the case with IR heating, because the IR panel adds power consumption compared to the case without IR heating.

The total energy consumption for the case without IR heating is 406.64 Wh, while for the case with IR heating it is 497.26 Wh (+22%). The thermal comfort criterions for transient evaluation (see Subsection 3.4.6 for details) for the case without IR heating are $C_1 = C_{2,0.5} = 2863.8$ (where $C_{2,0.5} = \int |PMV| dt$ if $|PMV| > 0.5$), while for the case with IR heating they are $C_1 = 1949.4$ (-32%) and $C_{2,0.5} = 1912.9$ (-33%).

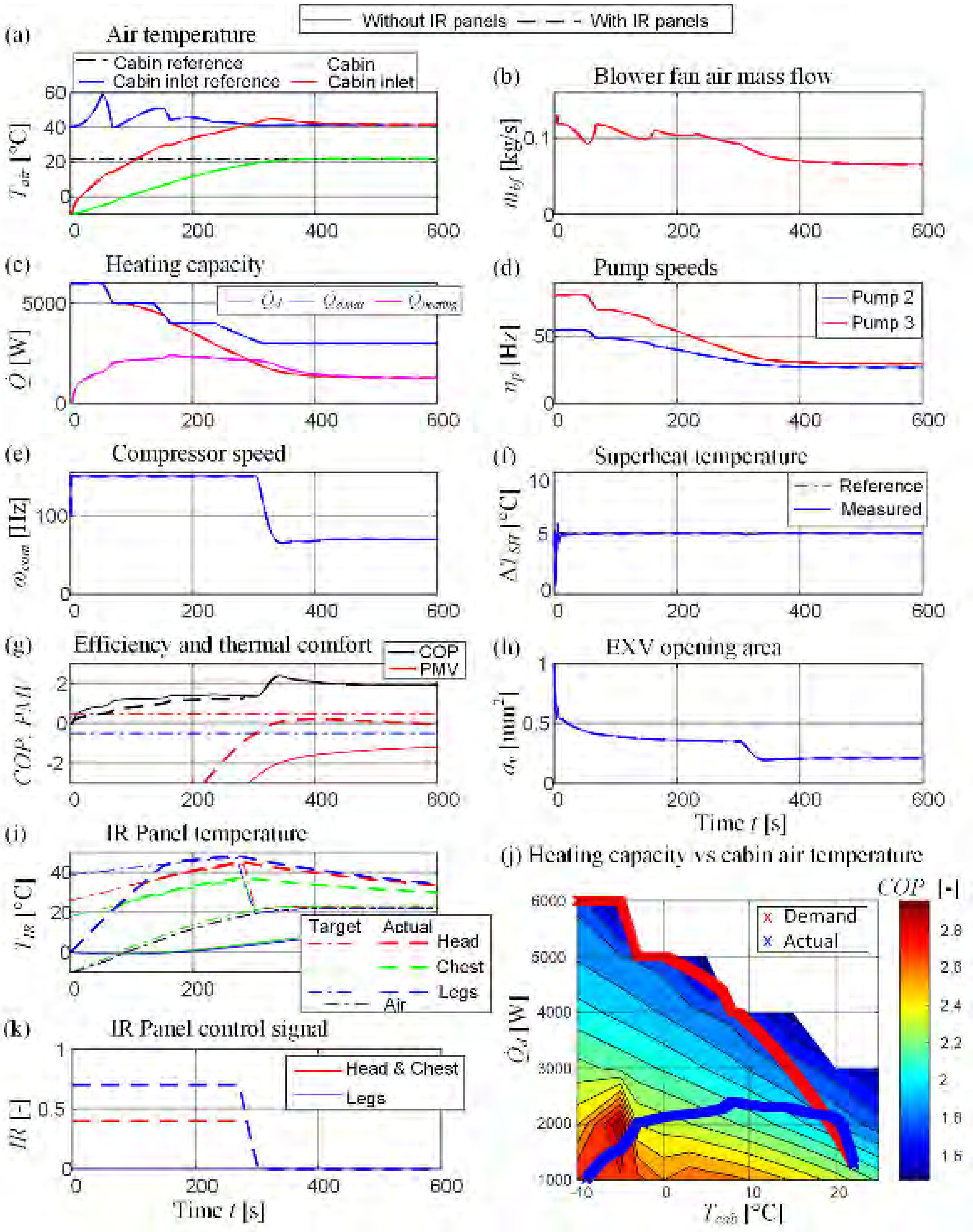

Figure 57: Simulation response comparison of overall HP control system implemented in Dymola without (solid line) and with (dashed line) infrared heating panels, given for heat-up scenario

This project has received funding from the European Union's Horizon 2020 research and innovation programme under grant agreement No. 769826. The content of this publication is the sole responsibility of the Consortium partners listed herein and does not necessarily represent the view of the European Commission or its services.

4. On-board energy management system and user interface

AIT has defined and established the hardware platform (see Figure 58) that will process the user-interface and the control strategy that communicates with all other vehicle components (HVAC, vehicle sensors, etc.) via CAN and other interfaces. In addition, drafts for the graphical user-interface (GUI) have been worked out and evaluated with the user as the key figure in mind.

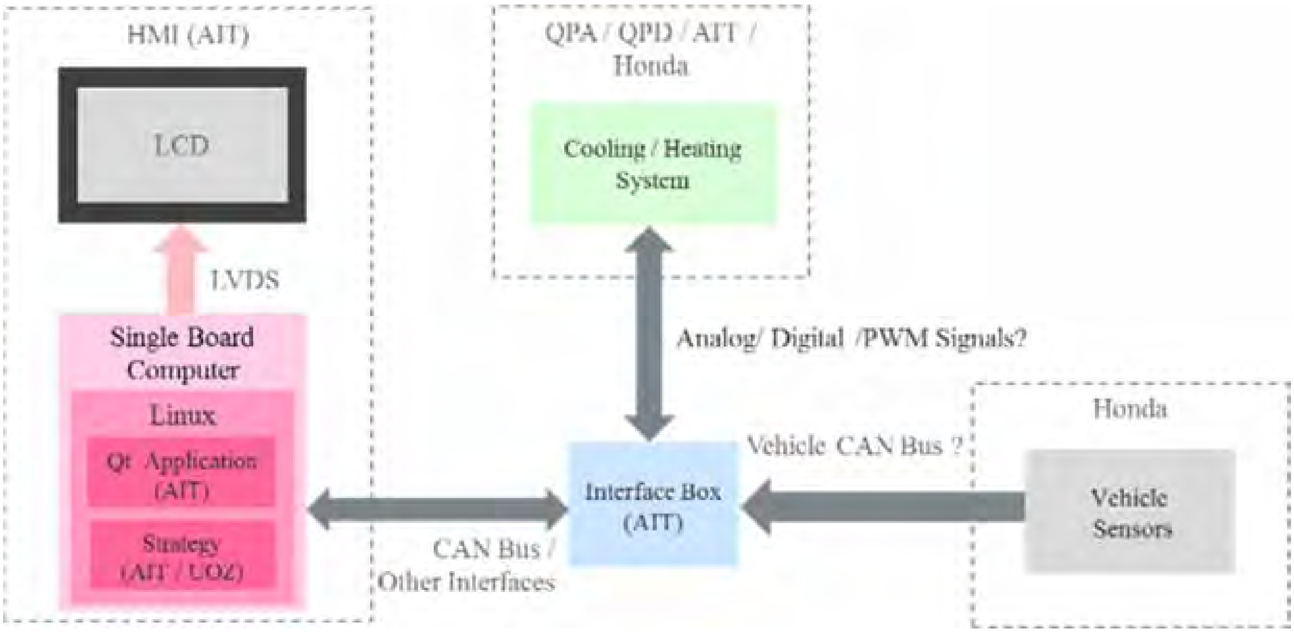

Figure 58: System overview – Human Machine Interface (HMI) concept

4.1. Hardware platform

The chosen hardware platform (see Figure 59) that inhabits the HMI and cooling/heating strategy consists of a single-board computer by Toradex, a touch LCD (7 or 10 inch) and an interface board that ensures proper connections to all other components of the vehicle. The single board computer consists of an ARM Cortex-A9 processor that is able to run an embedded Linux, and various interfaces to allow for external communication to other components. For the user interface the Qt framework was chosen. It allows to build sophisticated 2D and 3D applications for embedded devices and as a pure software-solution it ensures a rapid and from the hardware decoupled HMI implementation. The overall cooling/heating strategy runs as its own application decoupled from the user-interface within the operation system. The chosen single board computer offers a wide set of common physical interfaces/bus systems but requires an additional external interface box/board that extends the boards capability of driving higher power loads (e.g. servo-motors).

After a detailed connection plan, that includes a detailed description of all physical interfaces between all components, the single-board computer interfaces have been extended/adjusted to meet all requirements in order to control and read all involved components.

This project has received funding from the European Union's Horizon 2020 research and innovation programme under grant agreement No. 769826. The content of this publication is the sole responsibility of the Consortium partners listed herein and does not necessarily represent the view of the European Commission or its services.

Figure 59: Comparison 7" and 10" Display (left), Apalis iMX6Q Module (middle), Apalis Module and Development Board (right)

On that account, AIT has developed an interface board (see Figure 60) that acts as a central node, which ties all components in the developed system together. It consists of an ARM Cortex-R4 based microcontroller (TMS570 by Texas Instruments) that acts as a gateway and offers a lot of processing power and an assisting AVR based microcontroller (ATMega32 by Microchip) that provides additional interfaces and acts as a monitor of the main microcontroller (TMS570) in order to allow for safe operation of the whole system. The design is completely isolated thus enabling it to operate in noisy environment of the vehicle. It is packed with interfaces that covers all involved components, such as CAN (HMI Single Board Computer, Heating panels, Temperature and pressure sensors), LIN (valves), Open-Drain outputs (actuators, relays), and H-bridge drivers (actuators, DC-motors).

While its main purpose is to act as a gateway and interface extension for the single-board computer, it may also process timing critical parts of the vehicle energy management strategy, as it provides quicker response times in terms of error detection and handling of the complete system.

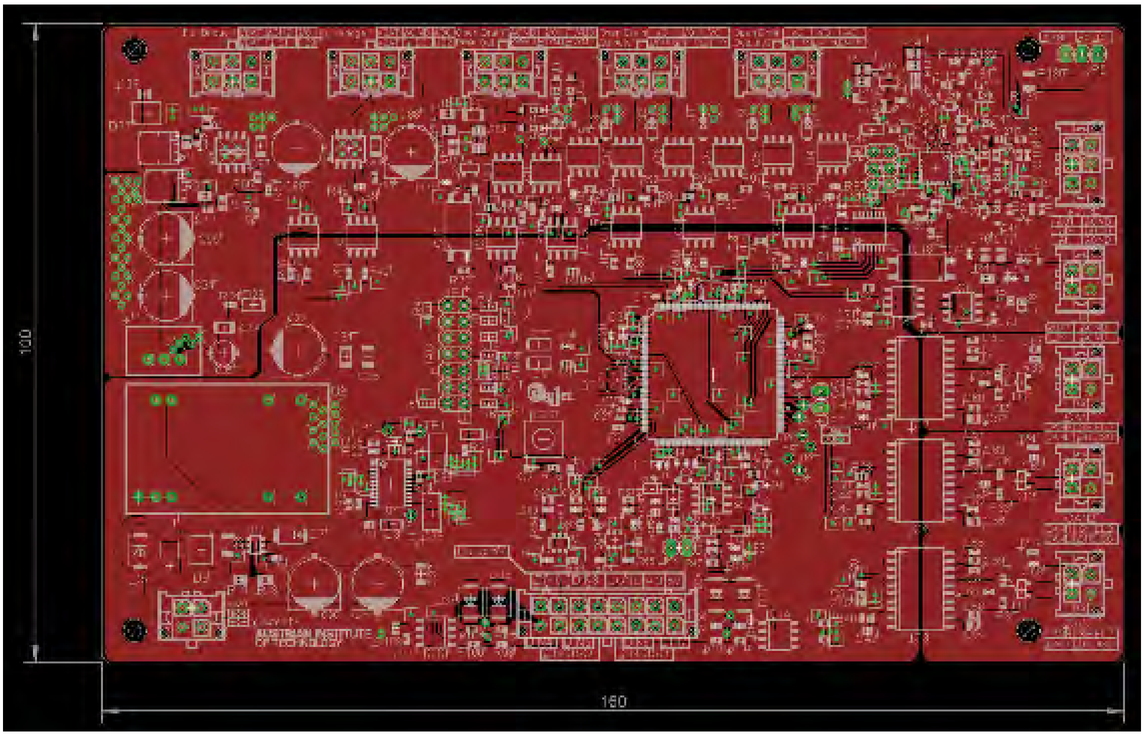

Figure 60: Interface Board developed by AIT

This project has received funding from the European Union's Horizon 2020 research and innovation programme under grant agreement No. 769826. The content of this publication is the sole responsibility of the Consortium partners listed herein and does not necessarily represent the view of the European Commission or its services.

4.2. GUI-design

As user-centric design is a key element in this project, several concepts have been carried out to further lay out the basis for the HMI. AIT has performed internal surveys that compared the conventional user-interface, to a more subjective approach. Instead of directly controlling the heating or cooling power/temperature, the user communicates his/her comfort and leaves it up to the control-strategy to take appropriate measures.
The first draft is illustrated in Figure 61 which resembles the conventional approach in terms of navigating through the interface, whereas a more interactive way is shown in Figure 62.

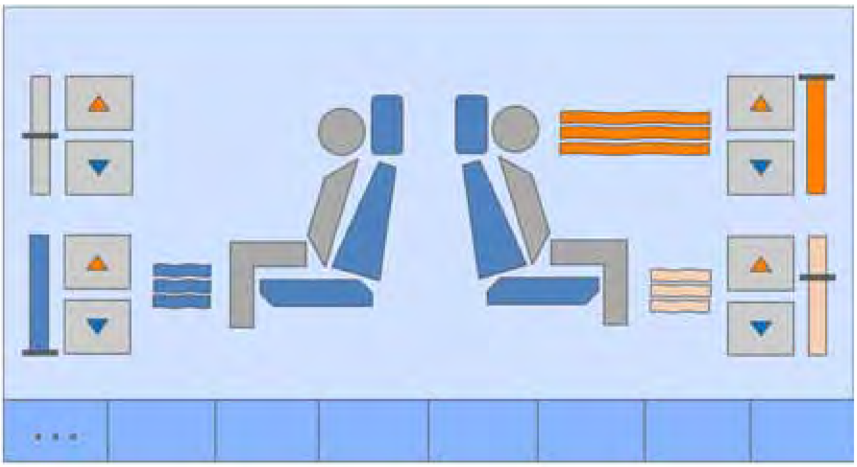

Figure 61: 1st Draft of possible GUI Design

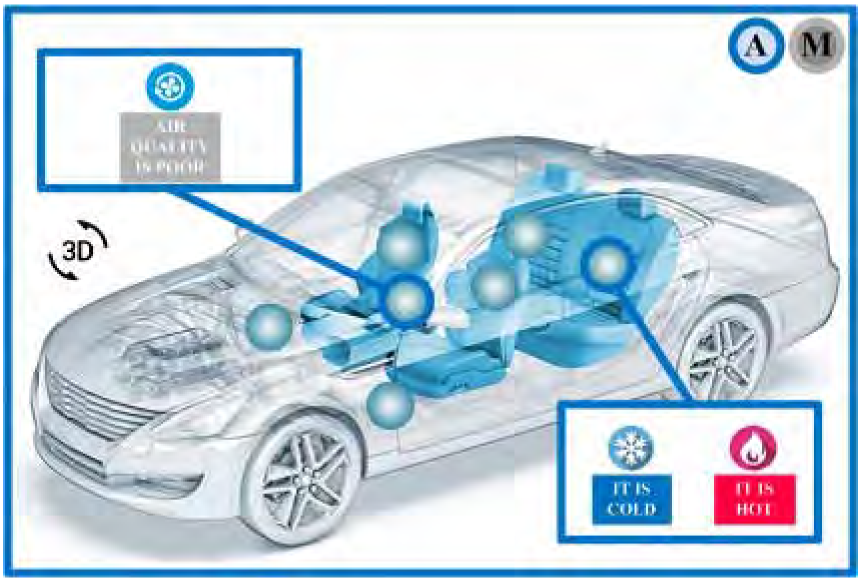

Figure 62: Advanced draft of possible GUI Design

This leads to the implementation and integration of the user-interface and control strategy within chosen hardware platform. This includes further research of the Qt framework and the software development of the

This project has received funding from the European Union's Horizon 2020 research and innovation programme under grant agreement No. 769826. The content of this publication is the sole responsibility of the Consortium partners listed herein and does not necessarily represent the view of the European Commission or its services.

user-interface (with the outcome of the GUI surveys and internal discussions) and the chosen cooling and heating strategy based on the output of Task 2.5.

The final approach that is further evaluated can be seen in Figure 63 to Figure 65. Within the automatic mode, the design is focusing on the experienced comfort level of each passenger. Each passenger can communicate their comfort level in terms of temperature by clicking on their corresponding passenger dummy. By telling the system that they “feel” cold or hot (with two designated buttons), the system capable to take appropriate measures. Additionally, the passengers in the front may select between foot and torso/head area. To let the user know that appropriate measures are currently executed, a visual feedback (rotating gears) is signalling that the system is adjusting the current state to match the users request. In either case the heating or cooling process is visualized by wavy lines hovering above the affected person. The passengers are coloured in terms of their comfort level (Red in case they feel too hot and blue if they feel too cold). In addition to the comfort control, four additional buttons have been introduced that take care of other aspects of the system such as switching between fresh and recirculating air and the windshield defogging/defrosting. In case of short-distance trips it is possible to only consider the heating panels, as heating up the cabin air (by activating the HVAC unit) would take too much time and would unnecessarily waste energy. For those who feel uncomfortable using the heating panels, it is also possible to deactivate them entirely.

Figure 63: Implemented GUI Design – AUTO control: driver upper body too hot

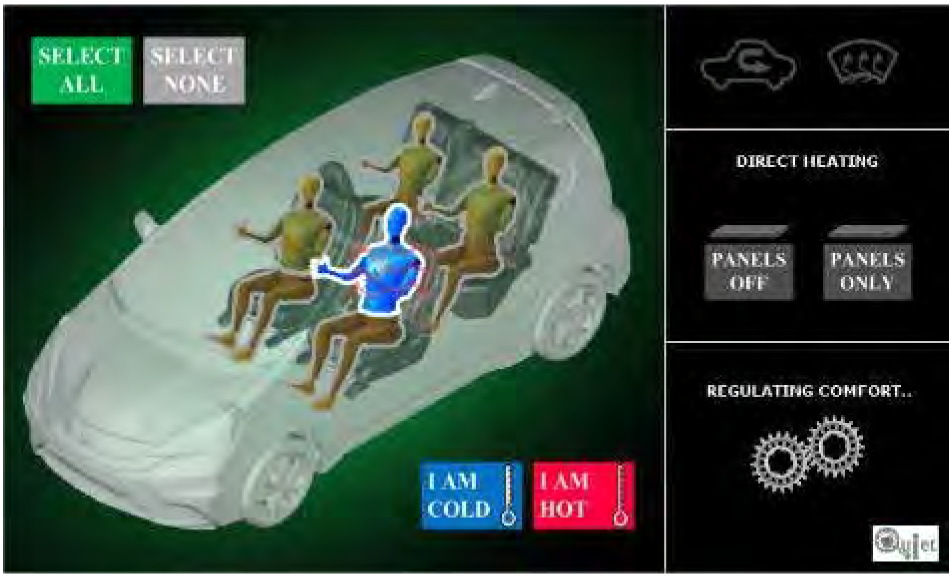

Figure 64: Implemented GUI Design – AUTO control: driver upper body too cold

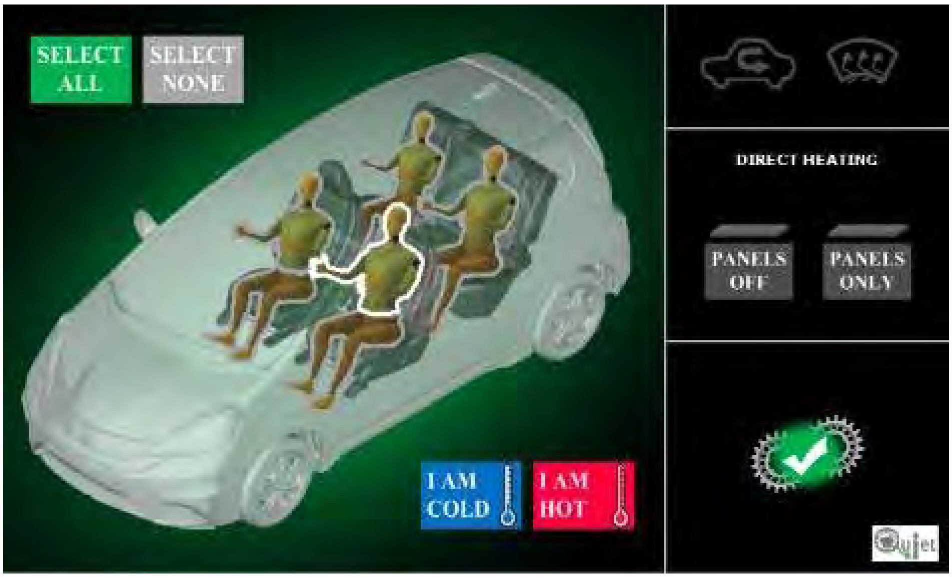

Figure 65: Implemented GUI Design – AUTO control: comfort level of all passengers reached

This project has received funding from the European Union's Horizon 2020 research and innovation programme under grant agreement No. 769826. The content of this publication is the sole responsibility of the Consortium partners listed herein and does not necessarily represent the view of the European Commission or its services.

In addition, an interface for manual control has been developed (see Figure 66). It is comparable to usual automatic air-conditioning systems that allow to set the temperature, fan speed and the air flow. Furthermore, it is possible to select every panel individually and set its desired temperature. This mode is mainly used to test and verify all included components that have been developed but may be also used by those who are more comfortable with the usual climate control.

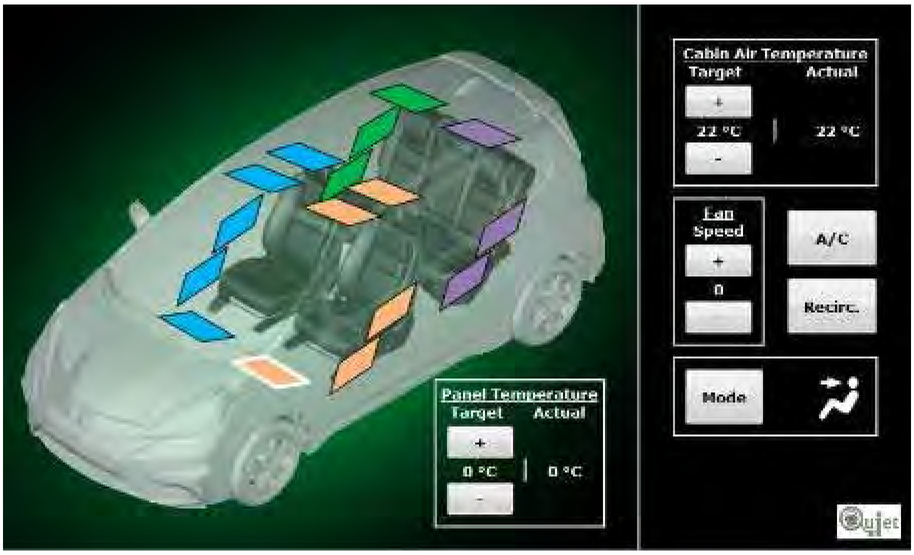

Figure 66: Implemented GUI Design – custom control

This project has received funding from the European Union's Horizon 2020 research and innovation programme under grant agreement No. 769826. The content of this publication is the sole responsibility of the Consortium partners listed herein and does not necessarily represent the view of the European Commission or its services.

5. Conclusions

With D2.2 the implementation of the comprehensive vehicle cabin model and the validation of the full multi-physical simulation model of the Honda Fit EV car is documented. The vehicle model acted as a solid basis for the creation of the optimised operation strategy of the demonstrator vehicle.

The HVAC model has already been set up successfully and the components of the AC cycle (compressor, condenser, evaporator, expansion valve, internal heat exchanger) have been parameterised successfully. Also, the components of the air- and water-side (e.g. heater core, front vehicle heat exchanger, water pumps) parameterised successfully. The model-based optimised energy management strategy of the HVAC control was developed by UOZ. Maps of HVAC static operating points were determined resulting in a linearization of reduced-order models offering operating point-dependent input-output model parameter maps. After this successful mapping a control trajectory optimisation framework to provide a cabin thermal comfort and HVAC efficiency benchmark was established. An optimised mechanism for control strategy scheduling (parameters and gain values) was developed/applied to the target electric vehicle HVAC model in the Dymola environment and verified under realistic driving cycles and operating conditions.

D2.2 deals also with the development of the electronic control unit which is required to integrate the vehicle energy management strategy. Beside the interfaces from the single-board computer to all other components the physical layer (voltage levels/range etc.) of all interfaces and connections were defined. An interface board that acts as a central node was established acting as a gateway offering a lot of processing power in order to provide quick response times in terms of error detection and handling of the complete system.

As user-centric design is a key element in this project, several concepts were studied to lay out the HMI. A more subjective approach was developed (compared to other, conventional user-interfaces) providing an intuitive touch-based display-based forwarding the users input stimuli to the electronic control unit as desired conditions for the optimised energy management strategy.

The applicability of the energy management strategy and the user interface for the intuitive control of the comfort zones in the passenger cabin regarding age and gender aspects were evaluated and assessed regarding effectiveness and efficiency. The developed operation strategy was demonstrated in a simulation environment enabling the initial assessment of the resulting behaviour of the main components of the novel HVAC system (reported in the next deliverable D2.3: Assessment report for user-centric design of the e-vehicle) confirming that high efficiency gains can be expected from the new HVAC implementation in comparison to conventional HVAC systems.

This project has received funding from the European Union's Horizon 2020 research and innovation programme under grant agreement No. 769826. The content of this publication is the sole responsibility of the Consortium partners listed herein and does not necessarily represent the view of the European Commission or its services.

6. Biblography

[1] P. Fritzson, "Principles of Object-Oriented Modeling and Simulation with Modelica 3.3", 2nd Edition, Wiley-IEEE Press, 2015

[2] TIL Suite: Software package to simulate thermal systems, TLK-Thermo GmbH, Braunschweig, March 2019.

[3] H. Elmquist, S. Mattsson and M. Otter. Object-Oriented and Hybrid Modeling in Modelica. Dynasim AG, DLR Oberpfaffenhofen, 2001.

[4] H. Giuliani, D. Simic, J.V. Gragger, C. Kral, and F. Pirker. Optimization of a four-wheel drive hybrid vehicle by means of the SmartElectricDrives and the SmartPowerTrains library. 22nd International Battery, Hybrid and Fuel Cell Electric Vehicle Symposium & Exposition, 2006.

[5] D. Simic, D. Dvorak, T. Bäuml and H. Kapeller. Modeling and evaluation of the SmartCooling (SC) library for the simulation of the thermal management in automotive applications. European Wolfram Technology Conference, 2014.

[6] D. Dvorak. The electricenergystorages library: Multi-physical battery simulation. International Symposium on E-Mobility & Energy Management, 2014.

[7] D. Dvorak, T. Bäuml, C. Niklas, D. Simic and H. Kapeller. Validation of electric energy storages library based on battery measurements. FISITA World Automotive Congress, 2014.

[8] M. A. Fayazbakhsh and M. Bahrami. Comprehensive Modeling of Vehicle Air Conditioning Loads Using Heat Balance Method. SAE International, 2013.

[9] L. Liu, F. Felgner and G. Frey. Comparison of 4 Numerical Solvers for Stiff and Hybrid Systems Simulation. 2010 IEEE 15th Conference on Emerging Technologies & Factory Automation (ETFA 2010).

[10] V. Norrefeldt and G. Grün. VEPZO – Velocity Propagating Zonal Model for the prediction of air-flow pattern and temperature distribution in enclosed spaces. 9th International Modelica Conference, September 3-5, 2012, Munich, Germany.

[11] B. P. Rasmussen and A. G. Alleyne, "Control-oriented modeling of transcritical vapor compression systems," J. Dyn. Syst. Meas. Control. Trans. ASME, vol. 126, no. 1, pp. 54–64, 2004.

[12] E. W. Grald and J. W. MacArthur, "A moving-boundary formulation for modeling time-dependent two-phase flows," Int. J. Heat Fluid Flow, vol. 13, no. 3, pp. 266–272, 1992.

[13] J. Bonilla, L. J. Yebra, S. Dormido, and E. Cellier, "Object-Oriented Modeling of Switching Moving Boundary Models for Two-phase Flow Evaporators," Mathmod, 2012.

[14] J. Jabardo, W. Mamani, and M. R. Ianella, "Modeling experimental evaluation of an automotive air conditioning system with a variable capacity compressor," Int. J. Refrig., vol. 25, no. 8, pp. 1157–1172, 2002.

[15] D. H. Richardson, H. Jiang, D. Lindsay, and R. Radermacher, "Optimization of vapor compression systems via simulation," 2002.

This project has received funding from the European Union's Horizon 2020 research and innovation programme under grant agreement No. 769826. The content of this publication is the sole responsibility of the Consortium partners listed herein and does not necessarily represent the view of the European Commission or its services.

[16] Q. Zhang, “Modeling , Energy Optimization and Control of Vapor Compression Refrigeration Systems for Automotive Applications,” 2014.

[17] I. H. Bell, J. Wronski, S. Quoilin, and V. Lemort, “Pure and Pseudo-pure Fluid Thermophysical Property Evaluation and the Open-Source Thermophysical Property Library CoolProp,” *Ind. Eng. Chem. Res.*, vol. 53, no. 6, pp. 2498–2508, Feb. 2014.

[18] X.-D. He, S. Liu, H. H. Asada, and H. Itoh, “Multivariable control of vapor compression systems,” HVAC R Res., vol. 4, no. 3, pp. 205–230, 1998.

[19] H. Li, J. E. Braun, and B. Shen, “Modeling Adjustable Throat-Area Expansion Valves,” Int. Refrig. Air Cond. Conf., no. 1, pp. 1–10, 2004.

[20] Q. Zhang and M. Canova, “Lumped-parameter modeling of an automotive air conditioning system for energy optimization and management,” ASME 2013 Dyn. Syst. Control Conf. DSCC 2013, vol. 1, 2013.

[21] M. A. Fayazbakhsh and M. Bahrami, “Comprehensive Modeling of Vehicle Air Conditioning Loads Using Heat Balance Method,” 2013.

[22] ASHRAE: American Society of Heating, Refrigerating and Air Conditioning Engineers, ANSI/ASHRAE Standard 55-2017: Thermal Environmental Conditions for Human Occupancy, vol. 2017. Atlanta, Georgia.

[23] R. E. Bellman and S. E. Dreyfus, Applied dynamic programming. 2015.

[24] R. Isermann, Digital Control Systems. Berlin, Heidelberg: Springer Berlin Heidelberg, 1981.

[25] E. Paffumi, M. Otura, M. Centurelli, R. Casellas, A. Brenner and S. Jahn, “Energy Consumption, Driving Range and Cabin Temperature Performances at Different Ambient Conditions in Support to the Design of a User-Centric Efficient Electric Vehicle: the QUIET Project”, in 14th SDEWES Conference, 2019.

[26] I. Cvok, I. Ratkovic and J. Deur, “Optimization of Control Parameters of Vehicle Air-Conditioning System for Maximum Efficiency”, SAE Paper 2020-01-1242

This project has received funding from the European Union’s Horizon 2020 research and innovation programme under grant agreement No. 769826. The content of this publication is the sole responsibility of the Consortium partners listed herein and does not necessarily represent the view of the European Commission or its services.

7. Acknowledgment

European Union's Horizon 2020 research and innovation programme

This project has received funding from the European Union's Horizon 2020 research and innovation programme under **grant agreement** No. **769826**. The content of this publication is the sole responsibility of the Consortium partners listed herein and does not necessarily represent the view of the European Commission or its services.

Project Partners:

The author(s) would like to thank the partners in the project for their valuable comments on previous drafts and for performing the review.

Participant No	Participant short name	Participant organisation name	Country
1 Coordinator	**AIT**	AIT Austrian Institute of Technology GmbH	Austria
2	**HRE**	Honda R&D Europe (Deutschland) GmbH	Germany
3	**AVL**	AVL List GmbH	Austria
4	**QPD**	qpunkt Deutschland GmbH	Germany
5	**VEN**	VENTREX Automotive GmbH	Austria
6	**UOZ**	University of Zagreb	Croatia
7	**IFAM**	Fraunhofer Institute for Manufacturing Technologies and Advanced Materials IFAM	Germany
8	**ATT**	ATT advanced thermal technologies GmbH	Austria
9	**ECON**	eCon Engineering Kft.	Hungary
10	**RUB**	Rubitherm Technologies GmbH	Germany
11	**STS**	SeatTec Sitztechnik GmbH	Germany
12	**OBR**	Obrist Engineering GmbH	Austria
13	**JRC**	Joint Research Centre - European Commission	Italy

Appendix A1 - 12th order model

Condenser model is defined with the system matrix $\mathbf{A}_c$

$$\mathbf{A}_c = \begin{bmatrix} A_c\bar{\rho}_1(\bar{h}_1 - h_1) & A_cL_{c1}\left(\frac{d(\bar{\rho}_1\bar{h}_1)}{dp_c} - \frac{d\bar{\rho}_1}{dp_c}h_1\right) & 0 & 0 & 0 & 0 & 0 \\ A_c\bar{\rho}_3(h_2 - \bar{h}_3) & A_cL_{c3}\left(\frac{d(\bar{\rho}_3\bar{h}_3)}{dp_c} - \frac{d\bar{\rho}_3}{dp_c}h_2\right) & A_c\bar{\rho}_3(h_2 - \bar{h}_3) & \frac{1}{2}A_cL_{c3}\left(\bar{\rho}_3 + \frac{d\rho_3}{dh}|_{p_c}(\bar{h}_3 - h_2)\right) & 0 & 0 & 0 \\ A_c(\bar{\rho}_1 - \bar{\rho}_3) & A_cL_{c2}\left(\frac{d\rho_{lg}}{dp_c} + \frac{d\bar{\rho}_1}{dp_c} + \frac{d\bar{\rho}_3}{dp_c}\right) & A_c(\rho_{lg} - \bar{\rho}_3) & \frac{1}{2}A_cL_{c3}\frac{d\rho_3}{dh}|_{p_c} & 0 & 0 & 0 \\ A_c(\bar{\rho}_1h_1 - \bar{\rho}_3h_2) & A_c\left(L_{c2}\left(\frac{d(\rho h)_{lg}}{dp_c} - 1\right) + L_{c1}\frac{d\bar{\rho}_1}{dp_c}h_1 + L_{c3}\frac{d\bar{\rho}_3}{dp_c}h_2\right) & A_c((\rho h)_{lg} - \bar{\rho}_3h_2) & \frac{1}{2}A_cL_{c3}\frac{d\rho_3}{dh}|_{p_c}h_2 & 0 & 0 & 0 \\ -(T_{cw2} - T_{cw1}) & 0 & 0 & 0 & L_{c1} & 0 & 0 \\ (T_{cw2} - T_{cw3}) & 0 & -(T_{cw3} - T_{cw2}) & 0 & 0 & L_{c2} & 0 \\ (T_{cw3} - T_{cw3}) & 0 & (T_{cw3} - T_{cw3}) & 0 & 0 & 0 & L_{c3} \end{bmatrix} \quad (A1.1)$$

and with conservation balance vector $\mathbf{f}_c$ that contains mass balance and heat exchange elements for the overall length of the condenser L_c

$$\mathbf{f}_c = \begin{bmatrix} \dot{m}_{ci}(h_{ci} - h_1) - \dot{Q}_{cr1} \\ -\dot{Q}_{cr3} - \dot{m}_{co}(h_{co} - h_2) \\ \dot{m}_{ci} - \dot{m}_{co} \\ -\dot{Q}_{cr2} + \dot{m}_{ci}h_1 - \dot{m}_{co}h_2 \\ \frac{\dot{Q}_{cr1} - \dot{Q}_{ca1}}{(c_pm/L_c)_w} \\ \frac{\dot{Q}_{cr2} - \dot{Q}_{ca2}}{(c_pm/L_c)_w} \\ \frac{\dot{Q}_{cr3} - \dot{Q}_{ca3}}{(c_pm/L_c)_w} \end{bmatrix} \quad (A1.2)$$

Evaporator model is defined with the system matrix $\mathbf{A}_e$

$$\mathbf{A}_e = \begin{bmatrix} A_eL_{e3}\left(\frac{d(\bar{\rho}_{e3}\bar{h}_{e3})}{dp_e} - \frac{d\bar{\rho}_{e3}}{dp_e}h_{e2}\right) & A_e\bar{\rho}_{e3}(h_{e2} - \bar{h}_{e3}) & \frac{1}{2}A_eL_{e3}\left(\bar{\rho}_{e3} + \frac{d\rho_{e3}}{dh}|_{p_e}(\bar{h}_{e3} - h_{e2})\right) & 0 & 0 \\ A_e\left(L_{e2}\frac{d\rho_{elg}}{dp_e} + L_{e3}\frac{d\bar{\rho}_{e3}}{dp_e}\right) & A_e(\rho_{elg} - \bar{\rho}_3) & \frac{1}{2}A_eL_{e3}\frac{d\rho_{e3}}{dh}|_{p_e} & 0 & 0 \\ A_e\left(L_{e2}\left(\frac{d(\rho h)_{elg}}{dp_e} - 1\right) + L_{e3}\frac{d\bar{\rho}_3}{dp_3}h_{e3}\right) & A_e((\rho h)_{elg} - \bar{\rho}_3h_{e2}) & \frac{1}{2}A_eL_{e3}\frac{d\rho_{e3}}{dh}|_{p_e}h_2 & 0 & 0 \\ 0 & -(T_{ew3} - T_{ew2}) & 0 & L_{e2} & 0 \\ 0 & (T_{ew2} - T_{ew3}) & 0 & 0 & L_{e3} \end{bmatrix} \quad (A1.3)$$

and with the conservation balance vector $\mathbf{f}_e$ that contains mass balance and heat exchange elements for the overall length of the evaporator L_e

$$\mathbf{f}_e = \begin{bmatrix} \dot{Q}_{er3} - \dot{m}_{eo}(h_{eo} - h_{e2}) \\ \dot{m}_{ei} - \dot{m}_{eo} \\ \dot{Q}_{er2} + \dot{m}_{ei}h_{ei} - \dot{m}_{eo}h_{e2} \\ \frac{\dot{Q}_{ea2} - \dot{Q}_{er2}}{(c_pm/L_e)_{ew}} \\ \frac{\dot{Q}_{ea3} - \dot{Q}_{er3}}{(c_pm/L_e)_{ew}} \end{bmatrix} \quad (A1.7)$$

This project has received funding from the European Union's Horizon 2020 research and innovation programme under grant agreement No. 769826. The content of this publication is the sole responsibility of the Consortium partners listed herein and does not necessarily represent the view of the European Commission or its services.

Appendix A2 - 6th order model

The outlet specific enthalpies h_{eo} and h_{co} are assumed to be static. The specific enthalpy cannot be calculated directly, but is derived from two other properties, pressure and temperature. Expressions for outlet temperatures are from the heat balance equation for the third node.
Evaporator outlet temperature T_{eo} is calculated:

$$T_{eo} = \frac{2\alpha_{ei3}A_{ei}(L_e - L_{e2})T_{ew} + T_{er2}\left(2c_{p,r}\dot{m}_{com} - \alpha_{ei3}A_{ei}(L_e - L_{e2})\right)}{2c_{p,r}\dot{m}_{com} + \alpha_{ei3}A_{ei}(L_e - L_{e2})} \tag{A2.1}$$

Condenser outlet temperature T_{co} is calculated:

$$T_{co} = \frac{2\alpha_{crw3}D_{ci}\pi(L_c - L_{c2} - L_{c1})T_{cw} + T_{cr2}\left(2c_{p,r}\dot{m}_v - \alpha_{crw3}D_{ci}\pi(L_c - L_{c2} - L_{c1})\right)}{2c_{p,r}\dot{m}_v + \alpha_{crw3}D_{ci}\pi(L_c - L_{c2} - L_{c1})} \tag{A2.2}$$

Reduced condenser state vector now has the following form:

$$\boldsymbol{x}_{c,R6} = [p_c \quad L_{c2} \quad T_{cw}]^T \tag{A2.3}$$

Reduced R8 condenser matrix $\mathbf{A}_{c,R6}$ now has the following form:

$$\mathbf{A}_{c,R6} = \begin{bmatrix} A_c\left(\frac{d\rho_{lg}}{dp_c} + \frac{d\bar{\rho}_1}{dp_c} + \frac{d\bar{\rho}_3}{dp_c}\right) & A_c(\rho_{lg} - \bar{\rho}_3) & 0 \\ A_c\left(L_{c2}\left(\frac{d(\rho h)_{lg}}{dp_c} - 1\right) + L_{c1}\frac{d\bar{\rho}_1}{dp_c}h_1 + L_{c3}\frac{d\bar{\rho}_3}{dp_c}h_2\right) & A_c\left((\rho h)_{lg} - \bar{\rho}_3 h_2\right) & 0 \\ 0 & 0 & L_c \end{bmatrix} \tag{A2.4}$$

and the condenser vector $\mathbf{f}_{c,R8}$

$$\mathbf{f}_{c,R6} = \begin{bmatrix} \dot{m}_{ci} - \dot{m}_{co} \\ -\dot{Q}_{cr2} + \dot{m}_{ci}h_1 - \dot{m}_{co}h_2 \\ \frac{\dot{Q}_{cr1-3} - \dot{Q}_{ca1-3}}{(c_p m/L_c)_{cw}} \end{bmatrix} \tag{A2.5}$$

Reduced evaporator state vector now has the following form:

$$\mathbf{x}_{e,R6} = [p_c \quad L_{c2} \quad T_{cw}]^T \tag{A2.6}$$

Reduced R6 evaporator matrix $\mathbf{A}_{e,R6}$ now has the following form:

$$\mathbf{A}_{e,R6} = \begin{bmatrix} A_e L_{e3}\left(\frac{d(\bar{\rho}_{e3}\bar{h}_{e3})}{dp_e} - \frac{d\bar{\rho}_{e3}}{dp_e}h_{e2}\right) & A_e\bar{\rho}_{e3}(h_{e2} - \bar{h}_{e3}) & 0 \\ A_e\left(L_{e2}\frac{d\rho_{elg}}{dp_e} + L_{e3}\frac{d\bar{\rho}_{e3}}{dp_e}\right) & A_e\left(\rho_{elg} - \bar{\rho}_3\right) & 0 \\ A_e\left(L_{e2}\left(\frac{d(\rho h)_{elg}}{dp_e} - 1\right) + L_{e3}\frac{d\bar{\rho}_3}{dp_3}h_{e3}\right) & A_e\left((\rho h)_{elg} - \bar{\rho}_3 h_{e2}\right) & 0 \\ 0 & 0 & L_e \end{bmatrix} \tag{A2.7}$$

and the condenser vector $\mathbf{f}_{e,R6}$

$$\mathbf{f}_{e,R6} = \begin{bmatrix} \dot{m}_{ei} - \dot{m}_{eo} \\ \dot{Q}_{er2} + \dot{m}_{ei}h_{ei} - \dot{m}_{eo}h_{e1} \\ \frac{\dot{Q}_{ea} - \dot{Q}_{er2-3}}{(c_p m/L_e)_{ew}} \end{bmatrix} \tag{A2.8}$$

This project has received funding from the European Union's Horizon 2020 research and innovation programme under grant agreement No. 769826. The content of this publication is the sole responsibility of the Consortium partners listed herein and does not necessarily represent the view of the European Commission or its services.